

ASTRONOMICAL INSTITUTE
SLOVAK ACADEMY OF SCIENCES

CONTRIBUTIONS
OF THE ASTRONOMICAL OBSERVATORY
SKALNATÉ PLESO

• VOLUME LIV •

Number 3



August 2024

Editorial Board

Editor-in-Chief

Augustín Skopal, *Tatranská Lomnica, The Slovak Republic*

Managing Editor

Richard Komžík, *Tatranská Lomnica, The Slovak Republic*

Editors

Július Koza, *Tatranská Lomnica, The Slovak Republic*

Aleš Kučera, *Tatranská Lomnica, The Slovak Republic*

Luboš Neslušan, *Tatranská Lomnica, The Slovak Republic*

Vladimír Porubčan, *Bratislava, The Slovak Republic*

Theodor Pribulla, *Tatranská Lomnica, The Slovak Republic*

Advisory Board

Bernhard Fleck, *Greenbelt, USA*

Arnold Hanslmeier, *Graz, Austria*

Marian Karlický, *Ondřejov, The Czech Republic*

Jan Vondrák, *Prague, The Czech Republic*

©

Astronomical Institute of the Slovak Academy of Sciences
2024

ISSN: 1336-0337 (on-line version)

CODEN: CAOPF8

Editorial Office: Astronomical Institute of the Slovak Academy of Sciences
SK - 059 60 Tatranská Lomnica, The Slovak Republic

CONTENTS

STARS

M.A. Hanna, A. Nakhlawy, M. Hayman, M.Y. Amin, H.R. Dwidar, M.A. El-Khamisy, A. Essam: Light curve analysis for the two eclipsing binary stars EM Cet and EL Cen	5
A.A. Haroon, W.H. Elsanhoury, A.S. Saad, E.A. Elkholy: Deep investigation of a pair of open clusters NGC 7031 and NGC 7086 utilizing Gaia DR3	22

GENERAL RELATIVITY

L. Neslušan: Outward oriented gravitational attraction in the innermost part of the compact objects - a new feature of relativistic gravity	49
--	----

The Contributions of the Astronomical Observatory Skalnaté Pleso
are available in the full version
in the frame of ADS Abstract Service
and can be downloaded in a usual way from the URL address:

<https://ui.adsabs.harvard.edu/>

as well as from the website of
the Astronomical Institute of the Slovak Academy of Sciences
on the URL address:

<https://www.astro.sk/caosp/caosp.php>

The journal is covered/indexed by:


Web of Science (WoS)

WoS Core Collection: Science Citation Index Expanded

SCOPUS

Index Copernicus International

Light curve analysis for the two eclipsing binary stars EM Cet and EL Cen

M.A. Hanna¹ , A. Nakhlawy¹, M. Hayman², M.Y. Amin²,
H.R. Dwidar², M.A. El-Khamisy¹ and A. Essam¹

¹ *National Research Institute of Astronomy and Geophysics, Department of Astronomy, Helwan, Cairo, Egypt (E-mail: magdyh_nriag06@yahoo.com)*

² *Cairo University, Faculty of Science, Department of Astronomy and Meteorology, Egypt*

Received: April 23, 2023; Accepted: May 2, 2024

Abstract. We present the first light curve analysis of the two eccentric eclipsing binary stars EM Cet and EL Cen by using the PHOEBE Code. The selected stars were taken from the Peremennye Zvezdy Prilozhenie supplement (PZP). Both were observed by the All Sky Automated Survey (ASAS) in the V band. Another light curve for EM Cet was observed via the Transiting Exoplanet Satellite (TESS). From the TESS observations we determined 4 new minima times. Orbital and physical parameters were determined. The analysis showed that the two targets confirming the concept of orbital circularization theories that stars with lower eccentricities are with later spectral types. A comparison between the results obtained from the two light curves of ASAS and TESS for EM Cet has been investigated.

Key words: detached binaries – EM Cet – EL Cen

1. Introduction

The study of apsidal motion of detached Eccentric Eclipsing Binary stars (EEBs) is important because it provides information about the internal structure of the stars. Apsidal motion refers to the rotation of the line connecting the two stars in an elliptical orbit. By measuring the rate of apsidal motion, astronomers can determine the structure constants k_2 specifying the density distribution in each of the components. Apsidal motion in binary star systems can be caused by several factors: (i) mutual tidal deformation of the components due to the gravitational interaction between them, affecting their orbits; (ii) deformation of the components due to the axial rotation of the stars which can also cause shape variations, (iii) the relativistic effects that introduces subtle corrections to the orbital dynamics, impacting the apsidal motion, and (iv) the compactness of triples that was investigated by [Rappaport et al. \(2024\)](#) can lead to interesting and important dynamical interactions, including so-called dynamical delays, driven apsidal motion in the inner binary (see also, e.g., [Rappaport et al., 2023](#); [Borkovits et al., 2015](#); [Borkovits & Mitnyan, 2023](#)). Hence, to investigate and

probe the internal structure of the stars many astronomers have focused their attention on studying detached eclipsing binary systems whose light curves exhibit a secondary minimum phase shift out of the value 0.5.

Researchers have difficulty observing detached systems with ordinary telescopes, because their orbital periods are long, making it difficult to cover the entire light curve compared to binaries with short periods. Fortunately, modern robotic space telescopes and significant advances in instrumentation over the past three decades have enabled several large-scale optical surveys to report tens of thousands of new eclipsing binaries in our Galaxy and other nearby galaxies (Kim *et al.*, 2018). Consequently, several catalogues have been formed by several authors, especially for detached binary stars showing apside line rotation, such as Petrova & Orlov, 1999; Hegedüs *et al.*, 2005; Bulut & Demircan, 2007; Prša *et al.*, 2011; Slawson *et al.*, 2011; Kirk *et al.*, 2016; and Kim *et al.*, 2018. For a preferred summary view of these catalogs, see Kjurkchieva *et al.* (2017). We have used in the present analysis light curves from the ASA-Survey (Pojmanski, 1997) and the TESS (Ricker *et al.*, 2015) mission. Pojmanski (2002) explained the description of the All-Sky Automated Survey that started at the beginning of 1996. It is a long-term project that provides long-baseline light curves for sources brighter than $V=15$ mag across the whole sky. The Transiting Exoplanet Survey Satellite (TESS), launched by NASA in 2018, is a space telescope designed to discover thousands of exoplanets orbiting the brightest dwarf stars. It has also produced high-quality light curves with a baseline of at least 27 days, eventually for most of the sky. The combination of ASAS and TESS light curves probes both long- and short-term variability in great detail, especially towards the TESS Continuous Viewing Zones (CVZ) at the ecliptic poles.

2. Source of data

We selected light curves for two detached systems, EM Cet and EL Cen, from the Peremennye Zvezdy Prilozhenie Supplement (Khruslov, 2012); and Kazarovets & Pastukhova (2017) that are characterized by an apparent secondary minimum phase shift apart of 0.5. However, Nedoroščik *et al.*, 2014; presented an effective way to quickly classify eclipsing binaries from the ASAS data via performing the Fourier decomposition of the phase light curves. They used the relations between the Fourier coefficients to infer principal properties of eclipsing binaries and, hence, the systems with eccentric orbits could be distinguished. The light curves of both systems were observed by the ASAS. In the analysis we also included another light curve for EM Cet from the TESS observations which is available with the 120-second cadence.

Table 1 displays the magnitudes in different bands, the color index and the effective temperatures of both stars. The next two sub-sections 2.1 and 2.2 give short accounts about both targets.

Table 1. Magnitudes, colors and effective temperatures of the two targets.

	EM Cet	EL Cen
J	08.685 ¹	11.351 ¹
H	08.426 ¹	11.237 ¹
K	08.400 ¹	11.171 ¹
B	10.23 ³	12.67 ²
V	09.64 ³	12.27 ²
J-H	0.259	0.114
B-V	0.590	0.310
$T_{eff.}$	6381 ⁵	6841 ⁴

¹Cutri et al., 2003, -yCat. 2246²Høg et al., 2000³Watson et al., 2006= VSX. 2005⁴Bai et al., 2019⁵Zhang et al., 2023

2.1. EM Cet

The star EM Cet ($\alpha_{2000} = 03^{\text{h}} 22^{\text{m}} 37^{\text{s}}.91$, $\delta_{2000} = -0^{\circ} 31' 42''.5$) was discovered by the Hipparcos mission and listed under serial number HIP 15728 (ESA, 1997) with a primary minimum 2448510^d.883 and an orbital period, $P = 13^{\text{d}}.2714$ day. Subsequently, it was named in the GCVS as EM Cet by Kazarovets et al. (1999) who classified the star as an eclipsing Algol (EA:). Kazarovets & Pastukhova (2017) selected the star from the ASAS photometric catalogue (ASAS 032238-0031.7) and reported $F8$ as a spectral type and gave a new period $P = 10^{\text{d}}.5240$ instead of the false period, $P = 13^{\text{d}}.2714$, given in the Hipparcos and Tycho Catalogues (ESA, 1997). They gave the line elements:

$$HJDMinI = 24\ 54783^{\text{d}}.709 + 10^{\text{d}}.5240E \quad (1)$$

Another light curve has been observed via TESS mission with serial number TIC 279097963, magnitude (T_{mag}) = 9.1854, and effective temperature $T_{eff} = 6381.06$ K with the ephemeris:

$$HJDMinI = 24\ 58414^{\text{d}}.498384 + 10^{\text{d}}.5242227E. \quad (2)$$

On the other side, two ephemerids were given for both primary and secondary minimum in the online O-C Gateway catalogue as:

$$HJDMinI = 24\ 48510^{\text{d}}.883 + 10^{\text{d}}.5141E, \quad (3)$$

$$HJDMinII = 24\ 48517^{\text{d}}.296 + 10^{\text{d}}.5141E. \quad (4)$$

The times of minimum light listed in Table 2 were taken from the online O-C gateway website (Paschke & Brat, 2006). Besides, we deduced 4 new minima

times from the TESS observations by using the AVE program that depends on [Barbera \(1996\)](#) method. The O-C residuals were calculated using equation (2), and plotted in Fig. 1.

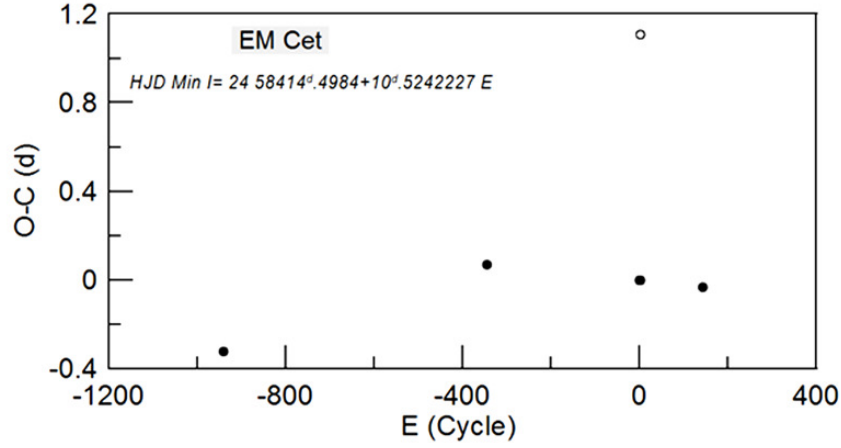


Figure 1. The O-C Diagram of EM Cet, dots stand for primary minima, an open circle for the secondary one.

Table 2. Time of minima for EM Cet.

HJD (+2400000)	Error	O-C	Type	Method	Ref.
48510.8830:		-0.32182	P	pe V	[1]
54783.7090		0.06745	P	pe V	[1]
58414.498818	0.000029	0.00043	P	CCD I	pw
58425.022845	0.000041	0.00024	P	CCD I	pw
58431.391731	0.000077	1.10701	S	CCD I	pw
58435.546786	0.000030	-0.00004	P	CCD I	pw
59929.954		-0.03245	P	Ic	[1]

Ref: [1] [Paschke & Brat \(2006\)](#). pw: present work (from TESS observations).

2.2. EL Cen

The star EL Cen ($\alpha_{2000} = 13^{\text{h}} 30^{\text{m}} 25^{\text{s}}.2$, $\delta_{2000} = -56^{\circ} 54' 52''.2$; TIC 68295752; ASAS 133025-5654.9) was discovered as an eclipsing variable by [Hoffleit \(1930\)](#)

taking Harvard serial number HV 4757. It was discovered while surveying the southern Milky Way by examining the Modified Forster-plates (MF), which was developed by the German astronomer Paul Forster to be more sensitive to shorter wavelengths of light than the traditional photographic plates, and taken by a refracting 10-inch Metcalf telescope located at the Boyden Observatory in South Africa.

An earlier version of GCVS classified the system as an eclipsing variable star without specifying its light elements. [Khruslov \(2012\)](#) confirmed its eclipsing nature according to the Automated Survey (ASAS-3) data and recorded secondary minimum phase shift ϕ_2 at 0.312 and minima differ in duration: $DI = 0.012 P$ and $DII = 0.022 P$. He also gave the light elements:

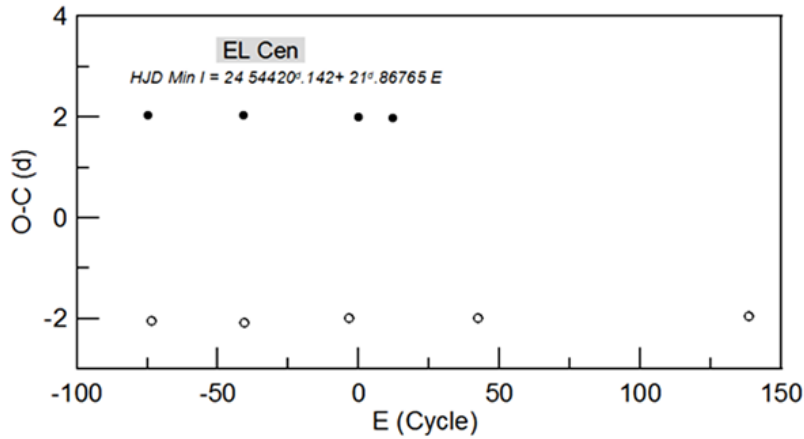


Figure 2. The O-C Diagram of EL Cen, filled circles stand for primary minima, open circles for secondary ones.

$$HJD(Min.I) = 24\ 53525^d.600 + 21^d.8677E. \quad (5)$$

The eclipse times of minima are listed in Table 3 from the O-C gateway catalog with the primary and secondary light elements:

$$HJD(Min.I) = 24\ 53525^d.600 + 21^d.8677E, \quad (6)$$

$$HJD(Min.II) = 24\ 53532^d.423 + 21^d.8677E. \quad (7)$$

EL Cen is also included in the Galactic eccentric eclipsing binary stars catalogue which is based on the eclipse timing diagram ([Kim et al., 2018](#)), with

Table 3. Times of minima for EL Cen.

HJD (+2400000)	O-C	Type	Method	Ref.
52782.1040	2.03575	P	pe V	[1]
52810.8320	-2.037725	S	pe V	[1]
53525.6000	2.03165	P	pe V	[2]
53532.4230	-2.079175	S	pe V	[2]
54341.6200	-1.985225	S	pe V	[1]
54422.1420	0	P	pe V	[1]
54684.5480	1.9942	P	pe V	[3]
55347.5338	-1.983325	S	pe V	[1]
57446.8630	-1.948525	S	-	[3]

Ref: [1] [Kim et al. \(2018\)](#). [2] [Khruslov \(2012\)](#). [3] [Paschke & Brat \(2006\)](#).

maximum $mag_V = 12.3$, and secondary minimum phase shift at 0.317. They gave the light elements:

$$HJD(Min.I) = 24\ 54420^d.142 + 21^d.86765 E. \quad (8)$$

The O-C residual diagram is shown in Fig. 2, where the residuals were calculated using the ephemeris of equation (8).

3. Light curve analysis

To model the light curves, we used the package PHOEBE v0.31 ([Prša & Zwitter, 2005](#)). The light curves' morphology shows constant out-of-eclipse parts and a secondary minimum phase shift value out of 0.5 for the two targets, then we used the mode Detached. To proceed with the use of PHOEBE one has to prepare some input initial parameters. For EM Cet and EL Cen the light curves' morphology shows difference between the depths of both eclipses, so the temperatures and radii of the primary and secondary components have to be different. Hence, the task is to set the temperature of the primary component as a constant value and to fit the temperature of the secondary one ([Zasche, 2016](#)).

The ASAS light curves of the two systems were observed in the V-band, while the light curve of TESS was observed in the 8100 Å I central band (=7865 Å); we have chosen the Cousins I filter in PHOEBE. We used $T_{1eff} = 6381$ K ([Zhang et al., 2023](#)) for EM Cet and 6841 K for EL Cen from [Bai et al. \(2019\)](#). Given some other parameters, such as gravity-darkening and bolometric albedo, one can begin to model the two systems. The gravity darkening can be found following [Lucy \(1967\)](#) and [Ruciński \(1973\)](#). For both systems, assuming convective envelope components ($T_1 < 7200$ K), the gravity-darkening $g_1 = g_2 = 0.32$ and the primary star albedo $A_1 = A_2 = 0.5$ ([Zasche, 2016](#)).

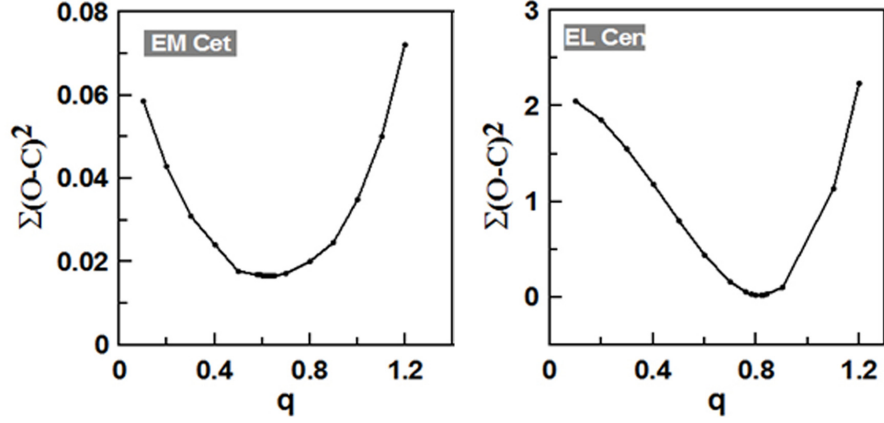


Figure 3. The $q_{ph} - \sum(O - C)^2$ relation

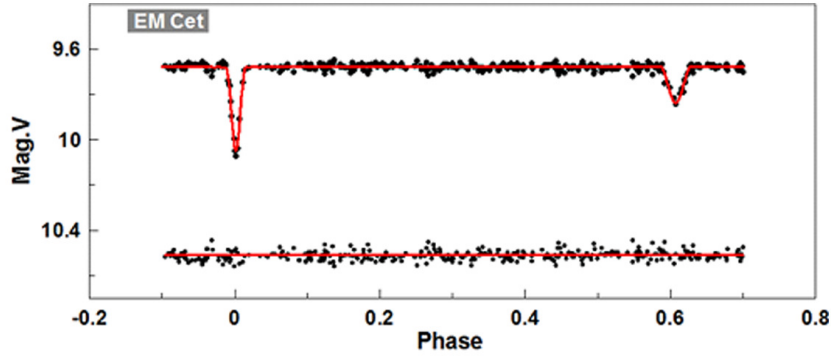


Figure 4. Top: The ASAS light curve of EM Cet and its fit. Bottom: The corresponding residuals (shifted vertically to save space).

Light curves of detached eccentric eclipsing binaries are mostly characterized by deviations of their secondary minimum from the phase 0.5. Hence, to proceed in solving the light curves, without a waste of time, one has to deduce, not guess, the initial values of both the eccentricity, e_o , and the longitude of periastron, ω_o . We follow the method of [Kjurkchieva & Vasileva \(2015a\)](#) by solving the two equations:

$$e_o \cos \omega_o = \frac{1}{2} \cdot \pi [(\phi_2 - \phi_1) - 0.5], \quad (9)$$

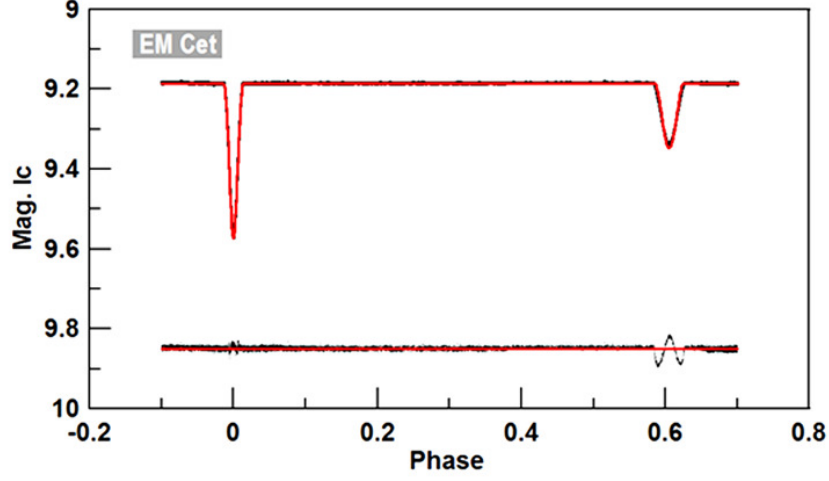


Figure 5. Top: The TESS light curve of EM Cet and its fit. Bottom: The corresponding residuals (shifted vertically to save space).

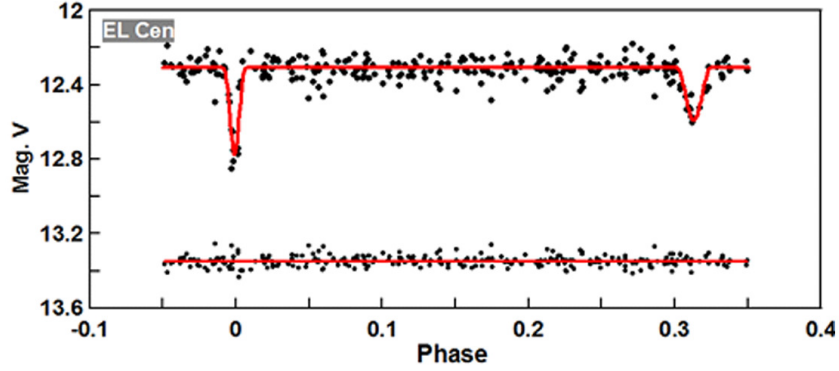


Figure 6. Top: The ASAS light curve of EL Cen and its fit. Bottom: The corresponding residuals (moved vertically to save space).

$$e_o \sin \omega_o = (W_2 - W_1)/(W_2 + W_1), \quad (10)$$

where W_1 and W_2 are the measured widths of the primary and secondary minima in phase unit; ϕ_2 is the phase of the secondary minimum, while $\phi_1 = 0$. Equations (9) and (10) are the approximate equations 9.25 and 9.37 given by

Kopal (1978). All these values are shown in Table 4. Both e_o and ω_o were used as raw parameters for PHOEBE. Also, we followed a q -search procedure implemented by several authors (e.g., Djurašević et al. (2016); Awadalla et al. (2016); El-Sadek et al. (2019)) to obtain the photometric mass ratio, q_{ph} . This can be performed by constructing the relation between the sum of weight squares deviation $(O - C)^2$ and q for both systems (Fig. 2). We obtained $q_{ph} = 0.63$ for EM Cet and 0.82 for EL Cen .

Table 4. The measured width of LC minimum, phase of sec. minimum and the estimated initial e_o and ω_o

	W_1^*	W_2^*	ϕ_2^*	e_o	ω_o (Rad.)
EM Cet _{ASAS}	0.027	0.0420	0.6080	0.2758	0.9080
EM Cet _{TESS}	0.033	0.0440	0.6074	0.2208	0.7012
EL Cen _{ASAS}	0.010	0.0216	0.3120	0.4927	0.9270

* in phase unit.

We put the deduced effective temperature, $T_{1eff.}$, as a constant parameter, and the estimated q_{ph} , e_o and ω_o as initial values. Then we proceed to the analysis by adjusting the inclination i , T_2 , surface potential of the primary and secondary components, e , ω and phase shift. We proceed step by step until the solution converges giving the best fit with the lowest value of χ^2 ($\chi^2 = 0.00528$ for EM Cet_{ASAS}, 0.0053 for EM Cet_{TESS}, and 0.0217 for EL Cen). The obtained solution parameters, including the standard errors, are shown in Table 5. In the first column of the table, the suffix 1 stands for the primary component and 2 for the secondary one. Synthetic light curves computed with these parameters are plotted as solid lines in Figs. 4, 5 and 6, with residuals at the bottom of each figure.

4. Discussion and Results

When using tables by Cox (2000), the temperatures $T_{1,2}$ (6381 & 6173(43) K) of EM Cet_{ASAS} correspond to the spectral types F7 + G7; and $T_{1,2}$ (6381 & 5899(17) K) of EM Cet_{TESS} correspond to the spectral types F7 + G3. Also, for EL Cen, $T_{1,2}$ (6841 & 6613(162) K) correspond to F3 + F 5 (see, Table 6). This result is expected considering that both stars are mainly solar-type stars. The orbital inclinations of the two targets are around 87° which is quite close to 90° . This is normally expected for eclipsing binaries with orbital periods over eight days (Kjurkchieva & Vasileva, 2015a). The light curve morphology of both systems shows partial eclipses (see also Figs. 7 & 8).

Table 5. Orbital and physical parameters of EM Cet and EL Cen.

Parameters	EM Cet _{ASAS}	EM Cet _{TESS}	EL Cen
Wavelength	5500 Å	8100 Å I central band =7865 Å	5500 Å
HJD (2400000+)	54783.709	58414.498384	53525.6
Orbit. Per. (d)	10 ^d 524	10 ^d 5242227	21 ^d 8677(4417)
Eccentricity (<i>e</i>)	0.2987(63)	0.3000(11)	0.3527(52)
ω (rad)	0.9958(149)	1.006(19)	2.538(19)
T_{1eff} (K)	6381 (fixed)	6381 (fixed)	6841 (fixed)
T_{2eff} (K)	6173(43)	5913(17)	6613(162)
Phase shift	0.0444(21)	0.04251(8)	-0.08009(92)
Orb. incl. (<i>i</i>)	87°.19 ± 0.81	87°.082 ± 0.002	87°.10 ± 0.09
Mass ratio (<i>q</i>)	0.7323(136)	0.7146(3)	0.815(42)
$l_1/(l_1 + l_2)$	0.6361(132)	0.7151(3)	0.6441(18)
$l_2/(l_1 + l_2)$	0.3638(132)	0.2849(3)	0.3559(18)
Frac. rad. r_1^*	0.0632	0.0703	0.0281
Frac. rad. r_2^*	0.0452	0.0517	0.0237
Limb dark. x_1	0.537	0.349	0.48(25)
Limb dark. x_2	0.562	0.385	0.502(225)
Surf. pot. Ω_1	17.975(340)	16.049(4)	14.00(32)
Surf. pot. Ω_2	16.752(335)	16.682(4)	13.00(37)
Fillout factor f_1	-0.812	-0.789	-0.6028
Fillout factor f_2	-0.798	-0.797	-0.5727
Albedo ALB_1	0.5	0.5	0.5
Albedo ALB_2	0.5	0.5	0.5
Grav. bright. g_1	0.32	0.32	0.32
Grav. bright. g_2	0.32	0.32	0.32
χ^2	0.0053	0.0053	0.027

* Calculated following [Ivanov et al. \(2010\)](#).

In our discussion we shall consider the obtained parameter values of EM Cet_{TESS} not EM Cet_{ASAS} to avoid any confusion for the reader. We chose the obtained parameter values of the TESS light curve rather than those of ASAS for two reasons. The first is due to the good quality of the TESS light curve compared to the ASAS light curve. The second is that the light curve by ASAS was observed during 8.8 years, while it was 27 days by the TESS. There are no radius parameters to fit in the PHOEBE code, but the radii of the components are stocked in the parameters like "PHSV" and "PCSV" (or POT1, POT2- primary and secondary surface potentials) ([Zasche, 2016](#)). However, we have obtained roughly the fractional radii from the empirical relations, assuming MS-stars given by [Ivanov et al. \(2010\)](#). We found $r_1 = 0.07032$ & $r_2 = 0.0517$ for EM Cet_{TESS} and $r_1 = 0.0281$ & $r_2 = 0.0237$ for EL Cen. These values do not provide error values, however, [Prša et al. \(2011\)](#) estimated that 90% of the sample of detached and semi-detached EBs had a corresponding error smaller

than 10% (Kjurkchieva & Vasileva, 2015b). We have attempted to study the period variation due to apsidal motion by analyzing the $O - C$ plot but we could not find an acceptable solution for the lack of the observed times of minima. For the same reason Kim et al. (2018) did not include the apsidal motion parameters of EL Cen within the eclipse timing diagram in their extensive catalogue of EEBs. The absolute physical parameters of the components were calculated using the empirical relations adopted by Harmanec (1988) and listed in Table 6. The geometrical configurations for both systems and the model solution at 0.0, 0.25, 0.50 and 0.75 orbital phases, using the Binary Maker Code (ver. 3.0), are illustrated in Figures 7 & 8. The geometrical configurations at the secondary minimum phase, ϕ_2 , at 0.6 (for EM Cet) and 0.31 (for EL Cen) are also shown at the lower panel of each figure. The partial eclipses are clearly shown.

Table 6. Orbital and physical parameters of EM Cet and EL Cen.

Star Name	Comp.	M (M_{\odot})	R (R_{\odot})	T (K)	L (L_{\odot})	$M_{bol.}$	Log g	Sp. type
EM Cet _{ASAS}	Pri.	1.271 (8)	1.347 (7)	6381	2.783 (74)	3.652 (29)	4.281 (2)	F7
	Sec.	0.971 (8)	1.051 (8)	6173 (43)	0.913 (31)	4.876 (04)	4.378 (3)	G7
EM Cet _{TESS}	Pri.	1.271 (8)	1.354 (3)	6381	2.783 (74)	3.622 (29)	4.281 (3)	F7
	Sec.	1.088 (8)	1.170 (8)	5899 (17)	1.415 (44)	4.360 (33)	4.338 (3)	G3
EL Cen	Pri.	1.438 (8)	1.496 (7)	6841	4.67 (11)	3.08 (3)	4.244 (2)	F3
	Sec.	1.365 (8)	1.432 (7)	6613 (162)	3.75 (09)	3.33 (3)	4.260 (2)	F5

The analysis shows that the orbital eccentricity of EM Cet is 0.3(0) with Sp-Type F7+G3 while for EL Cen, $e = 0.3527(52)$ with Sp-Type F3+F5, which matches Zahn (1977) and Tassoul (1988) theories of circularization, in which eccentric eclipsing binaries tending to circularize their orbits due to tidal interaction between their components. Mayer & Hanna (1991) emphasized the dependency of eccentricity evolution, towards orbital circularity, upon spectral type and the age of the binary. The obtained eccentricity and spectral type for both systems are matching the ($e - Sp.type$) diagram given by Hanna (1993) and Hanna et al. (1998).

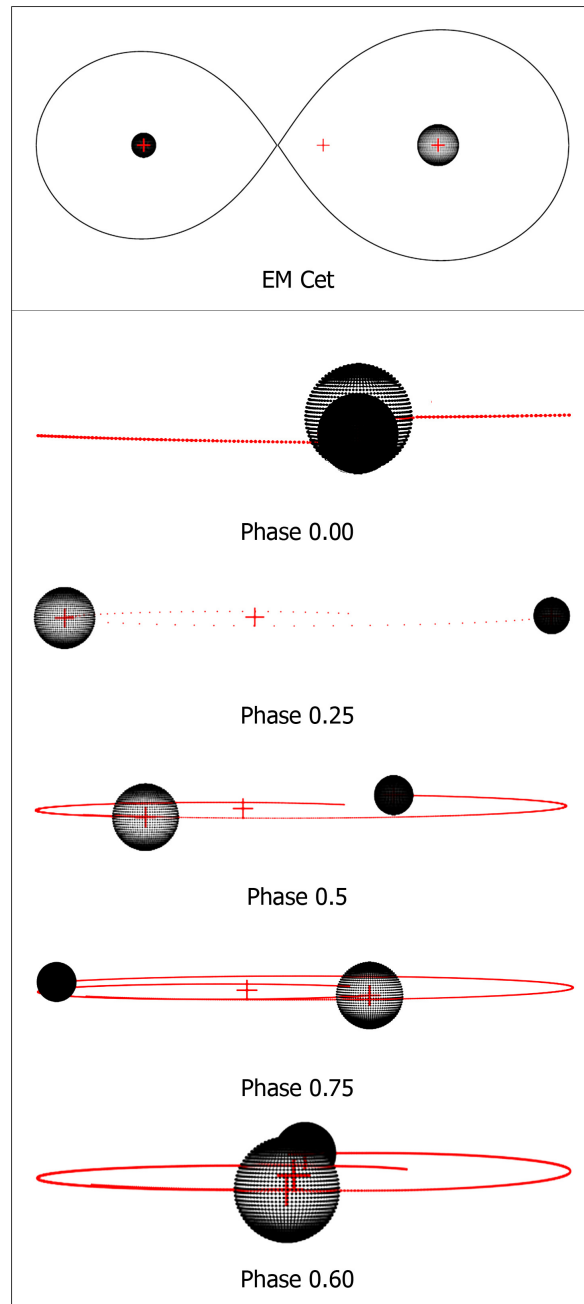


Figure 7. Top panel: Roche Lobe configuration. Bottom: The description of the model solution at different orbital phases for EM Cet.

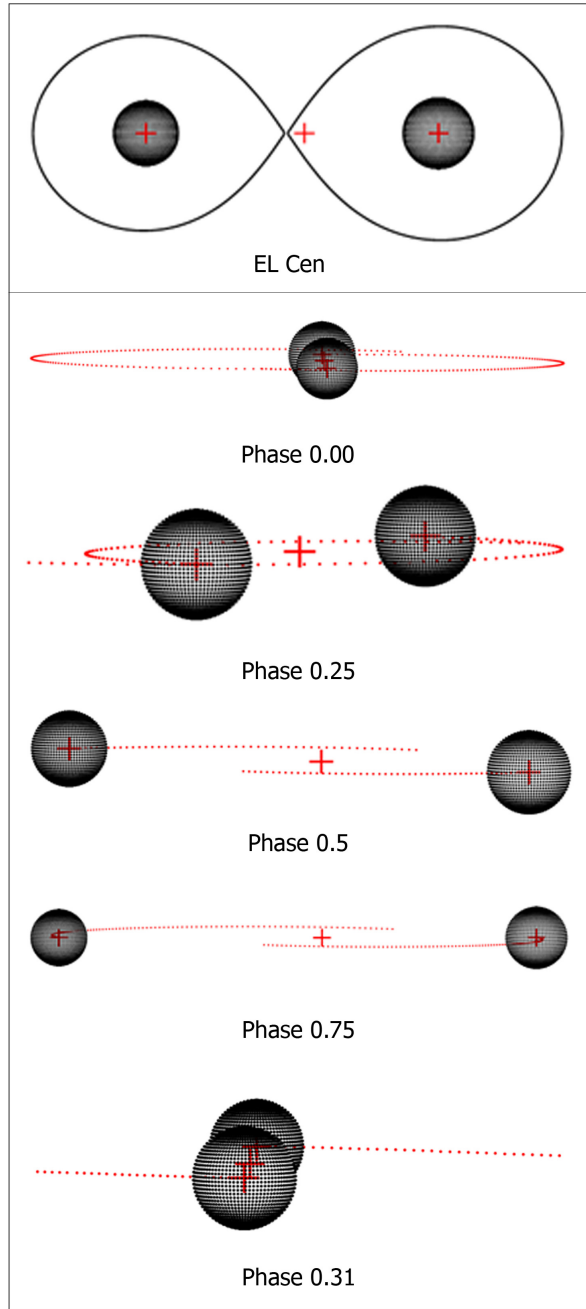


Figure 8. Top panel: Roche Lobe configuration. Bottom: The description of the model solution at different orbital phases for EL Cen.

5. Conclusion

The main results from the analysis of the two light curves are as follow:

- (1) We determined the orbital elements and stellar parameters for the two detached systems EM Cet and EL Cen.
- (2) The analysis show that EM Cet_{TESS} is of late spectral type, F7 + G3, where one can expect magnetic activity or star spots due to its convective envelope, which is a common characteristic of stars like our sun. However, we did not notice any considerable smooth or even abrupt variation in the out of eclipse range of the light curve.
- (3) The morphology of the light curves clearly shows that both systems are detached eccentric eclipsing binaries and the analysis verified significant orbital eccentricity 0.3(0) for EM Cet and 0.3527(52) for EL Cen. Also, the obtained small fractional radii are expected values for detached systems having long orbital periods.
- (4) The analysis of the light curves shows a relatively high eccentricity, $e = 0.3527(52)$, for the early type star EL Cen (Sp.type F3 + F5) rather than EM Cet of the later spectral type (F7 + G3) which has a lower eccentricity. This is consistent with tidal interaction theories that postulate the evolution of the orbit towards circularity (Mayer & Hanna, 1991).
- (5) The analysis shows a high orbital inclination of both stars $87^\circ.06 \pm 0^\circ.05$ and $87^\circ.10 \pm 0^\circ.09$ for EM Cet and EL Cen, respectively, which is expected for such long period binaries (Kjurkchieva & Vasileva, 2015a).
- (6) On comparing the two sets of parameters obtained from the analysis of the two light curves EM Cet_{ASAS} & EM Cet_{TESS}, one can notice that the differences are in the range of the estimated errors by PHOEBE for most parameters such as the eccentricity, the longitude of periastron, the inclination, the mass ratio and the phase shift. All are having almost the same values, while there is a considerable difference in T_{2eff} . by about 270 K. This may be due to the the scatter seen in the ASAS data. Also, the limb darkening coefficients x_1, x_2 for the TESS light curve are smaller by about 30% than those of the ASAS light curve. However, it is preferable to consider the results of the TESS light curve since its profile is better than the scattered light curve of ASAS, and it was observed over a shorter interval of time.

Due to the absence of spectroscopic observations, we consider the present solution as a preliminary one. Spectroscopic observations are indeed necessary for accurate determination of the absolute parameters. In addition, we recommend observing times of minima of both systems to be able to study the period variability and the apsidal motion.

Acknowledgements. This research makes use of the SIMBAD and Vizier data base, the NASA Astrophysics Data Service, the PZP catalogue, the O-C gateway, the All Sky Automated Survey (ASAS) data, the Transiting Exoplanet Satellite mission (TESS) data, and the PHOEBE software in the light curve analysis. The authors are grateful to an anonymous referee for valuable notes and propositions.





References

- Awadalla, N. S., Hanna, M. A., Ismail, M. N., Hassan, I. A., & Elkhamisy, M. A., New CCD Observations and the First Photometric Study of the Contact Binary AP UMi. 2016, *Journal of Korean Astronomical Society*, **49**, 65, DOI: 10.5303/JKAS.2016.49.3.065
- Bai, Y., Liu, J., Bai, Z., Wang, S., & Fan, D., Machine-learning Regression of Stellar Effective Temperatures in the Second Gaia Data Release. 2019, *Astronomical Journal*, **158**, 93, DOI: 10.3847/1538-3881/ab3048
- Barbera, R. 1996, AVE (Análisis de Variabilidad Estelar) Version 2.5
- Borkovits, T. & Mitnyan, T., Observational Detection of Higher-Order Secular Perturbations in Tight Hierarchical Triple Stars. 2023, *Universe*, **9**, 485, DOI: 10.3390/universe9110485
- Borkovits, T., Rappaport, S., Hajdu, T., & Sztakovics, J., Eclipse timing variation analyses of eccentric binaries with close tertiaries in the Kepler field. 2015, *Monthly Notices of the RAS*, **448**, 946, DOI: 10.1093/mnras/stv015
- Bulut, İ. & Demircan, O., A new catalogue of eclipsing binary stars with eccentric orbits*. 2007, *Monthly Notices of the RAS*, **378**, 179, DOI: 10.1111/j.1365-2966.2007.11756.x
- Cox, A. N. 2000, *Allen's astrophysical quantities*
- Cutri, R. M., Skrutskie, M. F., van Dyk, S., et al. 2003, VizieR Online Data Catalog: 2MASS All-Sky Catalog of Point Sources (Cutri+ 2003), VizieR On-line Data Catalog: II/246. Originally published in: 2003yCat.2246....0C
- Djurašević, G., Essam, A., Latković, O., et al., A Photometric Study of Four Recently Discovered Contact Binaries: 1SWASP J064501.21+342154.9, 1SWASP J155822.10-025604.8, 1SWASP J212808.86+151622.0, and UCAC4 436-062932. 2016, *Astronomical Journal*, **152**, 57, DOI: 10.3847/0004-6256/152/3/57
- El-Sadek, M. A., Djurašević, G., Essam, A., et al., A photometric study of two recently discovered, contact binaries-II: UCAC4 479-113658 and UCAC4 479-113711. 2019, *New Astronomy*, **69**, 21, DOI: 10.1016/j.newast.2018.11.006
- ESA, ed. 1997, ESA Special Publication, Vol. **1200**, *The HIPPARCOS and TYCHO catalogues. Astrometric and photometric star catalogues derived from the ESA HIPPARCOS Space Astrometry Mission*
- Hanna, M. 1993, Binary Stars and their Orbital Eccentricities, Unpublished, Charles University, Praha, Czech Republic., PhD thesis
- Hanna, M., Mayer, P., & Hanna, Y., Circularization of Binary Orbits. 1998, *Astrophysics and Space Science*, **262**, 171
- Harmanec, P., Stellar Masses and Radii Based on Modern Binary Data. 1988, *Bulletin of the Astronomical Institutes of Czechoslovakia*, **39**, 329
- Hegedüs, T., Giménez, A., & Claret, A., Eccentric Eclipsing Binary Systems - the Updated Catalogue. 2005, in Astronomical Society of the Pacific Conference Series, Vol. **333**, *Tidal Evolution and Oscillations in Binary Stars*, ed. A. Claret, A. Giménez, & J. P. Zahn, 88

- Hoffleit, D., Variables in Milky Way Field 167. 1930, *Harvard College Observatory Bulletin*, **874**, 13
- Høg, E., Fabricius, C., Makarov, V. V., et al., The Tycho-2 catalogue of the 2.5 million brightest stars. 2000, *Astronomy and Astrophysics*, **355**, L27
- Ivanov, V. P., Kjurkchieva, D. P., & Srinivasa Rao, M., Light curve solutions of eclipsing binaries in SMC. 2010, *Bulletin of the Astronomical Society of India*, **38**, 83, DOI: 10.48550/arXiv.1011.1986
- Kazarovets, E. V. & Pastukhova, E. N., New Elements for 34 NSV and GCVS Stars. 2017, *Peremennye Zvezdy Prilozhenie*, **17**, 2
- Kazarovets, E. V., Samus, N. N., Durlevich, O. V., et al., The 74th Special Name-list of Variable Stars. 1999, *Information Bulletin on Variable Stars*, **4659**, 1
- Khruslov, A. V., New Elements of Known Variables. 2012, *Peremennye Zvezdy Prilozhenie*, **12**, 8
- Kim, C. H., Kreiner, J. M., Zakrzewski, B., et al., A Comprehensive Catalog of Galactic Eclipsing Binary Stars with Eccentric Orbits Based on Eclipse Timing Diagrams. 2018, *Astrophysical Journal, Supplement*, **235**, 41, DOI: 10.3847/1538-4365/aab7ef
- Kirk, B., Conroy, K., Prša, A., et al., Kepler Eclipsing Binary Stars. VII. The Catalog of Eclipsing Binaries Found in the Entire Kepler Data Set. 2016, *Astronomical Journal*, **151**, 68, DOI: 10.3847/0004-6256/151/3/68
- Kjurkchieva, D. & Vasileva, D., Light Curve Solutions of Ten Eccentric Kepler Binaries, Three of them with Tidally Induced Humps. 2015a, *Publications of the Astron. Soc. of Australia*
- Kjurkchieva, D. & Vasileva, D., Light curve solutions of the eccentric Kepler binaries KIC 11619964 and KIC 7118545 and mid-eclipse brightening of KIC 11619964. 2015b, *Bulgarian Astronomical Journal*, **23**, 75, DOI: 10.48550/arXiv.1507.06072
- Kjurkchieva, D., Vasileva, D., & Atanasova, T., Orbital Parameters of the Eclipsing Detached Kepler Binaries with Eccentric Orbits. 2017, *Astronomical Journal*, **154**, 105, DOI: 10.3847/1538-3881/aa83b3
- Kopal, Z. 1978, *Dynamics of close binary systems(Book). Dordrecht, D. Reidel Publishing Co. (Astrophysics and Space Science Library), 68, 524*
- Lucy, L. B., Gravity-Darkening for Stars with Convective Envelopes. 1967, *Zeitschrift fuer Astrophysik*, **65**, 89
- Mayer, P. & Hanna, M. A. M., Eclipsing Binaries with Eccentric Orbits. 1991, *Bulletin of the Astronomical Institutes of Czechoslovakia*, **42**, 98
- Nedoroščík, J., Vaňko, M., & Pribulla, T., Eclipsing binaries in the ASAS survey. 2014, *Contributions of the Astronomical Observatory Skalnaté Pleso*, **43**, 465
- Paschke, A. & Brat, L., O-C Gateway, a Collection of Minima Timings. 2006, *Open European Journal on Variable Stars*, **23**, 13
- Petrova, A. V. & Orlov, V. V., Apsidal Motion in Double Stars. I. Catalog. 1999, *Astronomical Journal*, **117**, 587, DOI: 10.1086/300671

- Pojmanski, G., The All Sky Automated Survey. 1997, *Acta Astronomica*, **47**, 467, DOI: 10.48550/arXiv.astro-ph/9712146
- Pojmanski, G., The All Sky Automated Survey. Catalog of Variable Stars. I. 0 h - 6 h Quarter of the Southern Hemisphere. 2002, *Acta Astronomica*, **52**, 397, DOI: 10.48550/arXiv.astro-ph/0210283
- Prša, A., Batalha, N., Slawson, R. W., et al., Kepler Eclipsing Binary Stars. I. Catalog and Principal Characterization of 1879 Eclipsing Binaries in the First Data Release. 2011, *Astronomical Journal*, **141**, 83, DOI: 10.1088/0004-6256/141/3/83
- Prša, A. & Zwitter, T., A Computational Guide to Physics of Eclipsing Binaries. I. Demonstrations and Perspectives. 2005, *Astrophysical Journal*, **628**, 426, DOI: 10.1086/430591
- Rappaport, S. A., Borkovits, T., Gagliano, R., et al., A study of nine compact triply eclipsing triples. 2023, *Monthly Notices of the RAS*, **521**, 558, DOI: 10.1093/mnras/stad367
- Rappaport, S. A., Borkovits, T., Mitnyan, T., et al., Seven new triply eclipsing triple star systems. 2024, *Astronomy and Astrophysics*, **686**, A27, DOI: 10.1051/0004-6361/202449273
- Ricker, G. R., Winn, J. N., Vanderspek, R., et al., Transiting Exoplanet Survey Satellite (TESS). 2015, *Journal of Astronomical Telescopes, Instruments, and Systems*, **1**, 014003, DOI: 10.1117/1.JATIS.1.1.014003
- Ruciński, S. M., The W UMA-type Systems as Contact Binaries. I. Two Methods of Geometrical Elements Determination. Degree of Contact. 1973, *Acta Astronomica*, **23**, 79
- Slawson, R. W., Prša, A., Welsh, W. F., et al., Kepler Eclipsing Binary Stars. II. 2165 Eclipsing Binaries in the Second Data Release. 2011, *Astronomical Journal*, **142**, 160, DOI: 10.1088/0004-6256/142/5/160
- Tassoul, J.-L., On Orbital Circularization in Detached Close Binaries. 1988, *Astrophysical Journal, Letters*, **324**, L71, DOI: 10.1086/185094
- Watson, C. L., Henden, A. A., & Price, A., The International Variable Star Index (VSX). 2006, *Society for Astronomical Sciences Annual Symposium*, **25**, 47
- Zahn, J. P., Tidal friction in close binary systems. 1977, *Astronomy and Astrophysics*, **57**, 383
- Zasche, P., PHOEBE - step by step manual. 2016, *Open European Journal on Variable Stars*, **176**, 10
- Zhang, L.-y., Su, T., Misra, P., et al., Stellar Parameters and Spectroscopic Properties of TESS Objects Observed in the LAMOST Low- and Medium-resolution Spectral Survey. 2023, *Astrophysical Journal, Supplement*, **264**, 17, DOI: 10.3847/1538-4365/ac9b28

Deep investigation of a pair of open clusters NGC 7031 and NGC 7086 utilizing Gaia DR3

A.A. Haroon^{1,4}, W.H. Elsanhoury^{2,4}, A.S. Saad^{3,4} and
E.A. Elkholy^{2,4}

¹ *Astronomy and Space Science Department, Faculty of Science, King Abdulaziz University, Jeddah, Saudi Arabia (E-mail: aaharoon@kau.edu.sa)*

² *Department of Physics, College of Science, Northern Border University, Arar, Saudi Arabia (E-mail: elsanhoury@nbu.edu.sa)*

³ *Operations Management Department, College of Business and Economics, Qassim University, Buraidah 51452, Qassim, Saudi Arabia (E-mail: rmthaan@qu.edu.sa)*

⁴ *Astronomy Department, National Research Institute of Astronomy and Geophysics (NRIAG), 11421, Helwan, Cairo, Egypt (E-mail: elsanhoury@nriag.sci.eg)*

Received: March 21, 2024; Accepted: June 12, 2024

Abstract. In this paper, we carried out photometric and kinematic study of two poorly studied open clusters NGC 7031 and NGC 7086 utilizing the optical wavelength of Gaia DR3. We identified 613 and 226 candidates for respective clusters as highly probable astrometric members. Fitting King’s profile within RDPs, we estimate both core and limiting radii. For each cluster, we construct CMDs and fit them with suitable isochrones with metallicities ($Z = 0.01189 \pm 0.00023$ & 0.01121 ± 0.00025) and different ages (8.468 ± 0.007 & 8.617 ± 0.021 ; $\log \text{yr}^{-1}$), therefore, the heliocentric distances are 701 ± 26 & 942 ± 31 pc for NGC 7031 and NGC 7086, respectively. Moreover, the collective mass (M_C) in solar mass units may be deduced with MLR of 1072 ± 33 & 598 ± 25 and LF concluded that the average absolute (M_G) magnitudes are 7.51 ± 0.36 & 6.54 ± 0.39 for respective clusters. The overall mass function reflects the slopes (α) for Salpeter’s value (2.35) within the uncertainty, i.e., $\alpha_{\text{NGC 7031}} = 2.73 \pm 0.25$ & $\alpha_{\text{NGC 7086}} = 2.67 \pm 0.32$.

The present study and the dynamical analysis for different evolving times demonstrate that the clusters are dynamically relaxed, where the dynamical evolution parameter $\tau \gg 1$. According to a kinematical analysis, we have obtained that the coherent convergent point (A_o, D_o) is $(-83^\circ.99 \pm 0^\circ.11, -24^\circ.02 \pm 0^\circ.20$; NGC 7031) & $(-80^\circ.69 \pm 0^\circ.11, -17^\circ.51 \pm 0^\circ.24$; NGC 7086). Finally, we have computed their linear separation distance to be about 55.08 ± 7.42 pc, which reflects that the clusters are not binary and/or pair clusters.

Key words: open clusters: NGC 7031 and 7086 – astrometric – color magnitude diagrams CMDs – photometric – kinematics

1. Introduction

Open star clusters (OCs) are uniform stellar systems with abundant gas and dust that originated along the Galactic plane under identical physical scenarios. They are found in varied ranges of stellar mass but contain tens to a few thousand stars spread across comparable distances, ages, and initial chemical compositions. As a result, each of these systems makes an excellent laboratory for researching the creation and evolution of stars, and it may be utilized to test and constrain theories regarding stellar evolution (Joshi et al., 2016). In addition to offering details on the physics, motion, and development of stars, OCs also show the Milky Way’s disk structure (Kharchenko et al., 2013). Because of their ability to accurately determine the amount of interstellar reddening towards them, their chemical abundances, distances, and ages, OCs are a great tool for studying the structural, dynamic, and chemical evolution of the galaxy. This is demonstrated by the ability to create two-color diagrams (TCDs) and color-magnitude diagrams (CMDs) from UBV photometric data, and then compare these diagrams with stellar models and isochrones.

According to earlier studies, the percentage of OCs in gravitationally interacting pairs¹ is not insignificant in this situation (Angelo et al., 2022). At a distance of 50–60 kpc, the Magellanic Clouds (MCs) make it simple to identify binary clusters (Hatzidimitriou & Bhatia, 1990). It appears from studies of the Large Magellanic Cloud (LMC) and Small Magellanic Cloud (SMC) that about 10% of clusters are binary and/or pair clusters (Pietrzynski & Udalski, 2000) far from each other appearing to be close due to a viewing angle (Conrad et al., 2017). Some research (Subramaniam et al., 1995) has found that the Milky Way’s binary cluster percent age is less than this ($\sim 8\%$; 18 probable pairs) and stated that a cluster pair is termed a binary cluster if the separation is ≤ 20 pc.

Also, de La Fuente Marcos & de La Fuente Marcos (2009) used information from the Dias et al. (2002) and WEBDA² (Netopil et al., 2012) catalogs for a volume-limited sample of OCs that were situated at the solar circle. They used the physical (as opposed to projected) separation between pairs of OCs as their primary selection criterion, presuming that two objects are part of an interacting system when their separation is less than three times the average tidal radius (r_t) for clusters in the Milky Way disc ~ 10 pc (Binney & Tremaine, 2008). Based on the results of their process, they concluded that, like what has been proposed for the Magellanic Clouds (e.g., Bhatia & Hatzidimitriou (1988); Hatzidimitriou & Bhatia (1990); Pietrzynski & Udalski (2000); Dieball et al. (2002)), at least $\sim 10\%$ of all OCs seem to be involved in some kind of interaction with another cluster.

¹The term "pairs" is used simply to describe either unbound or gravitationally bound groups of interacting OCs or even random alignments in the sky. The term "binary cluster" is specifically used to refer to clusters of two OCs that are gravitationally bonded.

²<https://webda.physics.muni.cz/>

Table 1. Astrophysical parameters of NGC 7031 and NGC 7086, which were derived from the literature; (1)Dias et al. (2002), (2)Svolopoulos (1961), (3)Hoag et al. (1961), (4)Lindoff (1968), (5)Hassan & Barbon (1973), (6)Kopchev & Petrov (2008), (7)Yontan et al. (2019), (8)Hassan (1967), (9)Rosvick & Robb (2006), (10)Hunt & Reffert (2024).

α_{2000} [h m s]	δ_{2000} [$^{\circ}$ ' '']	l [$^{\circ}$]	b [$^{\circ}$]	$E(B - V)$ [mag]	$m - M$ [mag]	Distance [pc]	$\log t$ [yr $^{-1}$]	d_{Gaia} [pc]	μ_{α}^* [mas yr $^{-1}$]	μ_{δ} [mas yr $^{-1}$]	Ref.
Cluster: NGC 7031											
21 07 12.00	50 52 30	91.33	2.31	0.854	-	900	8.138	-	-2.87 \pm 0.20	-4.77 \pm 0.11	(1)
				1.03	12.60	760	-	-	-	-	(2)
21 08.20 0	50 42 0.0	91.62	2.04	0.85	12.41	900	8.14	-	-	-	(3)
				-	12.25	910	7.75	-	-	-	(4)
21 05.70 0.0	50 38 0.0	91.03	2.30	0.71-0.84	11.45-11.70	730-686	8.68	-	-	-	(5)
				1.05 \pm 0.05	9.60 \pm 0.20	831 \pm 72	8.35	-	-	-	(6)
				0.93 \pm 0.08	13.30 \pm 0.25	1212 \pm 146	7.81 \pm 0.03	1414 \pm 81	-1.286 \pm 0.081	-4.144 \pm 0.076	(7)
21 07 12.76	50 51 56.20	91.65	2.24	0.973	10.756	1416	7.562	-	-1.243 \pm 0.008	-4.281 \pm 0.010	(10)
Cluster: NGC 7086											
21 30 27.0	51 36 0.0	94.41	0.22	0.807	-	1298	8.142	-	0.98 \pm 1.56	0.22 \pm 1.44	(1)
21 29.40 0	51 27 0.0	94.48	0.24	0.69	12.40	1170	8.87	-	-	-	(8)
				-	12.50	1205	7.93	-	-	-	(4)
21 30 30	51 36 0.0	94.40	0.20	0.83 \pm 0.02	13.40 \pm 0.30	1500	8.00	-	-	-	(9)
				0.75 \pm 0.05	9.90 \pm 0.20	955 \pm 84	8.25 \pm 0.06	-	-	-	(6)
				0.75 \pm 0.07	13.37 \pm 0.23	1618 \pm 182	8.18 \pm 0.07	1684 \pm 140	-1.642 \pm 0.086	-1.644 \pm 0.076	(7)
21 30 30.66	51 35 34.10	94.76	0.19	0.991	11.129	1681	8.183	-	-1.653 \pm 0.005	-1.664 \pm 0.004	(10)

In the present work, we carried out the extensive astrometric, photometric, and kinematic analysis of a poorly studied pair and/or binary clusters NGC 7031 (known as Collinder 430, FSR 294, MWSC 3466, NGC 7031, OCL 210, or Theia 2164) and NGC 7086 (known as Collinder 437, FSR 309, MWSC 3520, NGC 7086, OCL 214, or Theia 2737) open clusters (Hunt & Reffert, 2023), which are located very near to the disc of the Milky Way (MW) according to Gaia Mission Collaborations data release 3 Gaia Collaboration (2022). Table 1 presents the the fundamental and astrophysical parameters of NGC 7031 and NGC 7086, which are derived from the literature like Dias et al. (2002), Svolopoulos (1961), Hoag et al. (1961), Lindoff (1968), Hassan & Barbon (1973), Kopchev & Petrov (2008), Yontan et al. (2019), Hassan (1967), Rosvick & Robb (2006), and Hunt & Reffert (2024).

In what follows, Section 2 describes the Gaia DR3 data we used. The structural analysis of the OCs is given in Section 3 followed by the discussion and selection of the probable members to construct CMDs in Section 4 with various photometric parameters. Luminosity, mass functions, and mass segregation are described in Section 5. Section 6 deals with evolving times and escape velocity. The ellipsoidal motion and the kinematical structure are presented in Section 7. We close finally with conclusions in Section 8.

2. Data sample

In this study, we have extracted our target with the aid of the most recent Gaia mission collaborations data release 3 of Gaia Collaboration (2022) to get the astrometric data. A new era in astronomy began with the launch of the European Space Agency (ESA) mission Gaia as it contains the five-parameter astrometry for approximately 1.8 billion sources along their position in the sky (α , δ), parallaxes (π ; mas) and the right ascension and declination components of the proper motion (μ_α^* , μ_δ ; mas yr⁻¹)³ with limiting magnitude of $G = 21$ mag. With uncertainties in the respective proper motion, components are up to 0.02 – 0.03 mas yr⁻¹ (at $G < 15$ mag), 0.07 mas yr⁻¹ (at $G \sim 17$ mag), 0.50 mas yr⁻¹ (at $G \sim 20$ mag) and 1.40 mas yr⁻¹ (at $G = 21$). The uncertainties in the parallax values are $\sim 0.02 - 0.03$ mas for sources with $G < 15$ mag, ~ 0.07 mas for sources with $G = 17$ mag, ~ 0.50 mas at $G = 20$ mag, and ~ 1.30 mas at $G = 21$. The DR3 is complemented with data of the radial velocity (V_r) for about 7 million stars from DR2 Gaia Collaboration et al. (2021). The source list has a slight change to DR2 with some notable changes. The significant advance of DR3 over DR2 is the large improvement in the accuracy of the astrometric parameters; a factor of 2.00 in the proper motion accuracy and a factor of about 1.50 in the parallax accuracy. Astrometric errors were suppressed by 30 – 40% for the parallax and by a factor of 2.50 for the proper motion.

³($\mu_\alpha^* = \mu_\alpha \cos \delta$)

In our calculations, the downloaded data was taken from the Gaia DR3 catalog of [Gaia Collaboration \(2022\)](#). Although the apparent diameters of these two open clusters are about 14.0 and 12.0 arcmin, respectively, we need to download the data diameter of both by about 20 arcmin to reach the background field stars. Therefore, we get from the Gaia DR3 catalog a complete worksheet data including the angular distance from the center, right ascension, and declination for G mag for NGC 7031 and NGC 7086.

3. Structural analysis of the open clusters

The initial phase of analyzing a cluster involves determining its structural attributes, such as the central coordinates and the outermost boundary. Despite some catalogs providing this information, the accuracy of the listed centers and sizes is not always reliable. For the analysis of structural and essential characteristics in this research, we consistently employ the ASteCA software suite. This package has been utilized in the examination of numerous clusters in previous studies and has yielded outstanding outcomes, e.g. [Perren et al. \(2020\)](#).

3.1. Determination of the new center of the clusters

In contrast to globular clusters where the center is typically clear to the naked eye, the core of an OC might not be as easily discernible. The Automated Stellar Cluster Analysis (ASteCA) code of [Perren et al. \(2015\)](#) employs a widely used technique to ascertain an OC's central coordinates by identifying the point with the highest spatial density. This is achieved by fitting a two-dimensional Gaussian kernel density estimator (KDE) to the cluster's spatial layout. What sets ASteCA apart from similar methods is its ability to operate without preset initial values, though they can be provided for semi-automatic operation. The tool ensures consistent convergence. This approach is less dependent on the binning of the area because it determines the KDE's bandwidth using Scott's rule [Scott \(1992\)](#), a recognized standard. It also simultaneously calculates the maximum density estimate in both spatial dimensions, reducing the impact that densely packed areas might have on pinpointing the central coordinates. Moreover, the process is adaptable to various coordinate systems and is equally effective with data expressed in pixels or degrees.

Figure 1 represents the re-estimated center using the ASteCA method (as well as the images of the clusters taken from the STScI Digitized Sky Survey⁴). According to our analysis, the new centers of NGC 7031 are less by about $0^{\circ}.1564$ in right ascension and exceeded by about $0^{\circ}.0013$ in declination, and in the same manner for NGC 7086 our obtained right ascension is less by about $0^{\circ}.0153$ in right ascension and exceed with $0^{\circ}.083$ in declination as compared with those obtained with [Dias et al. \(2002\)](#) and WEBDA. Table 2 reports the updated

⁴https://archive.stsci.edu/cgi-bin/dss_form

centers of the clusters in the equatorial (α , δ) and Galactic (l , b) coordinate systems. Figure 2 displays in three photometric bands G , G_{BP} , and G_{RP} the uncertainty in photometric magnitudes 0.05 for $G \leq 21$ mag.

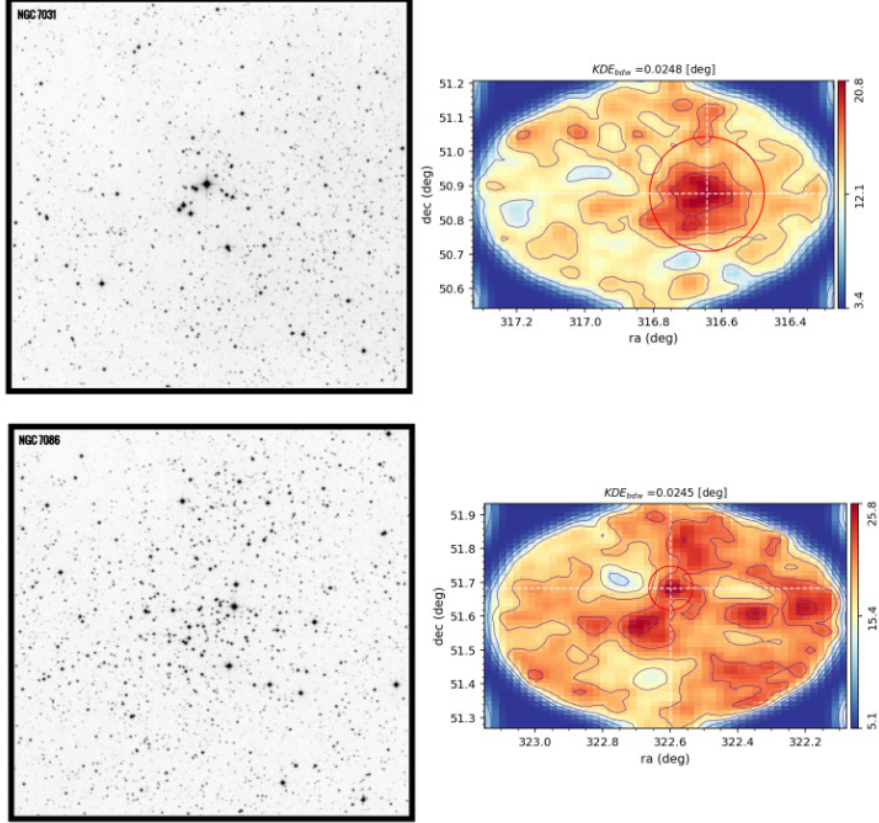


Figure 1. The images (left panel) and the contour maps (right panel) show the centers according to the Kernel density estimation technique (KDE) applied by AStCa of both NGC 7031 (top) and NGC 7086 (bottom).

3.2. Radial stellar surface density and cluster radii

To investigate the inner structural parameters of NGC 7031 and NGC 7086, we analyze the radial density profiles (RDP). The RDP is often calculated by dividing the number of stars that lie inside each ring by its area, and then creating concentric circular rings around the designated cluster center with increasing radius values, i.e., the observable regions of each cluster were divided into many

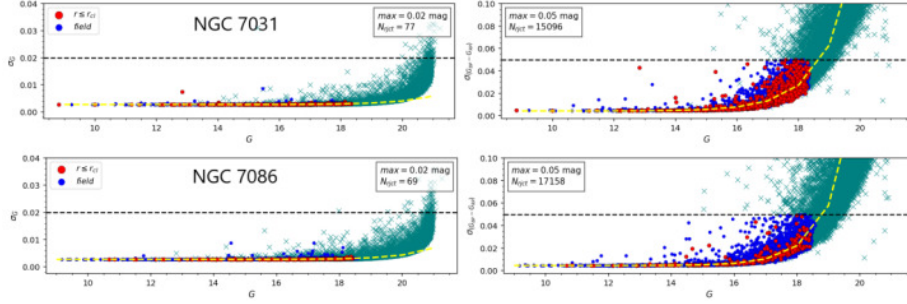


Figure 2. Photometric uncertainties in Gaia bands (G , G_{BP} , and G_{RP}) with G magnitudes which are used to clean the cluster field stars by rejection stars (the green x symbol) with uncertainties more than 0.02 in G mag and 0.05 in color-magnitude $G_{BP}-G_{RP}$, respectively.

Table 2. Our new center estimate of NGC 7031 and NGC 7086.

Coordinates	NGC 7031	NGC 7086
α	21 ^h 06 ^m 34 ^s .46	21 ^h 30 ^m 23 ^s .33
δ	50 ^d 52 ^m 35 ^s .08	51 ^h 40 ^m 59 ^s .20
l°	91 ^o .5932	94 ^o .8009
b°	2 ^o .3251	0 ^o .2690

concentric rings that centered around the cluster center. The number density (r_i) in the i th zone may be found using the formula ($r_i = N_i/A_i$), where (N_i) is the number of stars and (A_i) is the i th zone's area. First, we adopted the new central coordinates of the clusters as given in Table 2 and downloaded new row data with 14.00 and 12.00 arcmin for both clusters respectively with Gaia DR3 and then, following Perren et al. (2015), generated concentric square rings using an underlying 2D histogram or grid in the observed frame's positional space. This positional histogram's bin width is equal to 1% of the spatial dimension that covers the smallest range in the observed frame. Therefore, for each cluster, the fitted RDP could be utilized with King's profile (King, 1962) equation,

$$\rho(r) = f_{bg} + \frac{f_o}{1 + (r/r_c)^2}, \quad (1)$$

where f_o is the central surface density (i.e., maximum density), f_{bg} is the background surface density, and r_c is the core radius (distance from the obtained center to the point at which the value of $\rho(r)$ becomes half of the central density f_o). As seen in Figure 3, we created two RDPs using King's model for both clusters, which was fitted using Equation (1). Table 3 lists our obtained results with RDPs of NGC 7031 and NGC 7086.

Comparing our results of f_o and f_{bg} with those of [Yontan et al. \(2019\)](#), we found a large difference between our and their results in central and background densities in both clusters. We claim that their results are not reliable because the values of f_o are less than f_{bg} , which is not consistent with the King model; rather than their results depend on Gaia DR2, which clear from Figure 3 of [Yontan et al. \(2019\)](#). So, we are satisfied with our results from RDP (Figure 3) using the recent data of Gaia DR3, which is consistent with the King model (i.e., $f_o > f_{bg}$). Therefore, their error in estimating the King model fitting parameters (i.e., f_o , f_{bg} , and r_c) on both clusters may reflect on core, limiting, and tidal radii.

The limiting radius (r_{cl} ; arcmin) in expansion may be defined as the point into which the gravitational pull from the Galaxy center as well as the gravitational acceleration from the cluster center ([von Hoerner, 1957](#)). r_{cl} was calculated by comparing $\rho(r)$ to a background density level ρ_b (i.e., $\rho_b = f_{bg} + 3\sigma_{bg}$), where the uncertainty of f_{bg} is σ_{bg} . The following formula provides the value of r_{cl} ([Bukowiecki et al., 2011](#)).

$$r_{cl} = r_c \sqrt{\frac{f_o}{3\sigma_{bg}} - 1}. \quad (2)$$

According to Table 3, we found a difference in numerical values of the core radius (r_c) for both clusters as compared with those obtained by [Hunt & Reffert \(2024\)](#), which may account for the difference in the distance and the number of members.

3.3. Tidal radii

According to [von Hoerner \(1957\)](#), the tidal radius is the distance from the cluster center at which the gravitational acceleration created by the cluster equals the tidal acceleration caused by the parent galaxy. [Jeffries et al. \(2001\)](#) have introduced a relation between the tidal radius (r_t ; pc) and the total mass (M_C ; M_\odot) as (see section 5)

$$r_t = 1.46 \sqrt[3]{M_C}. \quad (3)$$

Our estimated values of tidal radii (pc) for both clusters NGC 7031 and NGC 7086 are 14.94 ± 0.26 and 12.30 ± 0.29 , respectively.

Empirically, the limiting radius lags between 2 – 7 times the core radius. Therefore, we obtained values of 10.04 and 3.91 arcmin for NGC 7031 and NGC 7086, respectively. On the other hand, other inner structural parameters may be deduced for OCs. First, the concentration parameter ($C = r_{cl}r_c$) [King \(1966\)](#) defined the C as the ratio of the cluster limiting and core radii and can be indicated by the concentration of the cluster's center. [Santos-Silva & Gregorio-Hetem \(2012\)](#) reversed King's definition of the C parameter from [King \(1966\)](#) and expect that young clusters will have low C values since many of their

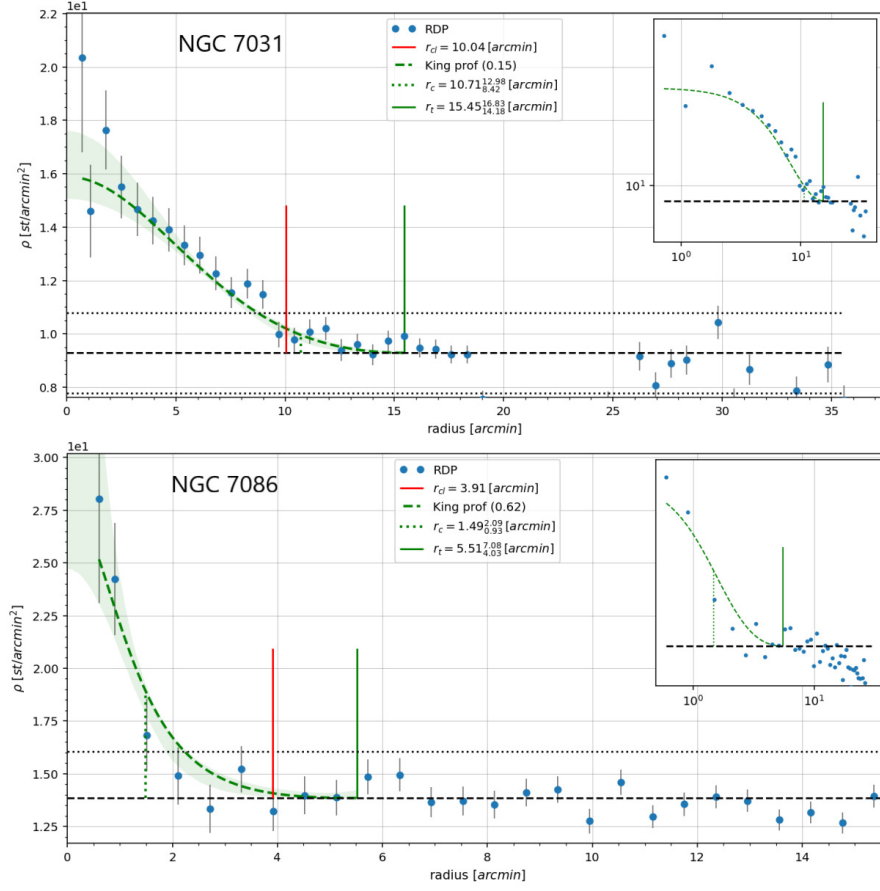


Figure 3. The RDPs of both NGC 7031 (top) and NGC 7086 (bottom). The dashed green lines were applied with the King’s density distribution model, the horizontal dashed lines denote the background field density (f_{bg} ; stars arcmin^{-1}). The vertical dotted green lines, vertical solid red lines, and vertical solid green lines indicate the cluster core (r_c), limiting (r_{cl}), and tidal (r_t) radii (in arcmin), respectively.

members are still concentrated in the center and haven’t had enough time to spread out of their borders. Based on Table 3, we arrived at a reasonable C range (Santos-Silva & Gregorio-Hetem, 2012) as 1.20 ± 0.08 and 4.20 ± 0.49 . Second, Bonatto & Bica (2009) defined density parameters for compact OCs known as the density contrast parameter (i.e., $\delta_c = 1 + f_o f_{bg}$) and give values $7 \leq \delta_c \leq 23$. Our computed δ_c are 2.760 ± 0.60 and 2.986 ± 0.58 for both clusters respectively, and we may conclude that NGC 7031 and NGC 7086 are scattered concerning their background density.

Table 3. Our inner structural properties of NGC 7031 and NGC 7086 as compared with (1) Yontan et al. (2019) and (2) Hunt & Reffert (2024).

Parameters	NGC 7031	NGC 7086	References
$(f_o; \text{stars arcmin}^{-2})$	16.319 ± 0.780	24.366 ± 5.473	Current work
	1.978 ± 0.059	3.602 ± 0.280	(1)
$(f_{bg}; \text{stars arcmin}^{-2})$	9.276 ± 0.402	12.381 ± 0.228	Current work
	4.006 ± 0.443	5.009 ± 0.171	(1)
$(r_c; \text{arcmin})$	$10.71_{8.42}^{12.98}$	$1.49_{0.93}^{2.09}$	Current work
	3.241 ± 1.816	1.517 ± 0.255	(1)
$(r_c; \text{pc})$	2.19 ± 0.68	0.41 ± 0.02	Current work
	2.23	2.51	(2)
$(r_{cl}; \text{arcmin})$	10.04	3.91	Current work
$(r_{cl}; \text{pc})$	2.05 ± 0.70	1.08 ± 0.03	Current work
	9.97	10.66	(2)
$(r_t; \text{arcmin})$	$15.45_{14.18}^{16.83}$	$5.51_{4.03}^{7.08}$	Current work
$(r_t; \text{pc})$	3.16 ± 0.56	1.51 ± 0.18	Current work
	9.974	10.656	(2)
C	1.20 ± 0.08	4.20 ± 0.49	Current work
δ_c	2.760 ± 0.60	2.986 ± 0.58	Current work

4. CMDs and member stars of the clusters

The highly accurate determination of cluster star members can be achieved by combining radial velocities, distances, and proper motions, either alone or in combination. Large spectroscopic surveys created for various objectives can now be used to identify cluster members (Allende Prieto et al. (2008); Gilmore et al. (2012); De Silva et al. (2015)). Spectroscopic observations require a telescope-time-focused methodology, which limits our ability to comprehend the characteristics of several clusters. Furthermore, no spectroscopic survey to determine the radial velocities of all Milky Way stars is scheduled. Fortunately, many techniques exist to distinguish cluster members from field stars because cluster stars share the same spatial origin (e.g. Krone-Martins & Moitinho (2014); Javakhishvili et al. (2006); Balaguer-Núñez et al. (1998)). These techniques typically consider the proper motions of the stars.

Perren et al. (2015) with the ASteCA code used two methods to estimate the overall number of likely cluster members. The first uses the integral of the RDP from zero to r_t above the estimated star field density and is based on the three-parameter (3P) King profile fitting. Only a decent tidal radius and convergence of the 3P fit are required for this method to be effective; otherwise, the result may be greatly overestimated. The second method is based on a straightforward star count (n_{fl}), or the approximate number of field stars inside the cluster region, is obtained by multiplying the field density value (d_{field}) by the area (A_{cl}) of the cluster (which is determined by the r_{cl} radius). After deducting this

amount from the actual number of stars inside the r_{cl} boundary (n_{cl+fl}), the final estimated number of cluster members, n_{cl} , is obtained:

$$n_{cl} = n_{cl+fl} - d_{field} A_{cl}. \quad (4)$$

Both approaches depend on the degree of completeness since they provide the approximate number of members down to the lowest observed magnitude.

By looking for a significant stellar over-density and contrasting it with the surrounding stellar field, the membership probability is assigned using the proper motion and parallax that are accessible from the Gaia DR3 database with the ASteCA code. In this investigation, the cluster most probable candidates are limited to stars with membership probabilities $P \geq 50\%$. As a result, we have 613 and 226 candidates for NGC 7031 and NGC 7086, respectively.

We employed the ASteCA code and the PARSEC v1.25 of [Bressan et al. \(2012\)](#) theoretical isochrones for each CMD of the clusters, as well as the Gaia DR3 photometric magnitudes (G, G_{BP}, G_{RP}) for our candidates, to derive the cluster metallicity (Z) and ages (in a log scale). Therefore, the best-suited metallicities are 0.01189 ± 0.00023 & 0.01121 ± 0.00025 and the ages ($\log \text{yr}^{-1}$) are 8.468 ± 0.007 & 8.617 ± 0.021 for NGC 7031 and NGC 7086, respectively. Our fitted CMDs for ($G_{BP} - G_{RP}, G$) mag are shown in Figure 4.

We approximated the reddening with magnitudes G_{BP} and G_{RP} from CMDs using most likely members from Gaia DR3 using the formula $E(G_{BP} - G_{RP}) = 1.289 \times E(B - V)$ ([Cardelli et al., 1989](#)). After correcting the observed data for reddening $A_G = 2.74 \times E(B - V)$ using a line-of-sight extinction coefficient (A_G) in the G -band calculated by [Casagrande & Vandenberg \(2018\)](#) and [Zhong et al. \(2019\)](#), we were able to obtain A_G values of 2.55 & 1.93 and $E(G_{BP} - G_{RP})$ of 1.197 ± 0.08 & 0.908 ± 0.05 for NGC 7031 and NGC 7086, respectively.

The distance moduli ($m - M$) for NGC 7031 and NGC 7086 are 9.229 ± 0.037 and 9.869 ± 0.001 mag, respectively. This indicates that the photometric distances (d_{phot} ; pc) in the same manner are approximately 701 ± 26 and 942 ± 31 , which are slightly different from those obtained by [Yontan et al. \(2019\)](#).

We calculated the mean proper motion on both sides ($\mu_{\alpha}^*, \mu_{\delta}$) in the following with adopted members using the stellar space distribution as illustrated in the upper and lower panels of Figure 5, and the results yielded the following numerical values ($-3.03, -2.53$; NGC 7031) and ($-3.09, -3.26$; NGC 7086) in mas yr^{-1} units. On the other hand, their Gaussian distributions are displayed in the left and right panels of Figure 6 with numerical values (0.571; NGC 7031) and (0.622; NGC 7086) in millarcsec units. Then the reflected astrometric distances (d_{plx} ; pc) are 1752 ± 42 and 1608 ± 40 , which are consistent with those obtained by [Hunt & Reffert \(2024\)](#), [Yontan et al. \(2019\)](#), and [Cantat-Gaudin et al. \(2018\)](#). All our astrophysical parameters devoted to both clusters are represented in Table 4 as compared by different authors.

We deduce that the distances to the Galactic center R_{gc} should be included based on our estimated d_{phot} distances, which are defined as

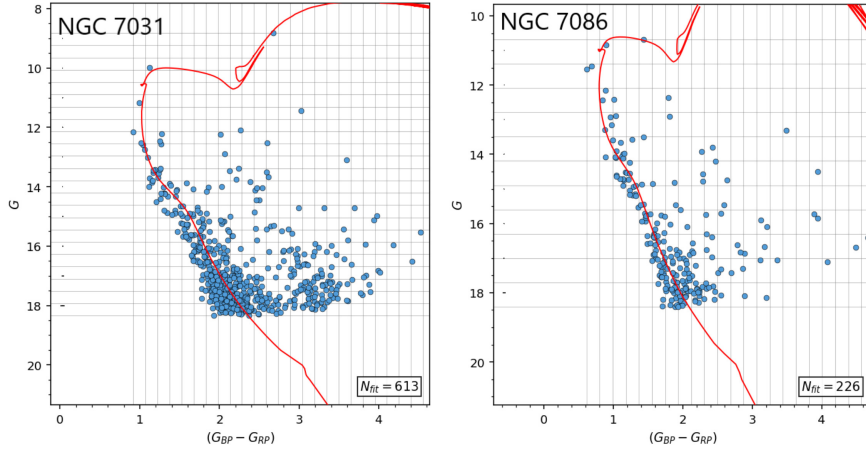


Figure 4. The CMDs of NGC 7031 (left) and NGC 7086 (right). The fitted extinction was corrected by [Bressan et al. \(2012\)](#).

$$R_{gc} = \sqrt{R_o^2 + (d \cos b)^2 - 2 R_o d \cos b \cos l} \quad (5)$$

where $R_o = 8.20 \pm 0.10$ kpc ([Bland-Hawthorn et al., 2019](#)). The following relationships can be used to calculate the projected distances toward the Galactic plane (X_\odot , Y_\odot) and the distance away from the Galactic plane (Z_\odot). The findings are shown in Table 4.

$$X_\odot = d \cos b \cos l, \quad Y_\odot = d \cos b \sin l, \quad Z_\odot = d \sin b. \quad (6)$$

5. Luminosity and mass functions

Each cluster's members are formed under similar physical conditions (same morphology) from the same molecular cloud at the same time. Therefore, the OC luminosity function (LF), which may be viewed as a projection of its CMD on the magnitude axis, indicates the distribution of member stars according to different absolute magnitude intervals.

Based on our previously mentioned NGC 7031 and NGC 7086 worksheet row data from DR3 [Gaia Collaboration \(2022\)](#) we have updated central positions, and astrophysical and photometric parameters, on this context, we have computed LF of both clusters as seen in the upper panel of Figure 7, where the

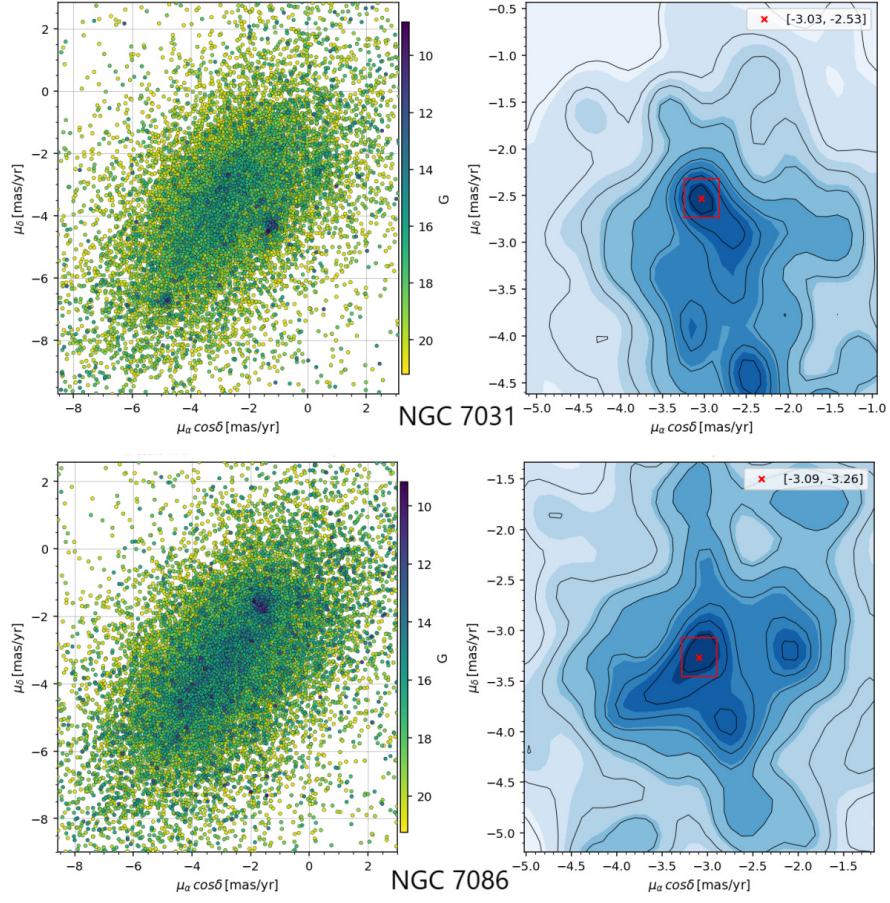


Figure 5. Mean proper motion distribution and their contours for NGC 7031 (top) and NGC 7086 (bottom).

estimated average values of absolute magnitudes ($\overline{M_G}$; mag) of each cluster are 7.51 ± 0.36 & 6.54 ± 0.39 for NGC 7031 & NGC 7086, respectively.

Empirically, the well-established mass-luminosity relation (MLR) links LF and mass function (MF) together. Additionally, absolute magnitudes (M_G ; mag) and collective masses (M_C ; M_\odot) attributed to adopted isochrones on CMDs for estimated ages, distance modulus, and reddening are taken into account. These findings were reported by [Evans et al. \(2018\)](#).

The initial mass function (IMF), which is defined as an initial arrangement of the star's masses, can be studied with great benefit from OCs mass spectrum, which contains both very low and very high mass stars ([Scalo \(1998\)](#); [Phelps &](#)

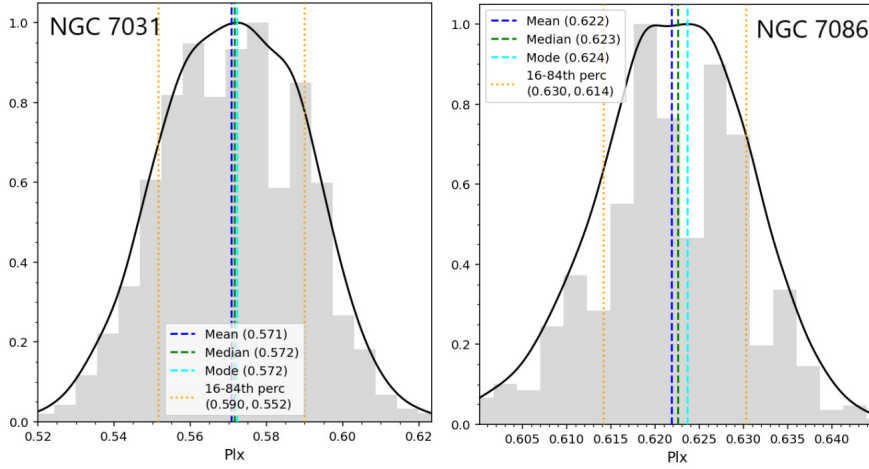


Figure 6. Parallax Gaussian distribution fitting diagrams for NGC 7031 (left) and NGC 7086 (right).

Janes (1993); Durgapal & Pandey (2001); Piatti et al. (2002); Piskunov et al. (2004); Sung & Bessell (2004); Yadav & Sagar (2002); Yadav & Sagar (2004); Bisht et al. (2017); Bisht et al. (2019)). The IMF, or present-day mass function theoretically, was defined by Salpeter (1955) as the total number (dN) the density of stars spread along a logarithmic mass scale in a mass bin (dM) with the central mass (M),

$$\text{Log} \left(\frac{dN}{dM} \right) = -\alpha \text{Log}(M) + \text{constant}, \quad (7)$$

where α is a dimensionless quantity that describes the slope of the straight line representing the MF-like lower panel of Figure 7, and it is dedicated as a characteristic of dynamical evolution for massive stars ($> 1M_{\odot}$). Salpeter's power law states that as mass increases, there are fewer stars in each mass range. Our calculated slopes from least-square fitting the MF data are 2.73 ± 0.25 & 2.67 ± 0.32 for NGC 7031 and NGC 7086, respectively, and agree with Salpeter (1955) results.

Our study indicates that the stars with the following (M_G ; mag) ranges are included in the MFs calculations: $(-0.405 \geq (M_G) \geq 9.116$ & $1.333 \geq (M_C) \geq 6.057$; NGC 7031) and $(0.806 \geq (M_G) \geq 8.545$ & $1.915 \geq (M_C) \geq 5.038$; NGC 7086). The average mass ($\overline{M_C}$), total mass (M_C), and slopes (α) are provided in Table 5.

Table 4. Our obtained astrophysical and photometric parameters of NGC 7031 and NGC 7086 as compared with those of (1) [Hunt & Reffert \(2024\)](#), (2) [Yontan et al. \(2019\)](#) and (3) [Cantat-Gaudin et al. \(2018\)](#).

Parameters	NGC 7031	NGC 7086	References
N	613	226	Current work
	264	963	(1)
	208	543	(2)
	171	622	(3)
$(\overline{\mu}_\alpha^*; \text{mas yr}^{-1})$	-3.03	-3.09	Current work
	-1.242 ± 0.122	-1.656 ± 0.148	(3)
$(\overline{\mu}_\delta; \text{mas yr}^{-1})$	-2.53	-3.26	Current work
	-4.205 ± 0.130	-1.629 ± 0.143	(3)
$(d_{plx}; \text{pc})$	1752 ± 42	1608 ± 40	Current work
	1402	1667	(1)
	1365^{+164}_{-216}	1616^{+225}_{-312}	(3)
$(d_{phot}; \text{pc})$	701 ± 26	942 ± 31	Current work
Z	0.01189 ± 0.00023	0.01121 ± 0.00025	Current work
$\log(\text{age yr}^{-1})$	8.468 ± 0.007	8.617 ± 0.021	Current work
A_G	2.55	1.93	Current work
$E(B - V)_{mag}$	0.929 ± 0.006	0.704 ± 0.001	Current work
$E(G_{BP} - G_{RP})_{mag}$	1.197 ± 0.08	0.908 ± 0.05	Current work
	1.254	1.277	(1)
$(m - M)_{mag}$	9.229 ± 0.006	9.869 ± 0.001	Current work
$(X_\odot; \text{kpc})$	-0.050 ± 0.007	-0.135 ± 0.012	Current work
	-0.033	-0.128	(1)
$(Y_\odot; \text{kpc})$	1.750 ± 0.042	1.602 ± 0.040	Current work
	1.401	1.662	(1)
$(Z_\odot; \text{kpc})$	0.071 ± 0.008	-0.008 ± 0.009	Current work
	0.056	0.006	(1)
$(R_{gc}; \text{kpc})$	8.432 ± 0.092	8.487 ± 0.093	Current work

6. Evolving times and escape velocity

The interactions between stars in OCs result in energy exchange ([Inagaki & Saslaw \(1985\)](#); [Baumgardt & Makino \(2003\)](#)). The spatial distribution of OCs is less dense than that of globular clusters. In the event of a force of contraction and/or destruction, massive stars exhibit mass segregation towards the cluster core, compared to fainter stars. Numerous OCs have recently been observed to exhibit this phenomenon ([Piatti \(2016\)](#); [Zeidler et al. \(2017\)](#); [Dib & Basu \(2018\)](#); [Rangwal et al. \(2019\)](#); [Bisht et al. \(2020\)](#); [Joshi et al. \(2020\)](#)). Following a Maxwellian stability equilibrium (i.e., dynamical evolution), the cluster's kinetic energy (velocity distribution) approaches one ([Yadav et al. \(2013\)](#); [Bisht et al. \(2019\)](#)) within dynamical relaxation time (T_{relax} ; Myr) which is the characteristic time required for dynamical evolution to be completed. T_{relax} depends

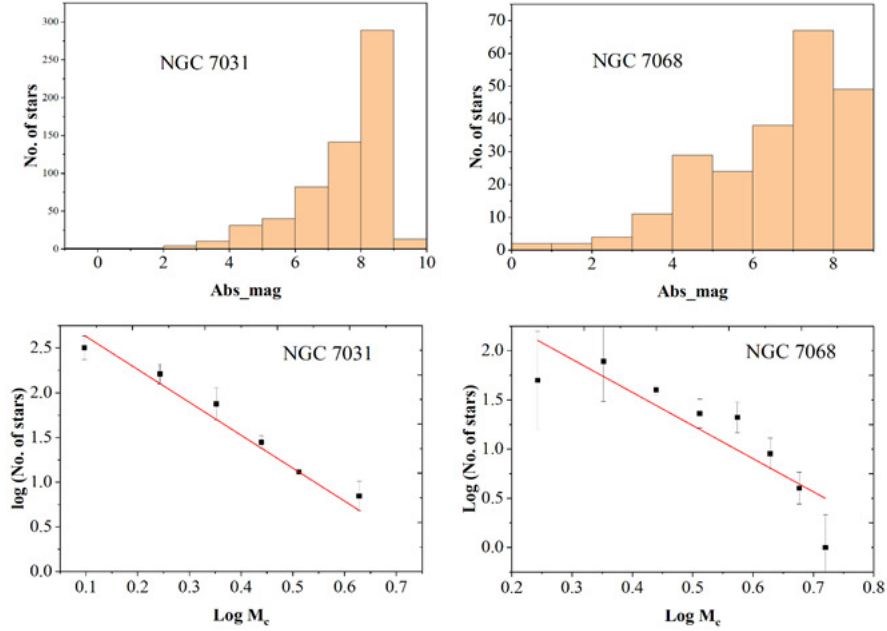


Figure 7. The true LFs for NGC 7031 and NGC 7086 are shown in the top panel. These LFs were constructed by taking the cluster’s $(m - M)$ into consideration while converting the observed G magnitudes of its member stars into absolute magnitudes M_G . The lower panel displays MFs that were obtained using the most likely members; Salpeter’s power-law fitting is indicated by solid lines in this panel.

on both cluster diameter and the number N of member stars (Lada & Lada, 2003), and according to Spitzer & Hart (1971) is given by

$$T_{relax} = \frac{8.9 \times 10^5 N^{1/2} R_h^{3/2}}{\sqrt{M_C} \log(0.4 N)}, \quad (8)$$

where R_h , which can be determined using the transformation outlined by Šablevičiūtė et al. (2006), is the radius (in pc) containing about 50% of the cluster mass,

$$R_h = 0.547 \times r_c \times \left(\frac{r_t}{r_c}\right)^{0.486}, \quad (9)$$

where the tidal and core radii are denoted, respectively, by r_c and r_t . Therefore, the derived (R_h ; pc) values are 3.07 ± 0.57 and 0.97 ± 0.01 . In the same manner the (T_{relax} ; Myr) are 1.515 and 0.267 for both NGC 7031 and NGC 7086, respectively. In addition to the relaxation time, we focus on estimating the evaporation time ($\tau_{ev} \approx 10^2 T_{relax}$; Myr), which is how long it takes to

Table 5. Our estimated average absolute magnitudes, average mass, total mass, and the IMF slopes for NGC 7031 and NGC 7086 as expressed with recent literature (1) [Hunt & Reffert \(2024\)](#).

Parameters	NGC 7031	NGC 7086	References
$(\overline{M_G}; mag)$	7.51 ± 0.36	6.54 ± 0.39	Current work
$(M_C; M_\odot)$	1072 ± 33	598 ± 25	Current work
	1403 ± 124	4271 ± 300	(1)
$(\overline{M_G}; M_\odot)$	1.75	2.64	Current work
α	2.73 ± 0.25	2.67 ± 0.32	Current work

Table 6. Table 6: Our dynamical evolution times and escape velocity for NGC 7031 and NGC 7086.

Parameters	NGC 7031	NGC 7086
T_{relax} (Myr)	1.515	0.276
τ_{ev} (Myr)	151.50	27.60
τ	194	1550
V_{esc} (km s ⁻¹)	251 ± 16	447 ± 21

evacuate every member star from internal stellar encounters ([Adams & Myers, 2001](#)). By calculating the dynamical evolution parameter (i.e., $\tau = age/T_{relax}$), we may characterize and specify the dynamic state of clusters. We concluded that our $\tau \gg 1$ for every cluster, therefore, these clusters are considered to be dynamically relaxed OCs.

Low-mass stars continue to set off the cluster, primarily at slow speeds via Lagrange points [Küpper et al. \(2008\)](#). The escape velocity (V_{esc} ; km s⁻¹) of rapid gas removal from the cluster when it remains bound in the face is ($V_{esc} = R_{gc} \sqrt{2 G M_C / 3r_t^3}$) ([Fich & Tremaine \(1991\)](#); [Fukushige & Heggie \(2000\)](#)), where the gravitational constant is $G = 4.3 \times 10^{-6}$ kpc M_\odot^{-1} (km s⁻¹)². In light of these achieved dynamical parameters, different times, and escaping velocities are shown in Table 6.

7. Ellipsoidal motion and the kinematical structure

To evaluate the coherent and uniform movements within a confined spatial region of gravitationally bound stellar assemblies in the Galactic framework, we applied a computational methodology formulated by [Elsanhoury et al. \(2018\)](#) and [Bisht et al. \(2020\)](#). This approach was utilized to determine the velocity ellipsoid parameters (VEPs) and the overall kinematics of the clusters. The

analysis focused on cluster members identified by their celestial coordinates (α_i , δ_i) with their proper motion ($\mu_{\alpha_i}^*$, μ_{δ_i}), distance (d_i), and radial velocity (V_r) with specific velocities (Hunt & Reffert, 2024) being $12.05 \pm 7.69 \text{ km s}^{-1}$ (NGC 7031) and $-16.10 \pm 3.16 \text{ km s}^{-1}$ (NGC 7086). Furthermore, we investigated their spatial velocity components (V_x , V_y , V_z ; km s^{-1}) along the x , y , and z axes of a solar-centric coordinate system.

The determination of space velocity components in Galactic coordinates (U, V, W ; km s^{-1}) employs the transformation equations outlined by Liu et al. (2011) and their distribution is shown in Figure 8.

$$U = -0.0518807421V_x - 0.8722226427V_y - 0.4863497200V_z, \quad (10)$$

$$V = +0.4846922369V_x - 0.4477920852V_y + 0.7513692061V_z, \quad (11)$$

$$W = -0.8731447899V_x - 0.1967483417V_y + 0.4459913295V_z. \quad (12)$$

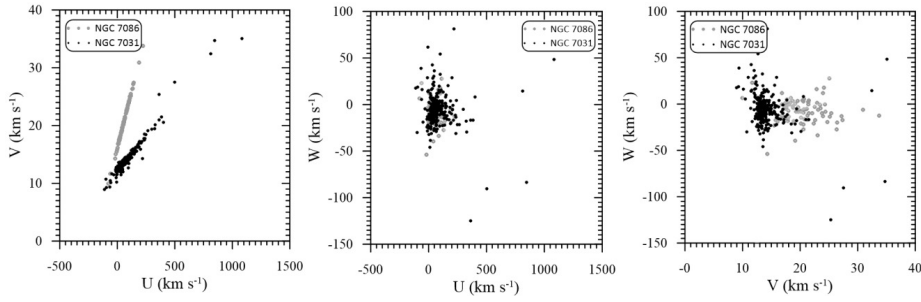


Figure 8. The distribution of the spatial velocity components for the member stars of NGC 7031 (black dots) and NGC 7086 (gray dots) in the Galactic coordinates.

Additionally, the apex coordinates of the cluster are ascertained through the apex diagram (AD) method, as illustrated in Figure 9, employing formulae for constructing the AD diagram as described by Chupina et al. (2001) and Chupina et al. (2006):

$$A_o = \tan^{-1} \left(\frac{\bar{V}_y}{\bar{V}_x} \right), \quad (13)$$

and

$$D_o = \tan^{-1} \left(\frac{\bar{V}_z}{\sqrt{\bar{V}_x^2 + \bar{V}_y^2}} \right). \quad (14)$$

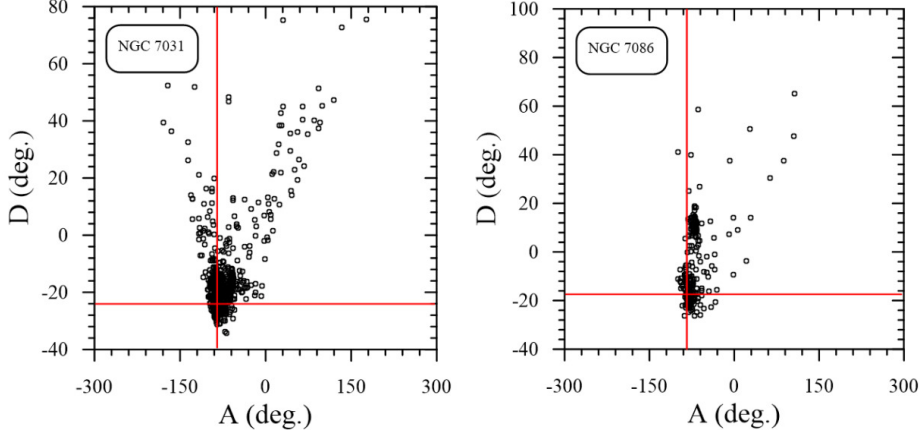


Figure 9. The AD diagram for NGC 7031 (left panel) and NGC 7086 (right panel) with a cross mark denoting the location of their convergent point (A_o , D_o).

The AD diagram facilitates an analysis of the cluster’s kinematic structure and the identification of its internal kinematic substructures. This diagram, created from the individual apexes of stars, showcases the distribution of stars within the equatorial coordinate system, where the apex equatorial coordinates (in degrees) are labeled A_o (right ascension) and D_o (declination). These coordinates result from solving a geometrical problem involving the intersection points of stars’ spatial velocity vectors with the celestial sphere.

Concerning other kinematic parameters, the cluster center (x_c , y_c , z_c ; kpc) is derived by calculating the mass center of N stars using equatorial coordinates (α_i , δ_i) and distance d_i . The solar motion elements, indicating the Sun’s velocity relative to the star group being studied, are defined as

$$U_{\odot} = -\bar{U}, \quad V_{\odot} = -\bar{V}, \quad \text{and} \quad W_{\odot} = -\bar{W}$$

Additionally, this study pioneers in estimating the solar apex location (l_A , b_A) in Galactic coordinates and their corresponding equatorial coordinates (α_A , δ_A) for both NGC 7031 and NGC 7086 OCs. We obtained the numerical kinematical results and the solar motion elements arranged in Table 7. The angular separation angle between NGC 7031 and NGC 7086 is about $3^{\circ}.81$ (i.e., 55.08 ± 7.42 pc) as depicted in Figure 10.

8. Conclusion

In the current study, we used Gaia DR3 to determine the photometric and astrometric properties of the star clusters NGC 7031 and NGC 7086. With

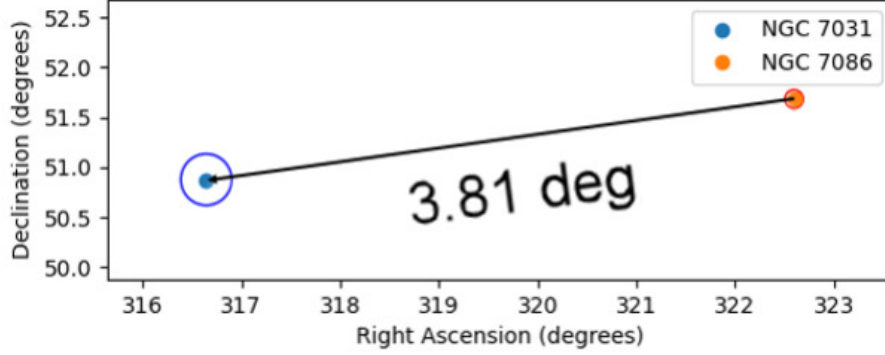


Figure 10. The angular separation between NGC 7031 and NGC 7086.

Table 7. Our obtained results of VEPs for NGC 7031 and NGC 7086 with their solar motion elements.

Parameters	NGC 7031	NGC 7086
\bar{V}_x (km s ⁻¹)	9.51 ± 0.32	12.78 ± 0.28
\bar{V}_y (km s ⁻¹)	-90.27 ± 9.50	-77.96 ± 8.83
\bar{V}_z (km s ⁻¹)	-40.46 ± 6.36	-24.93 ± 4.99
A_o	$-83^\circ.99 \pm 0^\circ.11$	$-80^\circ.69 \pm 0^\circ.11$
D_o	$-24^\circ.02 \pm 0^\circ.20$	$-17^\circ.51 \pm 0^\circ.24$
\bar{U} (km s ⁻¹)	97.91 ± 9.90	79.46 ± 8.91
\bar{V} (km s ⁻¹)	14.63 ± 3.83	22.37 ± 4.73
\bar{W} (km s ⁻¹)	-8.58 ± 0.34	-6.94 ± 0.38
x_c (kpc)	2.276 ± 0.048	1.860 ± 0.043
y_c (kpc)	-2.148 ± 0.046	-1.423 ± 0.038
z_c (kpc)	3.850 ± 0.062	2.963 ± 0.054
S_\odot (km s ⁻¹)	99.37 ± 9.97	82.84 ± 9.10
$(l_A, b_A)^\circ$	-8.50, 4.95	-15.73, 4.80
$(\alpha_A, \delta_A)^\circ$	-83.99, 24.02	-80.70, 17.52

membership probabilities $P \geq 50\%$, we assessed the most probable member stars to be 613 and 226 for respective clusters. We derived all the parameters using these Gaia-based likely members. Our results are in good agreement with the estimated parameters found in several of the most recent prior investigations. Under or overestimated numerical values in Tables 3 and 4 depending on the number of possible candidates, method of estimation and the data used. The following summarizes the main findings of the current studies:

- The distances from the cluster centers where the density of the cluster merged with the background density are named the clusters' limiting radius r_{cl} .

Our estimates are 10.04 and 3.91 arcminutes for NGC 7031 and NGC 7086, respectively.

- We created the proper motion and parallax histograms of these Gaia-based probable members by utilizing the most likely members of the two clusters that were found using the Gaia DR3 mean proper motion data. The results we computed are as follows:

- ★ $(\overline{\mu_\alpha^*}, \overline{\mu_\delta})_{\text{NGC7031}}$ is about $(-3.03, -2.53; \text{mas yr}^{-1})$, $\text{Plx}_{\text{NGC 7031}}$ is equal to 0.571 mas, and the corresponding distance d_{plx} (NGC 7031) = 1752 ± 42 pc.

- ★ $(\overline{\mu_\alpha^*}, \overline{\mu_\delta})_{\text{NGC7086}}$ is about $(-3.09, -3.26; \text{mas yr}^{-1})$, $\text{Plx}_{\text{NGC 7086}}$ is equal to 0.622 mas, and the corresponding distance d_{plx} (NGC 7086) = 1608 ± 40 pc.

- The ages (in a log scale) of NGC 7031 and NGC 7086 were determined to be 8.468 ± 0.007 and 8.617 ± 0.021 , by fitting their CMDs with the theoretical isochrones of [Bressan et al. \(2012\)](#) using Gaia DR3. According to Gaia photometry, their isochrone-based distances are 701 ± 26 and 942 ± 31 pc for respective clusters. The distances of both clusters from the galactic plane, Z_\odot , as well as their projected distances from the Sun, X_\odot , and Y_\odot , and the galactic centers R_{gc} , were then calculated and are all shown in Table 4.

- Total masses (in solar units) are 1072 ± 33 and 598 ± 25 for respective clusters. As compared with [Hunt & Reffert \(2024\)](#) for total mass ($M_C; M_\odot$) for both clusters, we found a slight difference in NGC 7031 due to our estimation and [Hunt & Reffert \(2024\)](#), on the other hand, a large difference in NGC 7086 which we recall for the number of candidates (i.e., 226; current work & 963; [Hunt & Reffert \(2024\)](#)). The initial mass function (IMF) slope was determined, i.e. $\alpha_{\text{NGC7031}} = 2.73 \pm 0.25$ and $\alpha_{\text{NGC7086}} = 2.67 \pm 0.32$, and they were found to be reasonably consistent with the value reported by Salpeter in 1955.

- We deduced that NGC 7031 and NGC 7086 are dynamically relaxed clusters with notable mass segregation based on the computation of their relaxation time.

- We presented the first complete estimation of the space velocities and kinematic parameters of both clusters, therefore, the convergent points $(-83^\circ.99 \pm 0^\circ.11, -24^\circ.02 \pm 0^\circ.20)$ and $(-80^\circ.69 \pm 0^\circ.11, -17^\circ.51 \pm 0^\circ.24)$ with respective clusters.

- Ultimately, we estimate that the age difference between NGC 7031 and NGC 7086 is 120 Myr, the linear separation between the two clusters is about 55.08 ± 7.42 pc and the distance difference along the line of sight is 228 pc. Since these findings do not meet the requirements for a binary cluster, we conclude that the two clusters are not genuine binary clusters and are most likely not produced from the same Giant Molecular Cloud (GMC).

Acknowledgements. We thank the anonymous referee for their comments that improved the quality of this paper, as well as Dr. Emily Hunt (Zentrum für Astronomie Universität Heidelberg) for her supporting data before archiving at the CDS completes. This work presents results from the European Space Agency (ESA) space mission Gaia. Gaia data are being processed by the Gaia Data Processing and Analysis Consortium

(DPAC). Funding for the DPAC is provided by national institutions, in particular, the institutions participating in the Gaia Multi-Lateral Agreement (MLA). The Gaia mission website is <https://www.cosmos.esa.int/gaia>. The Gaia archive website is <https://archives.esac.esa.int/gaia>. The authors extend their appreciation to the Deanship of Scientific Research at Northern Border University, Arar, KSA for funding this research work through the project number NBU-FFR-2024-237-03”

Data availability: We have used the different data sets for the analysis of NGC 7031 and NGC 7086, which are publicly available at the following links:

- https://vizier.cds.unistra.fr/viz-bin/VizieR-3?-source=I/355/gaiadr3&-out.max=50&-out.form=HTML%20Table&-out.add=_r&-out.add=_RAJ,_DEJ&-sort=_r&-oc.form=sexa
- https://vizier.cds.unistra.fr/viz-bin/VizieR-3?-source=J/A%2bA/673/A114&-out.max=50&-out.form=HTML%20Table&-out.add=_Glon,_Glat&-out.add=_RAJ,_DEJ&-oc.form=dec
- https://archive.stsci.edu/cgi-bin/dss_form
- <http://stev.oapd.inaf.it/cgi-bin/cmd>
- Emily L. Hunt, Private communication, 2024.

References

- Adams, F. C. & Myers, P. C., Modes of Multiple Star Formation. 2001, *Astrophysical Journal*, **553**, 744, DOI: 10.1086/320941
- Allende Prieto, C., Majewski, S. R., Schiavon, R., et al., APOGEE: The Apache Point Observatory Galactic Evolution Experiment. 2008, *Astronomische Nachrichten*, **329**, 1018, DOI: 10.1002/asna.200811080
- Angelo, M. S., Santos, J. F. C., Maia, F. F. S., & Corradi, W. J. B., Investigating Galactic binary cluster candidates with Gaia EDR3. 2022, *Monthly Notices of the RAS*, **510**, 5695, DOI: 10.1093/mnras/stab3807
- Balaguer-Núñez, L., Tian, K. P., & Zhao, J. L., Determination of proper motions and membership of the open clusters NGC 1817 and NGC 1807. 1998, *Astronomy and Astrophysics, Supplement*, **133**, 387, DOI: 10.1051/aas:1998324
- Baumgardt, H. & Makino, J., Dynamical evolution of star clusters in tidal fields. 2003, *Monthly Notices of the RAS*, **340**, 227, DOI: 10.1046/j.1365-8711.2003.06286.x
- Bhatia, R. K. & Hatzidimitriou, D., Binary star clusters in the Large Magellanic Cloud. 1988, *Monthly Notices of the RAS*, **230**, 215, DOI: 10.1093/mnras/230.2215
- Binney, J. & Tremaine, S. 2008, *Galactic Dynamics: Second Edition*
- Bisht, D., Elsanhoury, W. H., Zhu, Q., et al., An Investigation of Poorly Studied Open Cluster NGC 4337 Using Multicolor Photometric and Gaia DR2 Astrometric Data. 2020, *Astronomical Journal*, **160**, 119, DOI: 10.3847/1538-3881/ab9ffd
- Bisht, D., Yadav, R. K. S., & Durgapal, A. K., 2MASS analytical study of four open cluster candidates. 2017, *New Astronomy*, **52**, 55, DOI: 10.1016/j.newast.2016.10.009

- Bisht, D., Yadav, R. K. S., Ganesh, S., et al., Mass function and dynamical study of the open clusters Berkeley 24 and Czernik 27 using ground based imaging and Gaia astrometry. 2019, *Monthly Notices of the RAS*, **482**, 1471, DOI: 10.1093/mnras/sty2781
- Bland-Hawthorn, J., Sharma, S., Tepper-Garcia, T., et al., The GALAH survey and Gaia DR2: dissecting the stellar disc's phase space by age, action, chemistry, and location. 2019, *Monthly Notices of the RAS*, **486**, 1167, DOI: 10.1093/mnras/stz217
- Bonatto, C. & Bica, E., The nature of the young and low-mass open clusters Pismis5, vdB80, NGC1931 and BDSB96. 2009, *Monthly Notices of the RAS*, **397**, 1915, DOI: 10.1111/j.1365-2966.2009.14877.x
- Bressan, A., Marigo, P., Girardi, L., et al., PARSEC: stellar tracks and isochrones with the PAdova and TRieste Stellar Evolution Code. 2012, *Monthly Notices of the RAS*, **427**, 127, DOI: 10.1111/j.1365-2966.2012.21948.x
- Bukowiecki, L., Maciejewski, G., Konorski, P., & Strobel, A., Open Clusters in 2MASS Photometry. I. Structural and Basic Astrophysical Parameters. 2011, *Acta Astronomica*, **61**, 231, DOI: 10.48550/arXiv.1107.5119
- Cantat-Gaudin, T., Jordi, C., Vallenari, A., et al., A Gaia DR2 view of the open cluster population in the Milky Way. 2018, *Astronomy and Astrophysics*, **618**, A93, DOI: 10.1051/0004-6361/201833476
- Cardelli, J. A., Clayton, G. C., & Mathis, J. S., The Relationship between Infrared, Optical, and Ultraviolet Extinction. 1989, *Astrophysical Journal*, **345**, 245, DOI: 10.1086/167900
- Casagrande, L. & Vandenberg, D. A., On the use of Gaia magnitudes and new tables of bolometric corrections. 2018, *Monthly Notices of the RAS*, **479**, L102, DOI: 10.1093/mnras/sly104
- Chupina, N. V., Reva, V. G., & Vereshchagin, S. V., The geometry of stellar motions in the nucleus region of the Ursa Major kinematic group. 2001, *Astronomy and Astrophysics*, **371**, 115, DOI: 10.1051/0004-6361:20010337
- Chupina, N. V., Reva, V. G., & Vereshchagin, S. V., Kinematic structure of the corona of the Ursa Major flow found using proper motions and radial velocities of single stars. 2006, *Astronomy and Astrophysics*, **451**, 909, DOI: 10.1051/0004-6361:20054009
- Conrad, C., Scholz, R. D., Kharchenko, N. V., et al., A RAVE investigation on Galactic open clusters . II. Open cluster pairs, groups and complexes. 2017, *Astronomy and Astrophysics*, **600**, A106, DOI: 10.1051/0004-6361/201630012
- de La Fuente Marcos, R. & de La Fuente Marcos, C., Double or binary: on the multiplicity of open star clusters. 2009, *Astronomy and Astrophysics*, **500**, L13, DOI: 10.1051/0004-6361/200912297
- De Silva, G. M., Freeman, K. C., Bland-Hawthorn, J., et al., The GALAH survey: scientific motivation. 2015, *Monthly Notices of the RAS*, **449**, 2604, DOI: 10.1093/mnras/stv327


- Dias, W. S., Alessi, B. S., Moitinho, A., & Lépine, J. R. D., New catalogue of optically visible open clusters and candidates. 2002, *Astronomy and Astrophysics*, **389**, 871, DOI: 10.1051/0004-6361:20020668
- Dib, S. & Basu, S., The emergence of the galactic stellar mass function from a non-universal IMF in clusters. 2018, *Astronomy and Astrophysics*, **614**, A43, DOI: 10.1051/0004-6361/201732490
- Dieball, A., Müller, H., & Grebel, E. K., A statistical study of binary and multiple clusters in the LMC. 2002, *Astronomy and Astrophysics*, **391**, 547, DOI: 10.1051/0004-6361:20020815
- Durgapal, A. K. & Pandey, A. K., Structure and mass function of five intermediate/old open clusters. 2001, *Astronomy and Astrophysics*, **375**, 840, DOI: 10.1051/0004-6361:20010892
- Elsanhoury, W. H., Postnikova, E. S., Chupina, N. V., et al., The Pleiades apex and its kinematical structure. 2018, *Astrophysics and Space Science*, **363**, 58, DOI: 10.1007/s10509-018-3268-3
- Evans, D. W., Riello, M., De Angeli, F., et al., Gaia Data Release 2. Photometric content and validation. 2018, *Astronomy and Astrophysics*, **616**, A4, DOI: 10.1051/0004-6361/201832756
- Fich, M. & Tremaine, S., The mass of the Galaxy. 1991, *Annual Review of Astron and Astrophys*, **29**, 409, DOI: 10.1146/annurev.aa.29.090191.002205
- Fukushige, T. & Heggie, D. C., The time-scale of escape from star clusters. 2000, *Monthly Notices of the RAS*, **318**, 753, DOI: 10.1046/j.1365-8711.2000.03811.x
- Gaia Collaboration. 2022, VizieR Online Data Catalog: Gaia DR3 Part 1. Main source (Gaia Collaboration, 2022), VizieR On-line Data Catalog: I/355. Originally published in: *Astron. Astrophys.*, in prep. (2022)
- Gaia Collaboration, Brown, A. G. A., Vallenari, A., et al., Gaia Early Data Release 3. Summary of the contents and survey properties. 2021, *Astronomy and Astrophysics*, **649**, A1, DOI: 10.1051/0004-6361/202039657
- Gilmore, G., Randich, S., Asplund, M., et al., The Gaia-ESO Public Spectroscopic Survey. 2012, *The Messenger*, **147**, 25
- Hassan, S. M., Three-Color Photometry of NGC 7086. 1967, *Zeitschrift fuer Astrophysik*, **66**, 6
- Hassan, S. M. & Barbon, R., A photometric study of the open cluster NGC 7031. 1973, *Mem. Societa Astronomica Italiana*, **44**, 39
- Hatzidimitriou, D. & Bhatia, R. K., Cluster pairs in the Small Magellanic Cloud. 1990, *Astronomy and Astrophysics*, **230**, 11
- Hoag, A. A., Johnson, H. L., Iriarte, B., et al., Photometry of stars in galactic cluster fields. 1961, *Publications of the U.S. Naval Observatory Second Series*, **17**, 344
- Hunt, E. L. & Reffert, S., Improving the open cluster census. II. An all-sky cluster catalogue with Gaia DR3. 2023, *Astronomy and Astrophysics*, **673**, A114, DOI: 10.1051/0004-6361/202346285

- Hunt, E. L. & Reffert, S., Improving the open cluster census. III. Using cluster masses, radii, and dynamics to create a cleaned open cluster catalogue. 2024, *arXiv e-prints*, arXiv:2403.05143, DOI: 10.48550/arXiv.2403.05143
- Inagaki, S. & Saslaw, W. C., Equipartition in multicomponent gravitational systems. 1985, *Astrophysical Journal*, **292**, 339, DOI: 10.1086/163164
- Javakhishvili, G., Kukhianidze, V., Todua, M., & Inasaridze, R., A method of open cluster membership determination. 2006, *Astronomy and Astrophysics*, **447**, 915, DOI: 10.1051/0004-6361:20040297
- Jeffries, R. D., Thurston, M. R., & Hambly, N. C., Photometry and membership for low mass stars in the young open cluster NGC 2516. 2001, *Astronomy and Astrophysics*, **375**, 863, DOI: 10.1051/0004-6361:20010918
- Joshi, Y. C., Dambis, A. K., Pandey, A. K., & Joshi, S., Study of open clusters within 1.8 kpc and understanding the Galactic structure. 2016, *Astronomy and Astrophysics*, **593**, A116, DOI: 10.1051/0004-6361/201628944
- Joshi, Y. C., Maurya, J., John, A. A., et al., Photometric, kinematic, and variability study in the young open cluster NGC 1960. 2020, *Monthly Notices of the RAS*, **492**, 3602, DOI: 10.1093/mnras/staa029
- Kharchenko, N. V., Piskunov, A. E., Schilbach, E., Röser, S., & Scholz, R. D., Global survey of star clusters in the Milky Way. II. The catalogue of basic parameters. 2013, *Astronomy and Astrophysics*, **558**, A53, DOI: 10.1051/0004-6361/201322302
- King, I., The structure of star clusters. I. an empirical density law. 1962, *Astronomical Journal*, **67**, 471, DOI: 10.1086/108756
- King, I. R., The structure of star clusters. III. Some simple dynamical models. 1966, *Astronomical Journal*, **71**, 64, DOI: 10.1086/109857
- Kopchev, V. S. & Petrov, G. T., BV photometry of a possible open star cluster pair NGC 7031/NGC 7086. 2008, *Astronomische Nachrichten*, **329**, 845, DOI: 10.1002/asna.200711009
- Krone-Martins, A. & Moitinho, A., UPMASK: unsupervised photometric membership assignment in stellar clusters. 2014, *Astronomy and Astrophysics*, **561**, A57, DOI: 10.1051/0004-6361/201321143
- Küpper, A. H. W., MacLeod, A., & Heggie, D. C., On the structure of tidal tails. 2008, *Monthly Notices of the RAS*, **387**, 1248, DOI: 10.1111/j.1365-2966.2008.13323.x
- Lada, C. J. & Lada, E. A., Embedded Clusters in Molecular Clouds. 2003, *Annual Review of Astron and Astrophys*, **41**, 57, DOI: 10.1146/annurev.astro.41.011802.094844
- Lindoff, U., The ages of open clusters. 1968, *Arkiv for Astronomi*, **5**, 1
- Liu, J. C., Zhu, Z., & Hu, B., Constructing a Galactic coordinate system based on near-infrared and radio catalogs. 2011, *Astronomy and Astrophysics*, **536**, A102, DOI: 10.1051/0004-6361/201116947
- Netopil, M., Paunzen, E., & Stütz, C., Developments of the Open Cluster Database WEBDA. 2012, in *Astrophysics and Space Science Proceedings*, Vol. **29**, *Star Clusters in the Era of Large Surveys*, 53

- Perren, G. I., Giorgi, E. E., Moitinho, A., et al., Sixteen overlooked open clusters in the fourth Galactic quadrant. A combined analysis of UBVI photometry and Gaia DR2 with ASteCA. 2020, *Astronomy and Astrophysics*, **637**, A95, DOI: 10.1051/0004-6361/201937141
- Perren, G. I., Vázquez, R. A., & Piatti, A. E., ASteCA: Automated Stellar Cluster Analysis. 2015, *Astronomy and Astrophysics*, **576**, A6, DOI: 10.1051/0004-6361/201424946
- PHELPS, R. L. & JANES, K. A., Young Open Clusters as Probes of the Star-Formation Process. II. Mass and Luminosity Functions of Young Open Clusters. 1993, *Astronomical Journal*, **106**, 1870, DOI: 10.1086/116772
- Piatti, A. E., A comprehensive photometric study of dynamically evolved small van den Bergh-Hagen open clusters. 2016, *Monthly Notices of the RAS*, **463**, 3476, DOI: 10.1093/mnras/stw2248
- Piatti, A. E., Bica, E., Santos, J. F. C., J., & Clariá, J. J., A revision of the fundamental parameters of the open cluster Hogg 15 and the projected star WR 47. 2002, *Astronomy and Astrophysics*, **387**, 108, DOI: 10.1051/0004-6361:20020373
- Pietrzynski, G. & Udalski, A., The Optical Gravitational Lensing Experiment. Multiple Cluster Candidates in the Large Magellanic Cloud. 2000, *Acta Astronomica*, **50**, 355, DOI: 10.48550/arXiv.astro-ph/0010294
- Piskunov, A. E., Belikov, A. N., Kharchenko, N. V., Sagar, R., & Subramaniam, A., On the determination of age and mass functions of stars in young open star clusters from the analysis of their luminosity functions. 2004, *Monthly Notices of the RAS*, **349**, 1449, DOI: 10.1111/j.1365-2966.2004.07620.x
- Rangwal, G., Yadav, R. K. S., Durgapal, A., Bisht, D., & Nardiello, D., Astrometric and photometric study of NGC 6067, NGC 2506, and IC 4651 open clusters based on wide-field ground and Gaia DR2 data. 2019, *Monthly Notices of the RAS*, **490**, 1383, DOI: 10.1093/mnras/stz2642
- Rosvick, J. M. & Robb, R., A Photometric Search for Planets in the Open Cluster NGC 7086. 2006, *Astronomical Journal*, **132**, 2309, DOI: 10.1086/508517
- Salpeter, E. E., The Luminosity Function and Stellar Evolution. 1955, *Astrophysical Journal*, **121**, 161, DOI: 10.1086/145971
- Santos-Silva, T. & Gregorio-Hetem, J., Characterisation of young stellar clusters. 2012, *Astronomy and Astrophysics*, **547**, A107, DOI: 10.1051/0004-6361/201219695
- Scalo, J., The IMF Revisited: A Case for Variations. 1998, in *Astronomical Society of the Pacific Conference Series*, Vol. **142**, *The Stellar Initial Mass Function (38th Herstmonceux Conference)*, ed. G. Gilmore & D. Howell, 201
- Scott, D. W. 1992, *Multivariate Density Estimation*
- Spitzer, Lyman, J. & Hart, M. H., Random Gravitational Encounters and the Evolution of Spherical Systems. I. Method. 1971, *Astrophysical Journal*, **164**, 399, DOI: 10.1086/150855
- Subramaniam, A., Gorti, U., Sagar, R., & Bhatt, H. C., Probable binary open star clusters in the Galaxy. 1995, *Astronomy and Astrophysics*, **302**, 86

- Sung, H. & Bessell, M. S., The Initial Mass Function and Stellar Content of NGC 3603. 2004, *Astronomical Journal*, **127**, 1014, DOI: 10.1086/381297
- Svolopoulos, S. N., Spectral Classification in Some Open Clusters. 1961, *Astrophysical Journal*, **134**, 612, DOI: 10.1086/147183
- von Hoerner, S., Internal structure of globular clusters. 1957, *Astrophysical Journal*, **125**, 451, DOI: 10.1086/146321
- Šablevičiūtė, I., Vansevicius, V., Kodaira, K., et al., A Survey of Compact Star Clusters in the South-West Field of the M 31 Disk. Structural Parameters. 2006, *Baltic Astronomy*, **15**, 547, DOI: 10.48550/arXiv.astro-ph/0701774
- Yadav, R. K. S. & Sagar, R., A deep UBVR CCD photometric study of the open clusters Tr1 and Be 11. 2002, *Monthly Notices of the RAS*, **337**, 133, DOI: 10.1046/j.1365-8711.2002.05888.x
- Yadav, R. K. S. & Sagar, R., UBVR CCD photometric study of the open clusters Basel 4 and NGC 7067. 2004, *Monthly Notices of the RAS*, **349**, 1481, DOI: 10.1111/j.1365-2966.2004.07623.x
- Yadav, R. K. S., Sariya, D. P., & Sagar, R., Proper motions and membership probabilities of stars in the region of open cluster NGC 3766. 2013, *Monthly Notices of the RAS*, **430**, 3350, DOI: 10.1093/mnras/stt136
- Yontan, T., Bilir, S., Bostancı, Z. F., et al., CCD UBVR photometric and Gaia astrometric study of eight open clusters—ASCC 115, Collinder 421, NGC 6793, NGC 7031, NGC 7039, NGC 7086, Roslund 1 and Stock 21. 2019, *Astrophysics and Space Science*, **364**, 152, DOI: 10.1007/s10509-019-3640-y
- Zeidler, P., Nota, A., Grebel, E. K., et al., A High-resolution Multiband Survey of Westerlund 2 with the Hubble Space Telescope. III. The Present-day Stellar Mass Function. 2017, *Astronomical Journal*, **153**, 122, DOI: 10.3847/1538-3881/153/3/122
- Zhong, J., Chen, L., Kouwenhoven, M. B. N., et al., Substructure and halo population of Double Cluster h and χ Persei. 2019, *Astronomy and Astrophysics*, **624**, A34, DOI: 10.1051/0004-6361/201834334

Outward oriented gravitational attraction in the innermost part of the compact objects - a new feature of relativistic gravity

L. Neslušan 

*Astronomical Institute of the Slovak Academy of Sciences
059 60 Tatranská Lomnica, The Slovak Republic (E-mail: ne@ta3.sk)*

Received: June 27, 2024; Accepted: July 15, 2024

Abstract. We point out a new feature of gravity within general relativity (GR): according to GR, the gravity in the innermost region of relativistic compact objects (RCOs) is oriented outward from the object's center. We explain how the normal, attractive, gravity does result in such the orientation. Our analysis of RCO properties, derived from some models which imply the outward oriented action in the RCO central region, indicates that the gaseous RCOs are the objects in the shape of a hollow sphere with an inner physical surface. These inner radii can be arbitrarily small (but it is questionable if ever exactly zero), and this has been, likely, the reason of why the phenomenon of the outward oriented gravity has escaped our attention. We discuss the conceptual differences between the old, fulfilled-sphere, and new, hollow-sphere, concepts of RCO. Until now, the new concept has been forbidden by a postulate, in fact. This prohibition caused that almost whole general relativity was forbidden in the astrophysics of RCOs; the Oppenheimer-Volkoff upper-mass limit is a consequence of this prohibition. In conclusion, we point out that any model of realistic RCOs in the shape of a rigorous fulfilled sphere has never been constructed. It is questionable if such a solution of field equation exists. Within GR, we can easily construct only the models of real stable RCOs in the form of a hollow-sphere.

Key words: gravitation – general relativity – neutron stars – supermassive compact objects

1. Introduction

In this article, we give a review of gradually improving knowledge about the relativistic compact object (RCO), which should acquire the shape of a hollow-sphere, i.e. the spherical volume constrained not only with an outer, but also an inner physical surface. A large part of this knowledge was published in our previous papers (Neslušan, 2015, 2017a,b, 2019; Neslušan, 2022) and papers by deLyra et al. (deLyra, 2021; deLyra & Carneiro, 2023; deLyra et al., 2023; deLyra, 2023). Anastopoulos & Savvidou (2021) and Kotopoulis & Anastopoulos

(2023) analyzed a thermodynamic consistency of the equation of state, whereby they also dealt with the hollow-sphere solutions. One should, however, be careful with the conclusions drawn in their work since they also considered some unrealistic equations of state and outward oriented gravitational action represented with the help of negative mass. Even before the publishing of all these papers, the first hollow-sphere model of RCO was published by Ni (2011). Our review is completed with some new arguments and explanations.

The new concept of RCO raises a lot of questions. For example, if the RCO in the shape of a hollow sphere is stable; if the metrics inside it and in its vicinity is continuous; why a vacuum void in its central region occurs; what is the mechanism of its formation, etc. Of course, the main question is: how is the hollow-sphere RCO concept related to the currently accepted concept of the RCO in the form of a fulfilled sphere? What are the arguments in favor of each of these two concepts?

A discussion about the new concept is important. The general relativity (GR) provides us with a set of solutions to construct a model of RCO. The extent of this set can be illustrated with an infinite area. In the scheme in Fig. 1, this area is shown with the blue color. The area is bordered, from one side, with an abscissa (drawn with the red color in the scheme). The extent of the solutions implying the RCOs in the form of a fulfilled sphere is proportional only to this abscissa. (At the moment, it is however unknown whether the RCO can acquire the form of an exact or only approximate fulfilled sphere; we discuss this problem in Sect. 4.2.) The area of the one-dimensional abscissa is zero. The scheme in Fig. 1 points out that we are currently allowed to use the zero-area part of the infinite-area set of solutions. Either we should have a very good reason to reject almost all available solutions or we should abolish the prohibition of using them.

2. Outline of the theory of RCO

2.1. Description of the curvature of space-time

At first, let us outline the theory of RCO in general. In the following, we consider a simple, static, spherically symmetric object. Using the $---+$ signature and the coordinate system with the spatial part to be the spherical system $O(r\vartheta\varphi)$, the line element in the case of spherical symmetry is

$$ds^2 = -e^\lambda dr^2 - r^2 d\vartheta^2 - r^2 \sin^2 \vartheta d\varphi^2 + e^\nu c^2 dt^2, \quad (1)$$

where $-e^\lambda = g_{11} = g_{rr}$, $-r^2 = g_{22} = g_{\vartheta\vartheta}$, $-r^2 \sin^2 \vartheta = g_{33} = g_{\varphi\varphi}$, and $e^\nu = g_{44} = g_{tt}$. In the static RCO, the auxiliary metric functions λ and ν are the functions of only the radial distance, r .

Since we consider a compact object within GR, gravity must be described by Einstein's field equations (EFEs) (Einstein, 1915, 1916). For the spherically

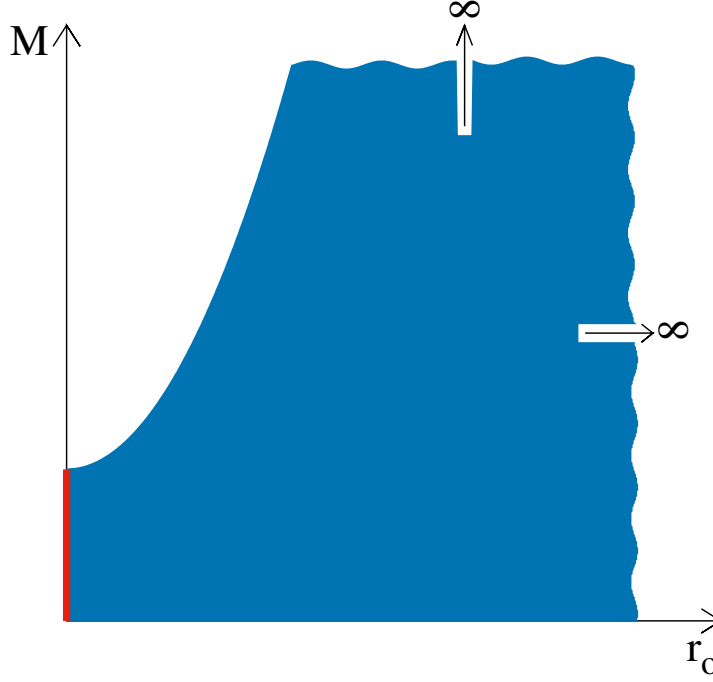


Figure 1. The scheme illustrating the whole extent of all GR solutions to describe the RCOs (the blue area continuing to infinity upward and rightward) and extent of the part of solutions which are currently allowed to be used (the red vertical abscissa).

symmetric RCO, these equations acquire the form (Tolman, 1934)

$$\kappa T_1^1 = -e^{-\lambda} \left(\frac{\nu'}{r} + \frac{1}{r^2} \right) + \frac{1}{r^2}, \quad (2)$$

$$\kappa T_2^2 = -e^{-\lambda} \left(\frac{\nu''}{2} - \frac{\lambda' \nu'}{4} + \frac{\nu'^2}{4} + \frac{\nu' - \lambda'}{2r} \right), \quad (3)$$

$$\kappa T_3^3 = -e^{-\lambda} \left(\frac{\nu''}{2} - \frac{\lambda' \nu'}{4} + \frac{\nu'^2}{4} + \frac{\nu' - \lambda'}{2r} \right), \quad (4)$$

$$\kappa T_4^4 = e^{-\lambda} \left(\frac{\lambda'}{r} - \frac{1}{r^2} \right) + \frac{1}{r^2}, \quad (5)$$

$$\kappa T_\mu^\sigma = 0 \quad \text{for } \mu \neq \sigma, \quad (6)$$

where $\kappa = 8\pi G/c^4$ is the Einstein gravitational constant (G is the Newton gravitational constant and c is the speed of light in vacuum) and T_μ^σ is the stress-energy tensor. The prime indicates the derivative of a given quantity in respect

of r and the double prime the second derivative in respect of r . When one deals with the spherically symmetric neutron stars as well as other gaseous spherically symmetric RCOs, the stress-energy tensor for a perfect fluid (Tolman, 1934)

$$T_{\mu}^{\sigma} = \begin{pmatrix} -P & 0 & 0 & 0 \\ 0 & -P & 0 & 0 \\ 0 & 0 & -P & 0 \\ 0 & 0 & 0 & E \end{pmatrix} \quad (7)$$

is relevant, where P is the pressure and E is the energy density.

Four EFEs (2)–(5) contain four quantities, λ , ν , P , and E , which are the functions of variable r in the considered static case. However, when the components of tensor (7) are supplied into EFEs (2)–(5), then EFE (3) is identical with EFE (4). It means that we have only three equations, in fact, but these still contain four unknown quantities. We need to supply one more equation to solve the system. Usually, this additional equation is an equation of state (EoS) relating P and E . In Sect. 4.6, we however mention other kind of equations which can be assumed and added to complete the system.

Oppenheimer & Volkoff (1939) replaced the auxiliary function λ by other metric function they denoted u . This function was defined by

$$u = \frac{1}{2}r \left(1 + \frac{1}{g_{rr}} \right) = \frac{1}{2}r (1 - e^{-\lambda}). \quad (8)$$

In this context, we see that u is another parameter characterizing the space-time. With the help of all, Eq.(8), matrix (7), and after an algebraic handling, EFEs (2) and (5) can be re-written to the form

$$\nu' = \frac{2}{r^2 - 2ru} \left(\frac{1}{2}\kappa Pr^3 + u \right), \quad (9)$$

$$u' = \frac{1}{2}\kappa Er^2. \quad (10)$$

Using the last three equations and Eq.(3) or identical Eq.(4) after $T_2^2 = T_3^3 = -P$ is supplied, we can also express the derivative of pressure in respect to r , specifically

$$P' = -\frac{E + P}{r^2 - 2ru} \left(\frac{1}{2}\kappa Pr^3 + u \right) \quad (11)$$

or, taking into account relation (9),

$$P' = -\frac{E + P}{2}\nu'. \quad (12)$$

2.2. Equation of state - examples

In view of our explanation, we consider an example in which the additional equation is the EoS of the cold, degenerated, Fermi-Dirac, neutron gas (Chandrasekhar, 1935), which was also used by Oppenheimer & Volkoff (1939) in their pioneering work. The EoS can be derived from the integrals known within the quantum statistics for the number density, n_n , pressure, P , and energy density, E . These integrals can be found in the textbooks (e.g. Hansen & Kawaler, 1994). In course to calculate them, the authors used an auxiliary quantity, τ , which is the function of the Fermi impulse, p_f , and is defined as

$$\tau = 4 \ln \left[\frac{p_f}{m_n c} + \sqrt{1 + \left(\frac{p_f}{m_n c} \right)^2} \right], \quad (13)$$

where m_n is the mass of a neutron. With the help of τ , the pressure and energy density can be given as

$$P = \frac{m_n^4 c^5}{96\pi^2 \hbar^3} \left(\sinh \tau - 8 \sinh \frac{\tau}{2} + 3\tau \right), \quad (14)$$

$$E = \frac{m_n^4 c^5}{32\pi^2 \hbar^3} (\sinh \tau - \tau). \quad (15)$$

\hbar is the Planck constant divided by 2π . In the EFEs, P and E are, thus, replaced with the single quantity τ and it is useful to replace Eq.(11), giving the derivative of pressure in respect to r , with the equation (Oppenheimer & Volkoff, 1939)

$$\tau' = -4 \frac{\sinh \tau - 2 \sinh \frac{\tau}{2}}{r^2 - 2ru} \cdot \frac{\frac{m_n^4 c G}{24\pi \hbar^3} r^3 \left(\sinh \tau - 8 \sinh \frac{\tau}{2} + 3\tau \right) + u}{\cosh \tau - 4 \cosh \frac{\tau}{2} + 3}, \quad (16)$$

which gives the derivative of τ in respect to r . Eq.(16) was derived from Eq.(11) realizing that $dP/dr = (dP/d\tau)(d\tau/dr)$ and $dP/d\tau$ was calculated deriving (14) in respect to τ .

If the derivatives in respect to r in Eq.(12) are replaced with the differentiation in respect to τ and relations (14) and (15) are used, we obtain the equation

$$\begin{aligned} & \left(\cosh \tau - 4 \cosh \frac{\tau}{2} + 3 \right) d\tau = \\ & = -\frac{1}{2} \left(4 \sinh \tau - 8 \sinh \frac{\tau}{2} \right) d\nu, \end{aligned} \quad (17)$$

which can be analytically integrated. The integration yields a useful relation between the g_{tt} component of metric tensor and τ ,

$$e^\nu = \frac{C_\nu}{\cosh \frac{\tau}{2} + 1}, \quad (18)$$

where C_ν is an integration constant.

Besides the EoS expressed with the help of relations (14) and (15), we also consider the EoS in the form of a polytrope, EoS of radiation, or a combination of both. The polytrope can be given with the help of relations (Tooper, 1965)

$$P = K_P \rho^{1+1/N}, \quad (19)$$

$$E = NP + c^2 \rho, \quad (20)$$

where K_P is a constant of proportionality, ρ is the material density, and N is the polytrope index. The EoS of radiation is

$$E = 3P \quad (21)$$

and the EoS, which is the combination of a polytrope and radiation can be given as

$$P = K_P \rho^{1+1/N} + \frac{1}{3} a T^4 \quad (22)$$

and with E given by relation (20), again (but this time, P is given by relation (22), not by (19)). In Eq.(22), a is the radiation constant and T is the temperature related to material density, in the given context, as

$$T = T_{max} \left(\frac{\rho}{\rho_{max}} \right)^{1/N}. \quad (23)$$

T_{max} and ρ_{max} are the constants, which equal to the maximum temperature and maximum density, respectively.

3. Acceleration of a test particle in rest, in GR

3.1. Acceleration in the field of a point-like massive particle

In course toward understanding of an RCO configuration in the form of a hollow sphere, we remind (Neslušan, 2019) and analyze the formula giving the gravitational acceleration of a test particle (TP) in the vicinity of a point-like material object. The TP is in rest in respect to the object. To calculate its acceleration within GR, the equation of geodesic,

$$\frac{d^2 x^\alpha}{ds^2} = -\Gamma_{\beta\gamma}^\alpha \frac{dx^\beta}{ds} \frac{dx^\gamma}{ds}, \quad (24)$$

should be used. x^α ($\alpha = 1, 2, 3, 4$) are the four-coordinates and $\Gamma_{\beta\gamma}^\alpha$ are the Christoffel symbols. Using relation $dx^\alpha/ds = (dx^\alpha/dt)(dt/ds)$ (see, e.g., Straumann, 2013, p. 59), equation (24) can be re-written as

$$\frac{d^2 x^\alpha}{dt^2} = \left(\Gamma_{\beta\gamma}^\alpha \frac{dx^\beta}{dt} \frac{dx^\gamma}{dt} - \Gamma_{\beta\gamma}^\alpha \right) \frac{dx^\beta}{dt} \frac{dx^\gamma}{dt}. \quad (25)$$

In the considered spherical coordinate frame centered on the material object, the TP accelerates in the negative sense of the radial axis. The radial component of the acceleration is

$$\begin{aligned}
\frac{d^2r}{dt^2} &= (-\Gamma_{11}^1 + \Gamma_{14}^4 + \Gamma_{41}^4) \left(\frac{dr}{dt}\right)^2 - \Gamma_{22}^1 \left(\frac{d\vartheta}{dt}\right)^2 - \\
&\quad - \Gamma_{33}^1 \left(\frac{d\varphi}{dt}\right)^2 - c^2 \Gamma_{44}^1 = \\
&= \left(-\frac{1}{2} \frac{d\lambda}{dr} + \frac{d\nu}{dr}\right) \left(\frac{dr}{dt}\right)^2 + r e^{-\lambda} \left(\frac{d\vartheta}{dt}\right)^2 + \\
&\quad + r \sin^2 \vartheta e^{-\lambda} \left(\frac{d\varphi}{dt}\right)^2 - \frac{c^2}{2} e^{\nu-\lambda} \frac{d\nu}{dr}, \tag{26}
\end{aligned}$$

For the TP being in rest, i.e. with $dr/dt = d\vartheta/dt = d\varphi/dt = 0$, the last formula reduces to

$$\frac{d^2r}{dt^2} = -c^2 \Gamma_{44}^1 = -\frac{c^2}{2} e^{\nu-\lambda} \frac{d\nu}{dr}. \tag{27}$$

Assuming that the object and the TP are in vacuum, the metrics in the vicinity of the object must be, according to the Birkhoff theorem (Birkhoff & Langer, 1923), the outer Schwarzschild metrics (OSM) (Schwarzschild, 1916). We know that this metrics was found as the solution of the EFEs in the case of spherical symmetry. Hence, only the diagonal components of the metric tensor are non-zero. We remind that we denoted them (in Sect. 2.1) as $g_{11} = g_{rr}$, $g_{22} = g_{\vartheta\vartheta}$, $g_{33} = g_{\varphi\varphi}$, and $g_{44} = g_{tt}$. In the OSM, components $g_{\vartheta\vartheta}$ and $g_{\varphi\varphi}$ are the same as in the flat space-time; specifically, $g_{\vartheta\vartheta} = -r^2$ and $g_{\varphi\varphi} = -r^2 \sin^2 \vartheta$. Components g_{rr} and g_{tt} equal

$$g_{tt} = -\frac{K_\nu}{g_{rr}} = e^\nu = -K_\nu e^{-\lambda} = K_\nu \left(1 - \frac{2u_c}{r}\right), \tag{28}$$

where K_ν and u_c are the integration constants (Equation (3) is the differential equation of the second order, therefore its solution must contain two integration constants). In the application like in our case, there is a convention to choose $K_\nu = 1$. If e^ν and $e^{-\lambda}$, expressed by Eq.(28), are supplied into Eq.(27), then the acceleration of the TP is

$$\ddot{r} = -\left(1 - \frac{2u_c}{r}\right) \frac{c^2 u_c}{r^2} = -\frac{c^2 u_c}{r^2} + \frac{2c^2 u_c^2}{r^3}, \tag{29}$$

whereby the minus (plus) sign at the right-hand side indicates its orientation in the direction toward (outward from) the origin of coordinate frame. The double dot above r denotes the second time derivative of the radial distance, r .

3.2. Calibration of constant u_c

In a weak gravitational field, the Newton physics well describes the reality and, thus, the relations derived within GR should converge, in the limit of weak field, to the corresponding relations in the Newtonian physics. In the weak field, $2u_c/r \ll 1$ and can be neglected. Then, the acceleration (29) reduces to

$$\ddot{r} = -\frac{c^2 u_c}{r^2}, \quad (30)$$

which is identical to the acceleration calculated by using the Newton gravitational law,

$$\ddot{r} = -\frac{Gm}{r^2}, \quad (31)$$

when the constant u_c equals

$$u_c = \frac{Gm}{c^2}. \quad (32)$$

In the last relations, m is the mass of a massive object in the Newtonian physics. It is worth stressing that this physics and GR are two conceptually different theories. Hence, the concept of mass in the former is completely different than the mass in the latter. In the former, the mass is not related to energy. We discuss the meaning of quantity u more in Sect. 5.2.

We note that constant u_c is, in fact, function u (see Sect. 2.1 and relation (8)) in the vacuum. Namely, we have $E = 0$ in the vacuum and, according to relation (10), $u' = 0$, then. After the integration of this differential equation, we obtain $u = u_c$.

We see that the relativistic acceleration given by relation (29) consists of two terms. The first term, $-c^2 u_c/r^2$, is identical, in fact, to the acceleration in the Newtonian physics and we will refer to it as to the “Newtonian term”. The second term, $+2c^2 u_c^2/r^3$, occurs in the GR formula for the acceleration. It is the “relativistic term”. Interestingly, the sign of the relativistic term is opposite to that of the Newtonian term. Hence, the relativistic term is a repulsive contribution to the Newtonian gravitational attraction. Since the inequality $2u_c/r < 1$ is always valid above the event horizon, the total gravitational acceleration must be attractive.

However, when we calculate the acceleration according to (i) the Newtonian formula (31) and (ii) relativistic formula (29) for the same system of particles and in the same configuration, then the absolute value of the first acceleration is greater than that of the second. In other words, the Newtonian gravity is stronger than the relativistic gravity above the event horizon.

If the whole massive object were located below its event horizon and also the TP were below this horizon, then, interestingly, its acceleration would be oriented away from the object; by formula (29), the gravitational action is implied to be repulsive below the horizon. No part of the RCO presented in this work is, however, located there.

3.3. Acceleration inside the spherically symmetric shell

This paper introduces the models of RCO in the form of a hollow sphere, with the inner physical surface and vacuum void inside. The example of such a model is given in Sect. 4. It may seem to be a paradox that the gravity, with its attractive character, shapes a spherically symmetric object to such a form. In this sub-section, we clarify the mechanism leading to an occurrence of the outward oriented acceleration in the deep RCO interior due to the gravitational attraction.

Because of simplicity of our explanation, we consider a thin, spherically symmetric material shell. It is well-known that the acceleration due to the net gravity of the shell is zero in the classical, Newtonian physics (this fact is also shown below). In GR, it is postulated that the metrics in the shell's interior must be the Minkowski metrics, which also implies the zero acceleration. However, this postulate is in a disagreement with the relativistic formula for the acceleration derived on the basis of the equation of geodesic. Thus, it is also in a disagreement with the EFEs.

Since we want to discuss the relevance of the old and new concepts of the RCO, we ignore the postulating the Minkowski metrics and use the above-found formula for the acceleration to derive the net acceleration in a spherical shell, in this sub-section. If the equation of geodesic is taken into account, then one can notice an important consequence of the relativistic term in the formula giving the acceleration on a TP inside the shell.

So, let us consider a thin, spherically symmetric, material shell. The density of matter in the shell is constant and equal to ρ . Let the gravity due to the matter in the shell be weak, therefore we can proceed, in our derivation, as in within the Newtonian physics. To describe the acceleration of TP, we further consider the rectangular coordinate frame $O(xyz)$ with the origin identical with the position of the TP (Fig. 2). The center of the shell is situated on the negative part of the coordinate z -axis and its distance from the TP is smaller than the radius of the shell.

As seen in Fig. 2, the coordinate x - y plane intersects the shell dividing it to the upper and lower globular canopies (the cross-curve of this plane with the shell is shown with the ellipse in Fig. 2; the center of the ellipse is identical to the position of the particle). Firstly, we calculate the partial acceleration of the TP due to the gravity of the matter in an infinitesimally small volume of the shell, dV_1 , in the upper canopy. The volume is seen from the position of the particle under space angle $d\Omega = \sin\vartheta d\vartheta d\varphi$ and the mass inside this volume is $\mu_1 = \rho r_1^2 d\Omega dr$. Symbol r_1 stands for the distance between the volume and the TP.

It is worth characterizing the position of the TP also in the rectangular frame $O(\tilde{x}_1\tilde{y}_1\tilde{z}_1)$ with the origin identical with the position of volume dV_1 and the axes \tilde{x}_1 , \tilde{y}_1 , and \tilde{z}_1 parallel with x , y , and z , respectively (Fig. 2). In this frame, the

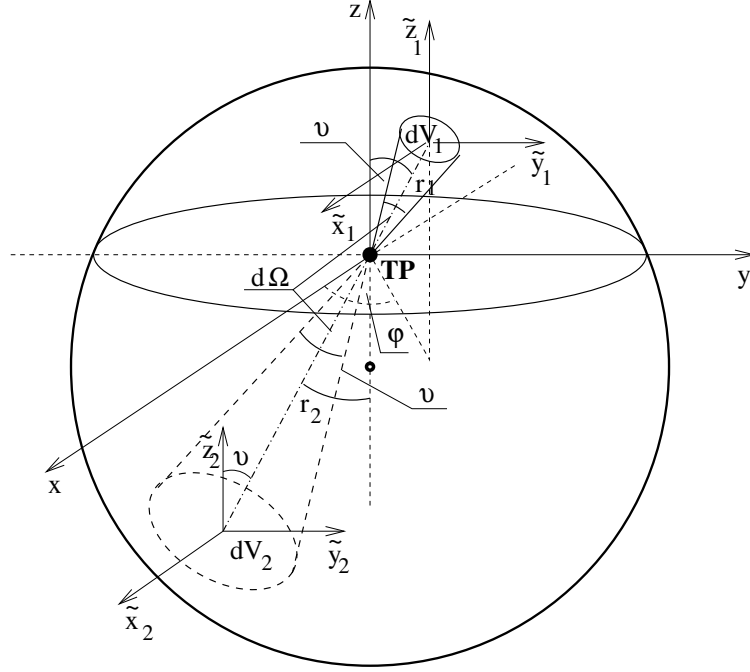


Figure 2. The scheme illustrating the position of a test particle (TP) inside a thin material shell (the large circle) and positions of two considered small partial volumes of the sphere, dV_1 and dV_2 (small ellipses). In Sect. 3.3, this scheme is used to explain the acceleration of the TP due to the matter of each of these volumes. In the explanation, three coordinate frames, $O(xyz)$, $O(\tilde{x}_1\tilde{y}_1\tilde{z}_1)$, and $O(\tilde{x}_2\tilde{y}_2\tilde{z}_2)$, are considered. From the position of the particle, volume dV_1 is seen under the same space angle, $d\Omega$, as volume dV_2 . The particle is located in the origin of the frame $O(xyz)$. The origins of frames $O(\tilde{x}_1\tilde{y}_1\tilde{z}_1)$ and $O(\tilde{x}_2\tilde{y}_2\tilde{z}_2)$ are identical with the positions of volumes dV_1 and dV_2 , respectively, and their axes are parallel with the corresponding axes of $O(xyz)$ frame. The whole shell is divided by the coordinate x - y plane (the cross-curve of both the plane and the shell is the ellipse with the horizontal axis passing through the TP), into upper and lower globular canopies. Volume dV_1 is situated in the upper and dV_2 in the lower canopy.

position of the TP can be characterized with the radial distance $\tilde{r}_1 = r_1$ and angles $\tilde{\vartheta}_1 = \pi + \vartheta$, $\tilde{\varphi}_1 = \varphi$.

Let us ignore, for a while, the remaining part of the shell and consider only the TP and the matter in the volume. The infinitesimally small volume can be regarded as a point and the metrics in its vicinity is the OSM. It means that the parameter u_c can be given with the help of mass μ_1 as $u_1 = G\mu_1/c^2$. We describe the OSM metrics and corresponding acceleration of the TP in the

rectangular coordinate frame $O(\tilde{x}_1\tilde{y}_1\tilde{z}_1)$. The \tilde{z}_1 -component of the acceleration of the TP due to the matter in the volume is given by

$$\ddot{\tilde{z}}_1 = - \left(1 - \frac{2G\mu_1}{r_1} \right) \frac{G\mu_1}{\tilde{r}_1^2} \frac{\tilde{z}_1}{\tilde{r}_1} \quad (33)$$

(see, e.g., our earlier paper (Neslušan, 2023), where we derived the x -component of the acceleration; the formulas for the other components are analogous; these can be obtained by the cyclic interchange of spatial variables, $x \rightarrow y \rightarrow z \rightarrow x$).

Obviously, $\tilde{z}_1/\tilde{r}_1 = \cos \vartheta_1$ and since $\vartheta_1 = \pi - \vartheta$, we can write $\tilde{z}_1/\tilde{r}_1 = \tilde{z}_1/r_1 = -\cos \vartheta$ (Fig. 2). Because the z -coordinate is related to \tilde{z}_1 as $z = \tilde{z}_1 + r_1 \cos \vartheta$, then z -components of corresponding accelerations are related as $\ddot{z} = \ddot{\tilde{z}}_1$ (the position of volume dV_1 does not change in time, therefore r_1 and ϑ are not functions of time). Using these relations and $\mu_1 = \rho r_1^2 \sin \vartheta d\vartheta d\varphi dr$, relation (33) can be re-written as

$$\ddot{\tilde{z}}_1 = G\rho \cos \vartheta \sin \vartheta d\vartheta d\varphi dr - \frac{2G^2\rho^2}{c^2} r_1 \cos \vartheta (\sin \vartheta d\vartheta d\varphi dr)^2, \quad (34)$$

where $\ddot{\tilde{z}}_1$ is the acceleration of the TP due to volume dV_1 referred in the $O(xyz)$ frame.

Secondly, let us consider the matter in the infinitesimal volume of the shell, dV_2 , in the exactly opposite direction than the first volume (Fig. 2). Also the second volume is seen from the position of the TP under space angle $d\Omega$. When we calculate the acceleration of the TP, the volume can be regarded as a point-like massive particle with the neighboring metrics being the OSM. Now, we describe the metrics and corresponding acceleration in the third rectangular coordinate frame $O(\tilde{x}_2\tilde{y}_2\tilde{z}_2)$ with the origin identical with the position of dV_2 and axes parallel with the axes of the $O(xyz)$ frame. In $O(\tilde{x}_2\tilde{y}_2\tilde{z}_2)$, the position of the TP is characterized by radial distance $\tilde{r}_2 = r_2$ and with angles $\vartheta_2 = \vartheta$ and $\varphi_2 = \pi + \varphi$.

The \tilde{z}_2 -component of the acceleration of the TP due to the gravity of matter in dV_2 can again be calculated by using relation (33) with the interchanges $\tilde{z}_1 \rightarrow \tilde{z}_2$, $\tilde{r}_1 \rightarrow \tilde{r}_2$, and $\mu_1 \rightarrow \mu_2$. Therefore, the mass of dV_2 equals $\mu_2 = r_2^2 d\Omega dr$ and u_c in the OSM can be expressed as $u_2 = G\mu_2/c^2$. Now $\tilde{z}_2/\tilde{r}_2 = \tilde{z}_2/r_2 = \cos \vartheta$ and the relation for the acceleration in the case of dV_2 can be given as

$$\ddot{\tilde{z}}_2 = -G\rho \cos \vartheta \sin \vartheta d\vartheta d\varphi dr + \frac{2G^2\rho^2}{c^2} r_2 \cos \vartheta (\sin \vartheta d\vartheta d\varphi dr)^2 \quad (35)$$

in the $O(xyz)$ frame (it is valid $z = \tilde{z}_2 - r_2 \cos \vartheta$ and, hence, $\ddot{z} = \ddot{\tilde{z}}_2$).

The first, Newtonian, term in (35) has the same size, but opposite sign than this term in (34), therefore the sum of the Newtonian terms in both components

of the acceleration, \ddot{z}_1 and \ddot{z}_2 , is zero. This is valid not only for the two considered infinitesimal volumes, but for every pair of volumes of which the first is located in the upper and the second one in the opposite direction in the lower globular canopy. The partial Newtonian gravity of the first volume is always eliminated by the partial Newtonian gravity of the second volume, which is seen under the same space angle. As we already mentioned, the resulting net gravity in the shell is zero in the Newtonian physics.

However, the sum of the relativistic terms is not zero. We have

$$\ddot{z}_1 + \ddot{z}_2 = \frac{2G^2\rho^2}{c^2}(r_2 - r_1) \cos\vartheta(\sin\vartheta d\vartheta d\varphi dr)^2. \quad (36)$$

Angle ϑ characterizes the position of volume dV_2 in the lower globular canopy, therefore it ranges from zero to $\pi/2$ and $\cos\vartheta > 0$. It is also valid that $r_1 < r_2$ (see Fig. 2), i.e. $r_2 - r_1 > 0$, therefore the total acceleration, due to the combined action of both volumes, is $\ddot{z}_1 + \ddot{z}_2 > 0$.

The positive value of the acceleration means that its z -component, in the $O(xyz)$ coordinate frame, is oriented in the positive direction of the coordinate z -axis. This is, again, valid for each pair of volumes, the first in the upper and the second in the lower globular canopy, which are seen from the position of the TP under the same space angle. Taking into account all possible pairs of volumes, summarily, we deduce that the net acceleration due to the gravity of matter in the upper canopy is larger than the net acceleration due to the gravity of matter in the lower canopy (Neslušan, 2019, see especially Fig. 7b). It means that the TP is accelerated away from the center of the shell. However, we would like to stress, again, that the TP is not *repelled* from the shell's center; it is attracted by the matter of the upper globular canopy with a stronger gravity, which dominates over a weaker gravity of the lower globular canopy.

It is well known that GR is not a linear theory, therefore our explanation described above is valid only for a weak field. In a strong field, the first result of our deduction, i.e. the acceleration for the system "matter in the 1-st volume"- "test particle", is no longer valid after the "matter in the 2-nd volume" is added to this system. In GR, the partial accelerations cannot be given as a simple vectorial sum as in the Newtonian physics. We presented the explanation valid, approximately, for a weak field in the sake of its transparency of the operating mechanism.

The generally correct way to calculate the acceleration in the shell is solving the EFEs as it was made in the construction of an example of a neutron star, which is presented later, in Sect. 4.1. However, the effect of the outward oriented gravitational action is not, then, very transparent. The resulting solution of the numerical integration of the EFEs is discussed more in the following section. Anyway, the explanation given in the text above indicates that the gravitational acceleration of a TP in the interior of a spherical layer of RCO matter is non-zero and oriented outward in GR.

4. Example of RCO

4.1. Modeling of RCO

A simple model of a neutron star can be created solving field equations (9), (10), and (16), in which P and E are expressed with the help of (14) and (15). Equations (9), (10), and (16) contain three quantities, ν , u , and τ , which are functions of a single variable r ; the system can be solved.

An analytical solution of these equations is unknown, therefore one can solve them via a numerical integration. The integration cannot start in the object's center, in $r = 0$, since the denominator $r^2 - 2ru \rightarrow 0$ for $r \rightarrow 0$ in the fractions in Eqs.(9) and (16). The integration must start in a finite star-centric distance.

Researchers who modeled neutron stars usually started the integration at a small star-centric distance Δr . The integration was processed outward and terminated at the outer physical surface of the star where the pressure and energy density vanished. They assumed that all quantities acquired essentially the same value in the true center of the star (at $r = 0$) as in the small starting distance Δr , since Δr could be, e.g., 1 cm. Hence, the assumption seems to be, intuitively, reasonable in the case of an object with ~ 10 to ~ 15 km radius.

It however appears that the human intuition fails in this case. If one starts the integration in a finite star-centric distance and performs it in two stages: stepping outward and inward, then the pressure and energy density vanish not only at the outer physical surface, but they, earlier or later, decrease and vanish in a non-zero star-centric distance in the inward processed integration as well. This fact implies the existence of an inner physical surface and vacuum void inside. In Sect. 4.2, we explain why the inner surface occurs in a gaseous object. In Sect. 4.6, we discuss some known solutions leading to a fulfilled-sphere RCO and explain why these solutions are irrelevant to the real gaseous RCOs.

In Fig. 3, there is the behavior of pressure in a model of a neutron star constructed by integrating Eqs.(9), (10), and (16) for the EoS given by relations (14) and (15). It is reasonable to start the integration in the distance, r_o , where the net gravity is zero (where $\nu' = 0$) and also the pressure and energy density reach their maximum (where the function representing the pressure reaches a local extreme, i.e. $P' = 0$). Seeing relations (9) and (11), $\nu' = 0$ and $P' = 0$ if $(1/2)\kappa P_{max} r_o^3 + u_o = 0$. From the latter

$$u_o = -\frac{1}{2}\kappa P_{max} r_o^3 \quad (37)$$

in the zero-gravity distance (Neslušan, 2017b). From this point, the integration should be done in two stages, stepping inward and outward. The maximum pressure, P_{max} , and the zero-gravity distance, r_o , are arbitrary input parameters. One can vary their values to obtain the model of an object with the required mass and the outer (or inner) radius.

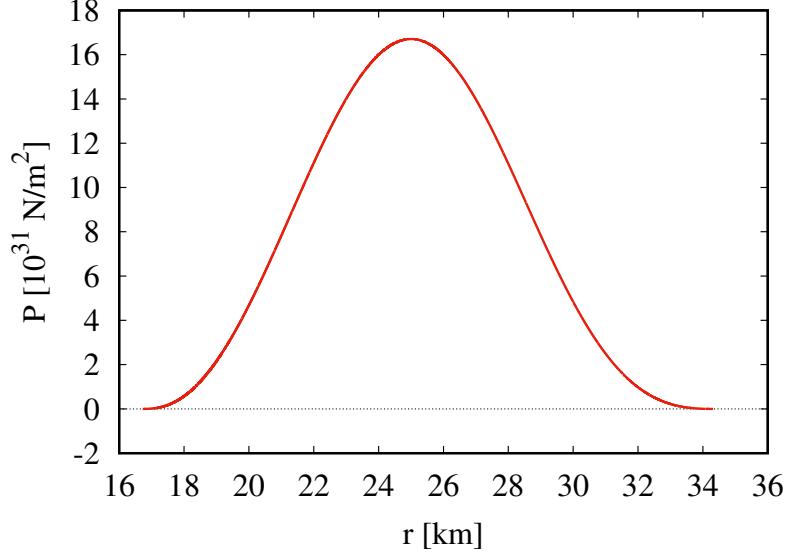


Figure 3. The dependence of the pressure, P , on the radial distance, r , from the center of the star in the example of a neutron star presented in Sect. 4. The zero-gravity distance in this object is $r_o = 25$ km. Its inner and outer radii equal 16.7 and 34.4 km, respectively.

4.2. Distribution of state quantities

When we proceed as described in the previous sub-section, we can construct a model of RCO - a neutron star. In the example with the result shown in Fig. 3, the distance of zero net gravity was chosen to be $r_o = 25$ km and the rest energy in terms of the rest mass, M_o , was achieved, doing an iteration, to be $M_o = 5 M_\odot$ (it corresponded to the Fermi impulse in r_o equal to $0.27464 m_n c$). We remind that the rest mass is given by the formula (e.g. Straumann, 2013; Misner et al., 2017, but with $R_{in} \equiv 0$, there)

$$M_o = 4\pi m_n \int_{R_{in}}^{R_{out}} n_n r^2 \sqrt{-g_{rr}} dr, \quad (38)$$

where n_n is the number density of neutrons. It can be calculated as (Oppenheimer & Volkoff, 1939)

$$n_n = \frac{1}{3\pi^2} \left(\frac{m_n c}{\hbar} \right)^3 \sinh^3 \frac{\tau}{2}. \quad (39)$$

As seen in Fig. 3, the pressure decreases outward as well as inward from r_o . The stability of the object is kept by a balance between the gravity and the

gradient of pressure. Let us analyze the net gravitational acceleration in more detail. When one divides the RCO into a large number of thin concentric layers and considers a radius r , there is a certain number, N_l , of spherical layers with radii smaller than r (“lower” layers) and a certain number, N_u , of spherical layers with radii larger than r (“upper” layers). Obviously, all the lower layers attract a TP in distance r downward, toward the RCO center, and the upper layers attract it outward as indicated in Sect. 3.3.

Let the TP be initially located at such a distance r that the net acceleration due to the lower layers is larger than that due to the upper layers, therefore the particle is accelerated inward. If we consider the particle at a smaller r than initially, the number of lower layers is smaller and the number of upper layers larger. Correspondingly, the net gravity of lower layers is reduced and that of upper layers magnified. If we further reduce r , then there must occur a critical distance, r_o , in which the absolute value of the net acceleration of lower layers just equals the absolute value of the net acceleration of upper layers. The total net gravity is, thus, zero in this distance. In distances $r < r_o$, the outward oriented net acceleration due to the upper layers must prevail; the particle accelerates outward in this region.

It seems that the region of the outward oriented gravity must exist in every gaseous RCO. Let us perform the following deduction. Imagine an RCO with both the inner radius and the zero-gravity distance approaching zero. In such an RCO, the mass within the sphere of radius r_o approaches zero when $r_o \rightarrow 0$ and, thus, the net gravity of the lower layers must also approach zero. This very low net gravity must be overcome by the net gravity of the upper layers before r_o reaches the exact zero value, because the acceleration due to this gravity approaches a finite (i.e. greater than zero) constant when $r_o \rightarrow 0$. This deduction would surely be correct in the flat space-time of Newtonian physics. However, the geometry of curved space-time is more difficult and we cannot exclude that the net gravity of the upper layers does not dominate even in the exact center of RCO.

The problem of existence or non-existence of the solution implying a realistic fulfilled-sphere RCO model could be solved with the help of an analytical solution of the EFEs for a realistic EoS. In physics, such a solution is often searched for in the form of Taylor series. Actually, we can find the coefficients of the series for P , E , and u in the vicinity of the center. However, the individual terms are so complicated that it is practically impossible to prove a convergence of the series.

In a stable RCO, the gravity is balanced by the gradient of pressure. In region $r > r_o$, the gravity acting on each concentric layer is oriented inward and the gradient of pressure, being the same size as the gravity, pushes the layer outward (notice the decrease of the pressure with the increasing radial distance in this region in Fig. 3). In region $r < r_o$, the orientation of the forces is opposite: the gravity acts outward and gradient of pressure inward (the pressure increases with the increasing radial distance, here).

4.3. Behavior of metrics

The behavior of the quantities g_{rr} , g_{tt} , and u characterizing the metrics in our example of RCO is shown in Fig. 4. In a realistic model of a neutron star or any realistic RCO, the metrics of the RCO body must be smoothly tailored to the external, vacuum metrics. (We use the term ‘‘RCO body’’ to refer to the volume inside the RCO, between the RCO-centric spheres with radii R_{in} and R_{out} .) According to the Birkhoff theorem (Birkhoff & Langer, 1923), the vacuum metrics in the vicinity of a spherically symmetric distribution of matter must be the OSM. Actually, as demonstrated in Fig. 4, only this metrics can be smoothly tailored to the metrics of the object’s body. The behavior of the RCO-body metrics is shown with the thick blue curve in each panel of the figure. The OSM in both outer (green curves) and inner (purple curves) physical surfaces actually touches the RCO-body metrics at the end points of the blue curve and the corresponding OSM curve smoothly continues behind the corresponding end point; there is no break in the merged curve. It means that the corresponding derivatives in respect to r equal each other; this was verified making a numerical calculation of the derivatives.

In Fig. 4c, notice that function $u < 0$ below the distance r_z , whereby $R_{in} < r_z < R_{out}$. The negative u occurs in the central region of the RCO body as well as in the internal vacuum void of any numerically created model of the RCO consisting of a comprehensible perfect fluid.

In the OSM, the function u is a constant. In the region $r < R_{in}$, we denote this function by u_{in} (the purple straight line in Fig. 4c) and in $r > R_{out}$ by u_{out} (the green straight line). The OSM g_{rr} component of metric tensor can be tailored to the g_{rr} of the RCO body at distances $r = R_{in}$ and $r = R_{out}$. The OSM g_{rr} equals $g_{rr} = -1/(1 - 2u_{in}/r)$ in the region $r \leq R_{in}$ (the purple curve in Fig. 4a) and $g_{rr} = -1/(1 - 2u_{out}/r)$ in the region $r \geq R_{out}$ (the green curve in Fig. 4a). Similarly, the g_{tt} component of the OSM can be tailored to g_{tt} of the RCO body at distances R_{in} and R_{out} and can be calculated as $g_{tt} = K_{\nu,i}(1 - 2u_{in}/r)$ in the region $r \leq R_{in}$ (the purple curve in Fig. 4b) and $g_{tt} = K_{\nu,o}(1 - 2u_{out}/r)$ in $r \geq R_{out}$ (the green curve).

There is a convention to put $K_{\nu,o} = 1$. Since the whole behavior of g_{tt} , from $r = 0$ to $r = \infty$, is fixed by this calibration, the constant $K_{\nu,i}$ cannot be chosen arbitrarily. It can be calculated on the basis of relation (18). At the inner and outer RCO surfaces, the pressure and energy density vanish, therefore the corresponding Fermi impulse equals zero in R_{in} and R_{out} . Then, according to (13), also $\tau = 0$ at these two distances. For $\tau = 0$, $g_{tt}(R_{in}) = C_\nu/2$ as well as $g_{tt}(R_{out}) = C_\nu/2$, therefore $g_{tt}(R_{in}) = g_{tt}(R_{out})$, according to (18). Notice that the component g_{tt} inside the RCO-body (the blue curve in Fig. 4b) begins and ends at the same value. It means that $K_{\nu,i}(1 - 2u_{in}/R_{in}) = K_{\nu,o}(1 - 2u_{out}/R_{out})$ or (Neslušan, 2015)

$$K_{\nu,i} = \frac{1 - \frac{2u_{out}}{R_{out}}}{1 - \frac{2u_{in}}{R_{in}}}, \quad (40)$$

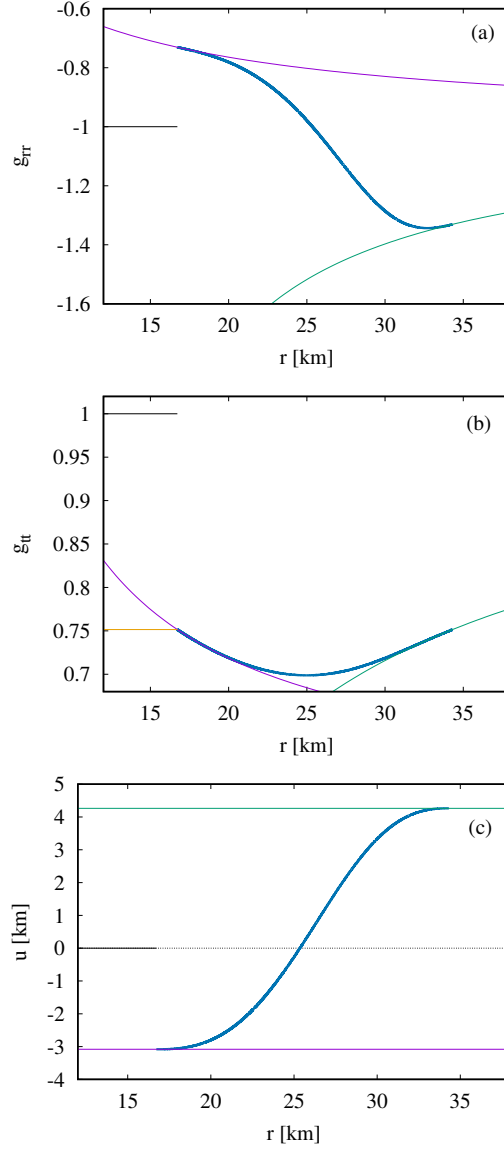


Figure 4. The dependence of g_{rr} (panel a) and g_{tt} (b) components of the metric tensor, as well as the auxiliary function u (c) on the radial distance, r , in the example of the neutron star presented in Sect. 4. The metrics in the star's body is shown with the thick blue curve. The OSM, which can be tailored to the RCO-body metrics at the outer (inner) physical surface in the right-hand end (left-hand end) of the thick blue curve, is shown with the thin green (thin purple) curve in each plot. The corresponding Minkowski metrics is shown with the black or orange straight line (see Sect. 4.4).

if we take into account the convention $K_{\nu,o} = 1$. In the example of a neutron star presented above, $K_{\nu,i} = 0.549047$.

An analogous equation to Eq.(18) can also be found for other EoSs than (14) and (15); probably for every reasonable EoS. For the polytrope (see relations (19) and (20)), in which E and P are functions of the material density, ρ , one can find

$$e^\nu = \frac{A_1}{(1 + A_2\rho^{1/3})^2}, \quad (41)$$

where A_1 is an integration constant and A_2 is a constant related to the maximum pressure and maximum material density of RCO. deLyra & Carneiro (2023) found the equation relating g_{tt} component and the energy density for other kind of a polytrope. Again, $\rho = 0$ or $E = 0$ in both R_{in} and R_{out} , therefore $g_{tt}(R_{in}) = g_{tt}(R_{out})$ also in these cases. Likely, this equality is universal.

In the vacuum far from the star, i.e. at a distance $r \gg R_{out}$, the gravitational acceleration of a TP due to the star's gravity can be well approximated with the Newtonian formula

$$\ddot{r} = -\frac{GM_{out}}{r^2}, \quad (42)$$

in which the parameter u_{out} is again calibrated with the parameter M_{out} , which can be identified with the Newtonian mass of the object, whereby $M_{out} = c^2 u_{out}/G$. We established this new notation because we use M_{out} as the parameter within GR. As seen, it corresponds to u_{out} , which characterizes the vacuum metrics in the region of $r \geq R_{out}$. (Later, we use also notation $M_{in} = c^2 u_{in}/G$ for the parameter corresponding with u_{in} , which characterizes the vacuum metrics in the region of $r \leq R_{in}$.)

Since the neutron star is the RCO with the GR gravity different from its Newtonian counterpart, acceleration (42) is not proportional to the mass M which is the equivalent of the total energy (see Sect. 5), but it is determined by the value M_{out} characterizing the metrics above the outer RCO surface. While the total mass, calculated within GR, is $M = 4.97457 M_\odot$, the Newtonian mass $M_{out} = 2.88708 M_\odot$ in our example. When the experts spoke about the measured ‘‘mass’’ of a neutron star, they spoke about the quantity M_{out} , in fact. In the case of the given example, they would say that the *mass* is $2.88708 M_\odot$ (not $4.97457 M_\odot$). Unfortunately, the Newtonian and GR concepts of mass are often used in a confusing way in this context.

The actual energy content of all known neutron stars is still unknown. We can only guess that the true M is significantly larger than the measured M_{out} .¹ In our example, we can clearly see the essential difference between GR and Newtonian physics in the case of RCOs.

¹Some models of the super-massive RCOs constructed with the EoS in the combined form of a polytrope and radiation imply that the total RCO mass as the equivalent of energy can exceed its Newtonian mass M_{out} by several orders of magnitude, so far. (Neslušan, 2022)

4.4. A note on the Minkowski metrics inside a spherical shell

In the literature, we can find a claim that the space-time inside the spherical shell is described by the Minkowski metrics, which implies zero gravitational acceleration of a TP. Our deduction made in Sects. 3.3 and 4.2 however implies that this claim has the character of a postulate. In addition, the claim is in a disagreement with the Birkhoff theorem (Birkhoff & Langer, 1923) saying that the vacuum metrics in the vicinity of any spherically symmetric distribution of matter must be the OSM (with $u_c \neq 0$; the Minkowski metrics can also be regarded as the special case of the OSM, with $u_c = 0$).

To postulate the Minkowski, flat, metrics, in the RCO vacuum void, one must neglect the second term in relation (29). It means that the acceleration implied by the equation of geodesic is replaced with the acceleration by the Newton gravitational law, in fact. In other words, the equation of geodesics is ignored, therefore GR itself is ignored. The Minkowski metrics was postulated to achieve the regularity of metrics in the RCO's center (see Sect. 7.1). But it is not a very logical way, when one, in course to achieve the regularity within GR, must ignore this theory.

In addition, the Minkowski metrics $(-1, -1, -1, 1)$ cannot be smoothly tailored with the metrics in the shell's body (Neslušan, 2017b) as is demonstrated in Fig. 4 (the black straight line in each panel). If the g_{tt} component of the Minkowski metrics equaled other constant than unity, the net gravity in the shell would also be zero. But even if we chose such a constant, which would lead to the linking of the Minkowski g_{tt} with the shell-body g_{tt} in R_{in} (this alternative Minkowski g_{tt} is drawn with orange color in Fig. 4b), the derivatives of both the orange straight line and the blue curve in R_{in} would not be equal. There would still be a discontinuity of the metrics. In conclusion, the postulate of the Minkowski metrics inside the spherical shell is physically unacceptable.

It is also unacceptable when we consider an infinitesimally thin shell. Then, the OSM relevant to the vacuum above the shell must be smoothly tailored with the Minkowski metrics in the shell's internal void. This is, however, impossible, since the derivatives dg_{rr}/dr and dg_{tt}/dr of the OSM are never zero at the shell's radius and, thus, they cannot match their Minkowski-metrics counterparts. The metrics that can be smoothly tailored to the RCO-body metrics at the inner surface of RCO is the OSM with a constant $u_c < 0$ as we demonstrated in Sect. 4.3 (see especially Fig. 4).

4.5. On the central singularity

As already mentioned, the metrics in the vacuum void below the RCO's inner surface is the OSM, but with $u_c \equiv u_{in} < 0$ (Fig. 4c). The OSM has a singular point at $r = 0$, since $g_{tt} \rightarrow \infty$ (not $-\infty$ because $u_{in} < 0$).

The inequality $u_{in} < 0$ means that a TP in the void is accelerated outward from the RCO's center as it was indicated in Sect. 3.3 and modeled in Sect. 4.3.

This acceleration increases above all limits when $r \rightarrow 0$, but, because it is oriented outward, the singularity is the Big-Bang type singularity (Neslušan, 2019). Thus, it is not in a conflict with the cosmic censorship (Penrose, 1969).

The “repulsive” character of the singularity was also stated by deLyra et al. (2023) in the conclusions of their paper. We should however be careful when we use the adjective “repulsive”. It can be used for the sake of simplicity of language to express the “repulsive” (from the RCO’s center) orientation of the force field. When we however analyze the physical nature of the force action, we must realize that the point in the exact RCO’s center is a vacuum point having no influence on a TP in its vicinity. The active agent acting on the particle is the circumambient matter of the RCO, which *attracts* it away from the center. This attraction increases above all limits when $r \rightarrow 0$ because of the geometry of space-time in the RCO’s internal vacuum void.

In reality, the mass of RCO-constituting matter is finite and a finite mass can be a source of only a finite action. Then, the singularity due to a finite action cannot be a true singularity. This claim can be supported by the following thought experiment (Neslušan, 2019). We shoot a particle situated in the internal RCO cavity toward the RCO center (singularity). If the kinetic energy of the particle is so small that its influence on the metrics in the cavity is negligible in comparison to that of the matter constituting the RCO, then the particle is decelerated, approaches the center up to a certain finite distance, where it is stopped, and then accelerated back by the gravity of the RCO matter.

On the contrary, if the energy of the particle is so high that the influence of this energy dominates over that of the RCO matter, then the metrics inside the vacuum void is re-configured. The presence of this high energy must have an impact on the neighboring space-time. After the re-configuration, the central singularity simply disappears. In such a case, the particle can pass through the point at $r = 0$, but this point is no longer a singular point. The experiment implies that the central singularity is only an abstract singularity, which figures in our mathematical description of the void metrics, but the singular point (until it remains singular) can never be visited by any material object and, hence, detected by any observer.

4.6. Remarks on the fulfilled-sphere solutions

In the context of the hollow-sphere concept of RCO, it is necessary to mention some known solutions of the EFEs, which resulted in the objects without the inner radius (e.g. Tolman, 1939; Buchdahl, 1967; Whittaker, 1968).

In Sect. 2, we showed that EFEs (3) and (4) are identical and this circumstance reduces the number of equations in the system to three, but we have four unknown quantities. One equation must be supplied from outside of GR. Since there is no mathematical restriction, any equation, representing any definition, can be chosen. For example, Tolman (1939) assumed an ad hoc behavior of the auxiliary metric functions $\lambda = \lambda(r)$ and $\nu = \nu(r)$, specifically $e^\nu \nu' / (2r) = \text{const}$.

(Solution IV), $e^\nu = \text{const.}$ (Solution V), or $e^{-\lambda} = \text{const.}$ (Solution VI). Although such the additional assumption is only an author's fantasy, one can still obtain a toy model resulting from the mathematical solution of the EFEs.

Such a model is not, however, related to reality. It can answer the question of what would the internal structure of RCO look like if we assumed, e.g., $e^\nu \nu' / (2r)$ is equal to a constant. It is, however, questionable if the RCO model with such a structure could be applied to a real object. The fact that such the model is irrelevant to reality can be also seen from the discrepancy that a specific real RCO can be described by only one, unique, solution, but Tolman published seven various solutions and many other solutions were published by other authors. The behavior of no quantity in the RCO body can be guessed, when we deal with a model of a real object. From the point of view of physics, a correct way to solve the EFEs, in course to obtain a realistic model of RCO, is consideration of a realistic EoS, which is the input (the fourth equation) into the system of the EFEs. Then, solving the EFEs, one obtains a regular, realistic model of RCO.

As we argued in Sect. 4.1, the numerical modeling of RCO always implies an object in the form of a hollow sphere. An exception is an RCO consisting of the incomprehensible perfect fluid. The incomprehensibility implies a resistance of fluid against a deformation. Such the fluid would have a constant density, ρ , throughout the RCO's body. Several solutions of the EFEs applicable to the RCOs of this kind were found, e.g., the solution published by Schwarzschild (1916) or Solutions I–III by Tolman (1939). Nevertheless, the gravity is oriented outward in the innermost region also in the objects constructed on the basis of these solutions. The distribution of matter down to the center is caused by the incomprehensibility.

The objects described by the models with an artificially defined behavior of a quantity in their bodies, like that in the papers by, e.g., Tolman (1939); Buchdahl (1967), or Whittaker (1968), could, perhaps, be artificially constructed. However, they would have been constituted of a solid material, with a significant tensile strength. The strength, resisting a deformation of material, should be then taken into account and other stress-energy tensor than that for a perfect fluid, defined by relation (7), should have to be used. The stress-energy tensor (7) and corresponding EFEs (9)–(11) are not relevant to a solid matter. Hence, the solutions implying the fulfilled-sphere RCOs, published by the above-mentioned authors, are ruled out as contra-examples of the necessity of hollow-sphere configuration of gaseous RCOs.

Taking into account this circumstance, we are forced to state that no model of RCO, which would have been completely described (from RCO-centric distance $r = 0$ to $r = \infty$), has ever been constructed and published. This is in a contrast with the hollow-sphere models, one of which is just published in this paper and other models were published in our past papers as well as in the paper by other authors (the references to these papers are given in Sect. 1).

5. Energy of RCO

5.1. General formulas. Mass

In GR, the energy, W , of a static, spherically symmetric RCO can be calculated as the integral of energy density, E , through the RCO's volume, i.e. from its inner surface with radius R_{in} to its outer surface having radius R_{out} . Specifically (e.g. [Straumann, 2013](#); [Misner et al., 2017](#), but with $R_{in} \equiv 0$, there),

$$W = 4\pi \int_{R_{in}}^{R_{out}} r^2 E dr. \quad (43)$$

If we take into account EFE (10), the integrand $r^2 E$ equals

$$r^2 E = \frac{2}{\kappa} \frac{du}{dr} = \frac{c^4}{4\pi G} \frac{du}{dr} \quad (44)$$

and relation (43) can be re-written as

$$W = \frac{c^4}{G} \int_{R_{in}}^{R_{out}} \frac{du}{dr} dr = \frac{c^4 u_{out}}{G} - \frac{c^4 u_{in}}{G} \quad (45)$$

where we denoted $u(R_{in}) = u_{in}$ and $u(R_{out}) = u_{out}$. It appears that the inequalities $u_{in} < 0$ and $u_{out} > 0$ are always valid. Hence, the energy $W = |c^4 u_{out}/G| + |c^4 u_{in}/G| > 0$, i.e. the energy is positive.

5.2. A remark on quantity u in the context of mass

As we stated in Sect. 3.2, the parameter u_c can be calibrated, after it is multiplied by the constant c^2/G , with the help of Newtonian mass. However, is the quantity $u_c c^2/G$ really a mass? We know that each quantity in the unit of length multiplied by c^2/G becomes the quantity of the unit of mass. For example, a vector $\mathbf{r} = (x, y, z)$ multiplied by c^2/G changes to $\mathbf{m}_r = (m_x, m_y, m_z)$, i.e. its components are quantities in the unit of mass. An object may be located at a position, where one or more of its components x , y , or z , and, hence, m_x , m_y , or m_z are negative. Can we say that the object cannot be in any such a position because a ‘‘mass’’ must not be negative? Of course, this would not be a reasonable demand. At the same time, we cannot demand that the negative values of the quantity uc^2/G must be forbidden.

In GR, the quantity uc^2/G cannot be regarded as a mass despite its unit, which is a unit of mass. Its different character can be demonstrated in the following deduction. Let us consider a small volume inside a neutron star body. (Here, it is not important whether we describe this star by the old, fulfilled-sphere RCO concept or by new, hollow-sphere concept.) Its energy, W , is the integral of energy density through this volume. Since $E > 0$, here, $W > 0$ and also mass $M = W/c^2 > 0$. However, if we consider such a volume in the vacuum

above the outer surface, $E = 0$ and, consequently its integral through the volume is zero, therefore $M = W/c^2 = 0$. But the space-time in the vacuum above the outer surface is curved; it is described by the OSM with the metric parameter $u_c > 0$ and, hence, $uc^2/G > 0$ in the place of the considered small volume. We see that uc^2/G cannot be mass. A quantity cannot be zero and non-zero at the same time.

In each realistic model of RCO that we or other authors created, the energy density was considered to be positive in any part of the RCO body. Therefore, its integral, corresponding energy as well as the corresponding mass were only positive (or zero in the vacuum below the inner and above the outer RCO surfaces). A negative value of uc^2/G in the region $r < r_z$ of RCO is acceptable, since it is not a mass.

The metric quantity u is an alternative form of the g_{rr} component of the metric tensor (see relation (8)). If $u \geq 0$, then g_{rr} ranges from $-\infty$ to -1 . However, one can ask why is this component of metric tensor constrained by the value of -1 ? In physics, it is reasonable to demand a negative (in the $---+$ signature), real-valued g_{rr} , but there is no argument why the interval from -1 to 0 should be ruled out. In other words, why should $u < 0$ be ruled out?

5.3. Hidden energy and other kinds of energy

In Sect. 4.3, we already mentioned that there can always be found such a distance r_z inside the RCO body, where the auxiliary metric function u equals zero. In an attempt to represent terms $c^4 u_{out}/G$ and $-c^4 u_{in}/G$ in the result of the energy calculation (45), we can divide the integration in this relation to two integrations (deLyra, 2023),

$$W_h = \frac{c^4}{G} \int_{R_{in}}^{r_z} \frac{du}{dr} dr = \frac{c^4 u_z}{G} - \frac{c^4 u_{in}}{G} \quad (46)$$

and

$$W_{out} = \frac{c^4}{G} \int_{r_z}^{R_{out}} \frac{du}{dr} dr = \frac{c^4 u_{out}}{G} - \frac{c^4 u_z}{G}. \quad (47)$$

Since $u_z \equiv u(r_z) = 0$, $u_{in} < 0$, and $u_{out} > 0$, these relations reduce to

$$W_h = -\frac{c^4 u_{in}}{G} = \left| \frac{c^4 u_{in}}{G} \right|, \quad (48)$$

$$W_{out} = \frac{c^4 u_{out}}{G} = \left| \frac{c^4 u_{out}}{G} \right|. \quad (49)$$

The acceleration above the outer RCO surface is proportional to u_{out} which corresponds to the Newtonian mass M_{out} according to relation (42). If we observationally determine the mass of RCO, i.e. the mass of a neutron star or a super-massive object in the center of a galaxy or a quasar, then we determine

the Newtonian mass M_{out} corresponding to u_{out} which yields the corresponding energy content W_{out} according to relation (49). The whole energy content is, however, the sum $W_h + W_{out}$. Hereafter we refer to energy W_h as the “hidden energy” and to energy W_{out} as the “outer-region energy”. In the Newtonian physics, we have only a single concept of energy. The “energy” and “rest energy” are not distinguished. At the same time, there is no hidden energy. The hidden energy is another kind of energy, which should be recognized in GR.

In GR, there has been sometimes considered the “mass within the sphere of radius r ”. This kind of mass should be abolished. In the context of our analysis, it seems reasonable to consider only a “mass between the spheres of radii r_z and r ”.

We note that the hidden energy is significant only in the truly relativistic objects, which cause a significant curving of space-time. In the non-relativistic objects, GR alone (without any postulate) implies $R_{in} \rightarrow 0$ and, consequently, $W_h \rightarrow 0$. One can illustrate this fact by the model of the Sun, which is not very relativistic object. Here, we present only a simple model constructed by using of the equation of state, which is a combination of the polytrope and the equation state of radiation - see relations (20) and (22). We considered the polytrope to be index equal to 3.

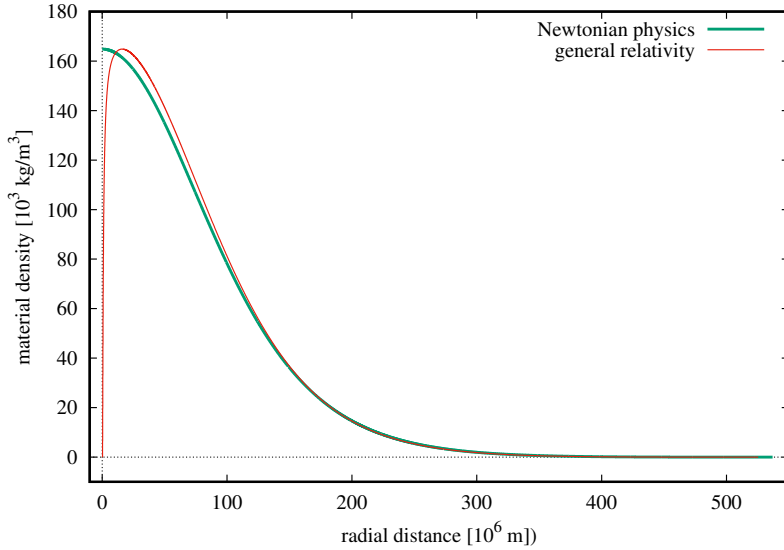


Figure 5. The behavior of the material density, $\rho(r)$, in the Sun’s interior according to its polytrope model described in Sect. 5.3 (the red curve). The corresponding behavior in the model constructed by using the Newton gravitational law is also shown (the green curve).

To obtain the minimum energy configuration of the solar body (the minimum energy configuration of RCO is discussed more in Sect. 5.4), we construct a series of models by varying the zero-gravity distance, r_o . Further, the mass of the object in the model must be equal to $1 M_\odot$. To achieve this mass, we considered the fixed maximum temperature and varied the maximum pressure (both quantities reach their maximum at the distance r_o). Other possibility is to fix the maximum pressure and vary the maximum temperature. However, it appears that the resulting model is almost the same in both cases. The maximum temperature and pressure as well as the chemical composition of the Sun were taken from the standard solar model by [Turck-Chieze et al. \(1988\)](#) (their reference model).

The behavior of the material density inside the Sun's model is shown in Fig. 5 (the red curve). For the sake of a comparison, the polytrope model of the Sun constructed by the Newton gravitational law is also shown (the green curve). We can see that the models are identical in a prevailing volume of the solar body. A difference occurs in a very small volume, in the central region. Specifically, $R_{in} \sim 10^{-4}$ m (but density, ρ equals $10^{-5} \rho_{max}$ already in $r = 218$ km), $r_o = 1.6 \cdot 10^4$ km, and $R_{out} = 5.239 \cdot 10^5$ km. The hidden mass (W_h/c^2) equals only $0.0014 M_\odot$.

5.4. Minimum energy configuration of RCO

If an RCO possesses not only an outer surface, but an inner surface and a non-zero zero-gravity distance as well, then there is one more degree of freedom. It is, thus, reasonable to ask what a configuration will be acquired. For a set of particles constituting a given RCO, it will obviously be the configuration at which the object has the minimum energy.

Assuming that an RCO consists of η neutrons, its rest mass equals $M_o = \eta m_n$ regardless the configuration acquired. So, let us construct a series of models for the RCO with the rest mass equal to $M_o = 5 M_\odot$, for example. No relation between the Fermi impulse in a starting point of numerical integration and the rest mass of the RCO is known. The required rest mass can be achieved via an iteration, when we vary the input value of the impulse in the starting point. The individual models in the series differ by their zero-gravity distance, r_o . When this distance is given, then the inner and outer radii of RCO are yielded by modeling.

Having the series of the models, we can investigate the dependence of the RCO's total energy on the zero-gravity distance ([Neslušan, 2019](#)). The dependence is shown in Fig. 6 in our example. Actually, there is a model of RCO with the minimum energy, for $r_o \doteq 25$ km. So, the object will tend to acquire the configuration with this value of r_o . The RCOs with $M < M_o$ (those below the cyan horizontal line in Fig. 6) obey the binding energy condition for a stable configuration (see Sect. 6.1), the minimum energy configuration including.

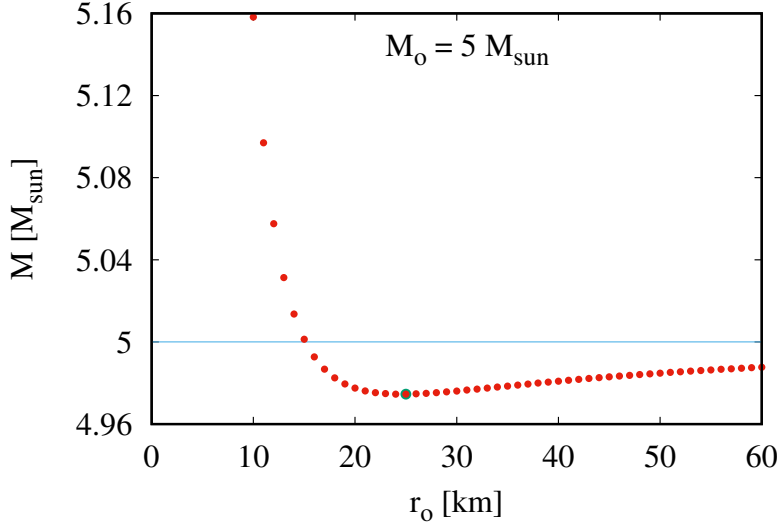


Figure 6. The dependence of total energy, W , in term of mass, $M = W/c^2$, on the zero gravity distance, r_o , for a series of RCO models, all with the rest mass $M_o = 5 M_\odot$. The RCO with the minimum total energy is shown with the green circle (around the red full circle). The zero-gravity distance of this RCO is $r_o = 25$ km. The cyan horizontal line separates the solutions obeying the binding-energy condition of stability (below the line) from those being in the unstable equilibrium configuration (above the line).

On the contrary, the objects with $M > M_o$ are in an unstable equilibrium configuration. Since the total energy decreases with the increasing r_o in the region of instability, these objects should expand after a perturbation occurs. We constructed the $M = M(r_o)$ dependence for many values of the rest mass; except for the example for $M_o = 5 M_\odot$ presented here, five other examples were presented in our previous paper (see Fig. 5 in Neslušan, 2019). The minimum of the function $M = M(r_o)$ always occurred in the region of the stable-equilibrium configuration.

In Fig. 6, we can observe a steep increase of the energy when $r_o \rightarrow 0$. It means that the fulfilled-sphere configuration is highly unstable.

The dependence of the outer radius, R_{out} , on the zero-gravity distance, r_o , for various configurations of RCO with the same rest mass in the context of the RCO's event horizon is shown in Fig. 7. (In the figure, the example of RCO with the rest mass of $5 M_\odot$ is presented.) We can see that the outer radius approaches the gravitational radius (the purple curve) when the zero-gravity distance decreases to small values (in the small window showing the detail, the purple curve seems to approach, asymptotically, the blue one). However, when

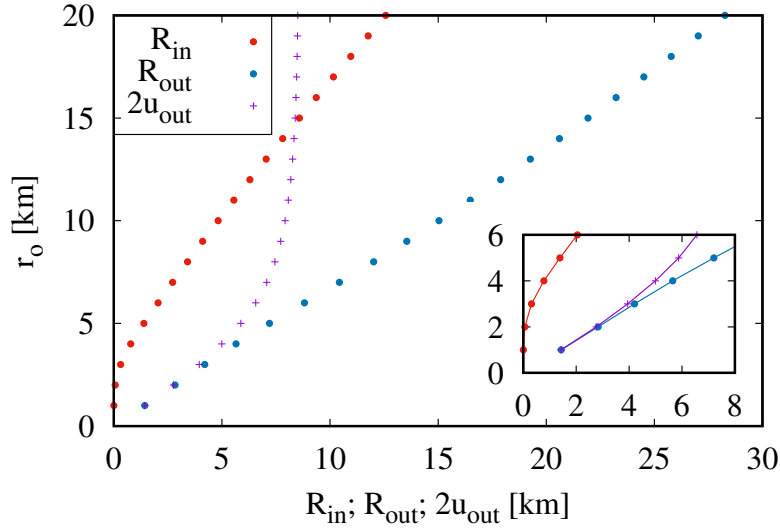


Figure 7. The extent of the RCO with the rest mass $M_o = 5 M_\odot$, from the inner radius, R_{in} (red circles), to the outer radius, R_{out} (blue circles). This extent in the horizontal axis is shown in the dependence on the zero-gravity distance, r_o , on the vertical axis. (The distance between two, red and blue, points at the same horizontal level is the extent.) The behavior of the gravitational radius, $2u_{out}$, as the function of r_o for the $5 M_\odot$ -RCO is shown with the purple crosses. In the small window showing a detail at the smallest radii and r_o , the points resulting from the discrete models are connected with the curve of the corresponding color to demonstrate the approach of the outer radius to the gravitational radius when $r_o \rightarrow 0$.

$r_o \rightarrow 0$ then the energy of the object increases as seen in Fig. 6. This fact is even more transparent in Fig. 8 showing the dependence of the difference between the outer RCO radius and the radius of the event horizon on the total energy of the object. We see that the outer radius decreases to reach the event horizon with the increasing energy. In other words, the dependence indicates that a collapse of the object to a black hole requires the delivery of a huge, possibly infinite, amount of energy.

Unfortunately, no analytical, even an analytical static, general solution of the EFEs describing a realistic RCO is known (except for the solution for a photon sphere; see Sect. 7.3), therefore it is impossible to answer the question whether the energy required for a collapse is finite or infinite. At the moment, we have only the indication that some energy is needed. The definitive conclusion on the required energy could be drawn if we knew the analytical solution (the dynamical case) of the EFEs describing the collapse.

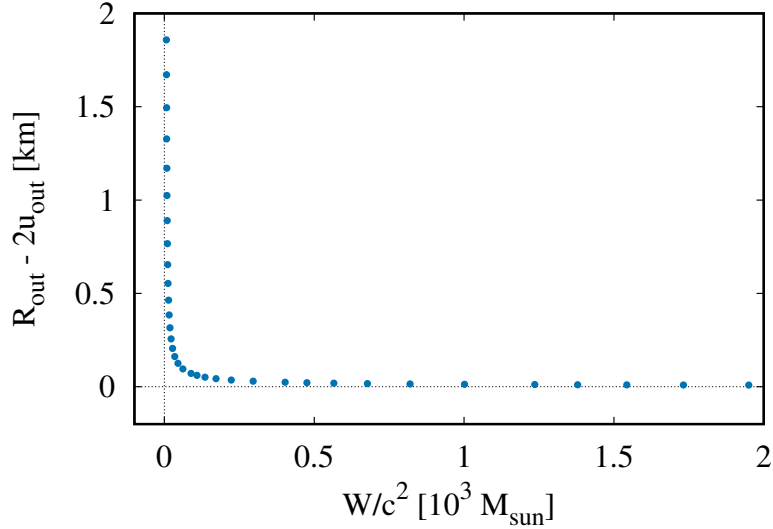


Figure 8. The dependence of the difference between the outer radius of a neutron star, R_{out} and radius of its event horizon, equal to $2u_{out}$, on the total energy, W , given in terms of the corresponding mass, $M = W/c^2$. Here, the example of the star with the rest mass $M_o = 5 M_\odot$ is considered; the blue circles correspond to the individual models of RCO with this rest mass.

5.5. On the maximum mass of RCO

In their pioneering work, [Oppenheimer & Volkoff \(1939\)](#) concluded that the mass of a stable neutron star cannot exceed a certain limit. Today, this limit is known as the Oppenheimer-Volkoff upper-mass limit. We know that these authors considered the objects in the shape of the fulfilled sphere. In this section, let us investigate if there is also a constraint on the mass of RCO in the shape of a hollow-sphere.

In [Fig. 9](#), there is shown the dependence of RCO mass on the maximum (in r_o) Fermi impulse, p_F , for several values of the zero-gravity distance. In panel (a) of the figure, the black solid curve shows the dependence for $r_o = 100$ m. The analogous curves for a smaller value of r_o could not be distinguished in the resolution of the figure, in the interval of reasonable values of p_F (~ 0.1 to $\sim 2m_n c$), from the black curve for $r_o = 100$ m. The behavior is practically the same for any value of $r_o < 100$ m, also for $r_o \rightarrow 0$. Hence, the black curve shown in [Fig. 9a](#) corresponds to the curve published by [Oppenheimer & Volkoff \(1939\)](#) in their [Figure 1](#). (These authors plotted the dependence of mass on a quantity that corresponded with the maximum Fermi impulse by a complicated, unclear, way. They presented only the part of the curve comprehending the

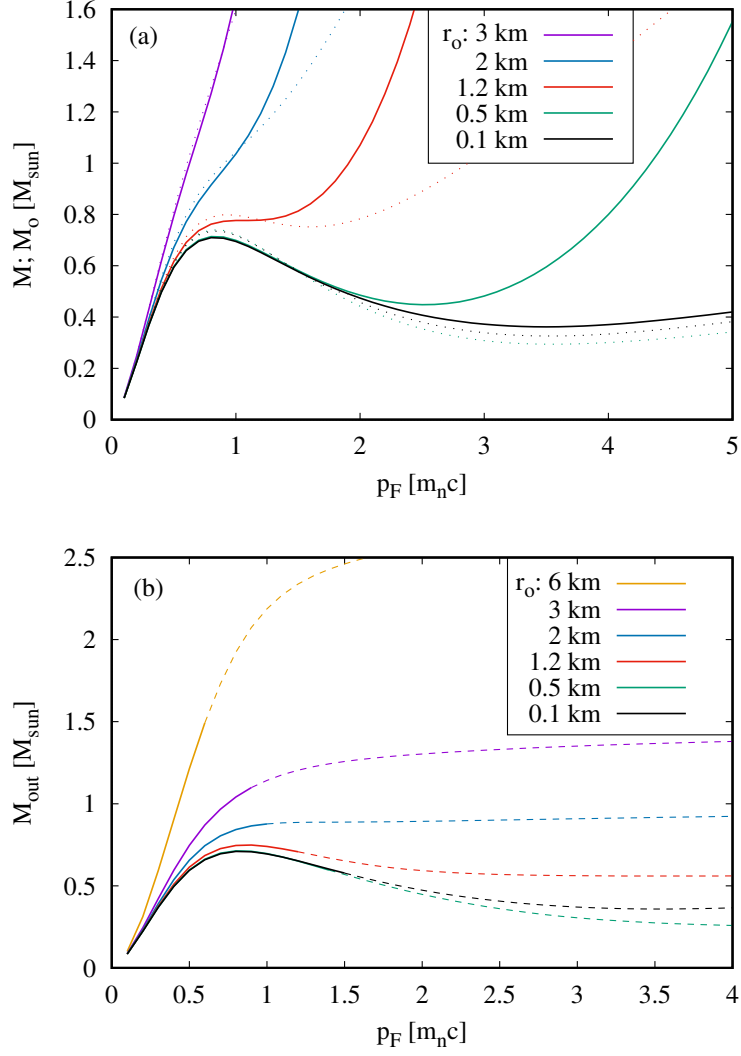


Figure 9. The dependence of the RCO mass, M , and the rest mass, M_o , on the maximum Fermi impulse, p_F , for several values of the RCO's zero-gravity distance, r_o (panel a). The thick solid curve of a given color shows the dependence of the mass and the dotted curve of the same color shows the dependence of the rest mass for the given r_o . In the intervals of p_F with $M_o > M$ (the dotted curve is above the corresponding solid curve), the RCO is in the stable-equilibrium configuration. In panel (b), there is the corresponding dependence of Newtonian mass M_{out} on p_F . The intervals of p_F where the RCOs are in the stable-equilibrium configuration are shown with a solid curve, the unstable-equilibrium RCO configurations are shown with a dashed curve.

models with a relatively small maximum Fermi impulse.) As seen, the curve has a local maximum at $p_F \approx 0.8 m_n c$. This fact has been the main argument for an existence of the upper-mass limit of neutron stars.

The green solid curve in Fig. 9a shows the dependence for $r_o = 500$ m. In the interval of p_F from a very small value (we created the models starting with $p_F = 0.1 m_n c$) to $\sim 2 m_n c$, it is situated only slightly above the black curve for $r_o = 100$ m, since there is no significant difference in the behavior for a small r_o as we mentioned. All curves for a small r_o have a local maximum, at $p_F \approx 0.8 m_n c$ or a slightly larger value of p_F . However, if the dependence is constructed for $r_o \doteq 1.2$ km (the red solid curve), then there is no maximum; only an inflection point at $p_F \approx 1.1 m_n c$. If $r_o > 1.2$ km, then the mass permanently increases with increasing p_F (the cyan curve for $r_o = 2$ km and the purple one for $r_o = 3$ km in the examples shown in Fig. 9a).

The real objects must be in the stable equilibrium configuration, i.e. $M < M_o$ according to the binding energy condition of stability (Sect. 6.1). In Fig. 9a, the dependence of the rest mass, M_o , on the maximum Fermi impulse, p_F , is shown with a dotted curve of the same color as the dependence $M = M(p_F)$ for a given r_o . The intervals of the stable equilibrium RCO configuration are those where the dotted curve is above the solid curve of a given color. We can see that the intervals of the stability range from a small p_F beyond the local maximum or beyond the point of smallest derivative in respect to p_F of each curve.

Let us now deal, again, with the modeled RCOs with $r_o < 1.2$ km. If we consider only the part of the dependence of mass on the maximum impulse, which is terminated before the curve reaches its local minimum (as [Oppenheimer & Volkoff \(1939\)](#) did), it seems that the previous maximum, at $p_F \approx 0.8 m_n c$, is the absolute maximum. However, as shown in Fig. 9a, a continuation of the dependence to large values of p_F reveals that there is a local minimum (at $p_F \approx 3.5 m_n c$ in the case of $r_o = 100$ m and at $p_F \approx 2.5 m_n c$ when $r_o = 500$ m) and mass again increases for a larger p_F -values. Of course, the behavior of the $M = M(p_F)$ dependence in the region of extreme values of p_F is irrelevant to real objects because of two reasons. First, the RCOs would be in an unstable equilibrium configuration (the black dotted or green dotted curves are below the black solid or green solid curve, respectively). Second, the extreme impulse p_F implies such a huge energy of neutrons that we can expect transmutations of the particles and, consequently, the considered EoS would no longer be valid. Hence, the continuation of the $M = M(p_F)$ dependence is interesting only from the point of view of mathematics.

If we deal with the RCOs in the shape of a hollow sphere, the mass corresponding to the outer-region energy is the quantity we measure in observations, as we already mentioned at the end of Sect. 4.3. The dependence of the measured outer-region - or Newtonian - mass, M_{out} , on the maximum Fermi impulse is shown in Fig. 9b, again for several values of r_o . The part of the dependence in the region of stable equilibrium is shown with a solid line (a continuation to

the region of the unstable equilibrium is shown with a dashed line). One can see that the maximum M_{out} in the regions of stability increases with increasing r_o .

When one constructs the dependence $M_{out} = M_{out}(p_F)$ for a large enough value of r_o , there is an indication that M_{out} (the measured “mass”) can, most probably, increase up to an arbitrarily large value. Without an analytical solution, we cannot prove if an increase above all limits is actually possible. Anyway, even if there is a maximum value of M_{out} , this value is, obviously, much larger for the hollow-sphere than the fulfilled-sphere RCO. In Fig. 9b, the maximum M_{out} of the stable RCO with $r_o = 6$ km (the orange solid curve) is $1.49 M_\odot$. If we search for the maximum in the series of RCO models for a larger r_o , for $r_o = 10, 15, 20, \text{ or } 25$ km for example (these results are not shown in Fig. 9b because of its better transparency), then the maximum M_{out} of RCO in the stable-equilibrium configuration $M_{out} = 2.14, 2.62, 3.18, \text{ or } 3.39 M_\odot$, respectively.

6. Condition of hollow-sphere-RCO stability and other conditions

6.1. Binding-energy criterion of RCO stability

EFEs (2)–(5) or those in form (9), (10), and (16) give a static solution for a RCO, therefore every RCO described by a solution of these equations must be in a balanced configuration. However, the RCO equilibrium can be stable or unstable. We are, of course, interested in the models of RCO in the stable equilibrium configuration. An RCO is in the stable equilibrium, if its binding energy is positive (Tooper, 1965), i.e.

$$W_{b.e.} = W_o - W > 0. \quad (50)$$

In the example of a neutron star presented in Sect. 4, the binding energy condition is obeyed because $Mc^2 < M_o c^2$ ($M = 4.97457 M_\odot$ and $M_o = 5.00000 M_\odot$). We remind that W_o and W are the rest energy and total energy of RCO, respectively. The rest energy is

$$\begin{aligned} W_o = M_o c^2 &= 4\pi \bar{m} \int_{R_{in}}^{R_{out}} nr^2 e^{\lambda/2} dr = \\ &= 4\pi \int_{R_{in}}^{R_{out}} \frac{\rho r^2}{\sqrt{1 - \frac{2u}{r}}} dr. \end{aligned} \quad (51)$$

The symbol \bar{m} stands for the mean mass and n is the number density of the RCO-constituting particles.

When condition (50) is applied, it is implicitly assumed that the generation of thermal energy in nuclear reactions is negligible, i.e. W_o is constant, and also the energy of radiation is negligible. However, the energy of radiation is

sometimes a significant or dominant type of energy, so far, therefore we have to modify the condition for the stable equilibrium given by inequality (50).

The modification is necessary, since the energy of the radiation of a RCO in thermal equilibrium cannot be converted into the kinetic type energy of gas particles; there is no contribution of energy from the radiation helping these particles to overcome the RCO's potential barrier. The radiation tends to be in the thermodynamic equilibrium with the gas (plasma). Some radiation energy could be delivered to the gas (causing an increase of its energy and, hence, temperature) only if the temperature of radiation decreased, but this would contradict the second law of thermodynamics. Therefore, when the energy of radiation is significant, the binding energy should be calculated as

$$W_{b.e.} = W_o - W_g, \quad (52)$$

where $W_g = W - W_r$ is the total energy reduced by the energy of radiation, W_r .

We note that Tooper's binding-energy criterion for stability was abandoned in the works published in the last decades. The stability has been mostly evaluated performing the perturbation analyses. The reason of why the binding-energy criterion was abandoned has never been given, however. The condition (50) or (52) should be the primary condition of stability. If it is not obeyed, the object cannot be stable. Namely, if there is enough energy to overcome the gravitational potential of an object, the object must expand. We can compare this to the celestial-mechanics problem of two bodies the integral of their energy is positive. Then, we cannot say that one object remains in a bound, elliptical, orbit around the other. It must move in the unbound, hyperbolic, orbit.

6.2. Other conditions to describe a real object

To create a model relevant to a realistic RCO, several conditions in addition to the binding-energy condition were published by various authors. In this section, we discuss some of these conditions, as summarized by Ivanov (2017) and recently discussed by Hernández et al. (2021). Some of the conditions are, however, relevant only to the RCO in the shape of the fulfilled sphere, therefore we omit them in this section, but are discussed in Sects. 4.4, 4.5, and 7.

Except for the demand on the positive binding energy, the following conditions for an isotropic RCO should be mentioned.

(1) Components of the metric tensor, e^λ and e^ν , are positive, finite, and free from any singularity within the matter distribution.

(2) At the surfaces of the RCO, the RCO-body solution for the components of the metric tensor should match continuously their counterparts in the OSM. In other words, the components of the RCO-body metric tensor and their derivatives in respect to r should equal to the corresponding components and their derivatives in the OSM at both RCO surfaces. In the case of the spherically symmetric RCO, having non-zero only the diagonal components of the

metric tensor, the spatial transversal components, $g_{\theta\theta}$ and $g_{\varphi\varphi}$, are identical in the RCO-body metrics and OSM, therefore their matching is obvious. There is also the match of the g_{rr} component and its derivative due to the intrinsic consistency of GR.

However, the g_{tt} component is not present in the EFEs; there is only the derivative of the auxiliary function ν . Hence, g_{tt} is not uniquely determined by the EFEs and its tailoring deserves an attention. The fact that the derivative $d\nu/dr$ can be found solving the EFEs means that the behavior of ν , as a function of the distance r , is given, but there is an unknown integration constant, ν_K , which can be added to the function $\nu = \nu(r)$ at every r .

The value of the constant ν_K suitable for the tailoring can be found either in an iteration or in the following way. We start the numerical integration with an arbitrary initial value, ν_a , of the function ν and perform the integration to the outer radius, R_{out} . The integration yields a value of ν , which we denote ν_{Ra} , at R_{out} . At the same time, the integration yields the value, u_{out} , of the function u at R_{out} , therefore we can calculate the relevant g_{tt} component in the OSM in R_{out} : $g_{tt}(R_{out}) = 1 - 2u_{out}/R_{out}$. The corresponding ν equals $\nu_{OSM} = \ln(1 - 2u_{out}/R_{out})$. Obviously, constant $\nu_K = \nu_{OSM} - \nu_{Ra}$. The initial value of ν suitable for the tailoring, which we denote by ν_b , is equal to $\nu_a + \nu_K$, explicitly

$$\nu_b = \nu_a + \ln\left(1 - \frac{2u_{out}}{R_{out}}\right) - \nu_{Ra}. \quad (53)$$

We implicitly assumed the calibration $K_{\nu,o} = 1$ in the calculation of ν_b . If the integration is repeated, whereby ν_b is used as the input, it yields the behavior of g_{tt} which can be tailored to its OSM counterpart at R_{out} .

(3) The pressure should vanish at the surfaces, except for radiation pressure. (We consider the isotropic solution, therefore we do not distinguish between the radial and tangential components of the pressure.) We require, in addition, the material density should vanish at the RCO surfaces.

(4) The energy density and pressure should be positive inside the RCO body. For the energy density this demand coincides with the null energy condition. If both pressure and energy density are positive in the RCO's body, then all energy conditions, except for the dominant and strong (see the next item), are obeyed.

(5) The dominant energy condition should be satisfied, i.e. $E \geq P$, anywhere inside the RCO body. It is desirable that even the strong energy condition is satisfied. This condition requires $E \geq 3P$.

(6) The causality condition should be satisfied. It says that the speed of sound should not surpass the speed of light, or $0 < dP/dE \leq 1$.

(7) The adiabatic index, $\Gamma = [(E + P)/P]dP/dE$, which is the ratio of two specific heats, should be $\Gamma \geq 4/3$.

(8) The distribution of mass obeys the principle of minimum action. The total energy of RCO is minimal possible energy for the set of particles of gas

constituting the object.

We found that, for a reasonable EoS, all these conditions are obeyed for a large variety of RCOs. Condition (1) is satisfied for every real-values λ and ν and these quantities are real-valued if all components of the metric tensor are real. For several EoSs we also proved that the behavior of all quantities in the RCO body is continuous, without any singularity. As well, it is possible to prove, for the specific EoSs, that there are always the inner and outer surfaces in which the material density vanishes and the OSM can be smoothly tailored to the metrics of the RCO-body.

If the EoS for radiation or a polytrope with radiation is considered, then the energy density and pressure are non-zero down to the exact center of the object and up to the infinite distance from it. However, even in the case of a radiation sphere, there is a steep decrease of the pressure and energy density in two finite object-centric distances. The first can be regarded as inner and the second as the outer physical surface. Below the inner and above the outer surface the metrics can be well approximated with the OSM (an example can be found in (Neslušan, 2017b) or (Neslušan, 2017a)). Thus, conditions (2) and (3) are obeyed, practically.

The reasonable EoS, i.e. the EoS to describe a real object, contains only the positive energy density and pressure, therefore the obeying of condition (4) is obvious. For the EoS given by relations (13)–(15), we can show that

$$E = 3P + \frac{m_n^4 c^5}{4\pi^2 \hbar^3} \sum_{j=1}^{\infty} \frac{1}{(2j+1)!} \left(\frac{\tau}{2}\right)^{2j+1}. \quad (54)$$

Hence, $E \geq 3P$ for $\tau \geq 0$, which is always the case. Therefore, condition (5), i.e. the dominant as well as strong energy conditions, are obeyed. The conditions are also obeyed for the EoS of radiation, $E = 3P$, and EoS in the form of a polytrope (relations (19) and (20)) when the polytrope index $N \geq 1$ (the dominant energy condition) or $N \geq 3$ (both dominant and strong energy conditions).

Causality condition (6) is also obeyed for all the three above mentioned EoSs. For EoS (14) and (15), we can show that

$$\frac{dP}{dE} = \frac{1 \cosh \frac{\tau}{2} - 1}{3 \cosh \frac{\tau}{2} + 1}. \quad (55)$$

For any positive τ , it is therefore valid $dP/dE > 0$ and dP/dE approaches $1/3$ when τ acquires large values. When $\tau \rightarrow 0$, then $dP/dE \rightarrow 0$. If $E = 3P$, then $dP/dE = 1/3$. For the polytrope, one can find

$$\frac{dP}{dE} = \frac{1}{N} \frac{(N+1)K_P \rho^{1/N}}{(N+1)K_P \rho^{1/N} + c^2}, \quad (56)$$

therefore $dP/dE < 1$ for $\rho > 0$ if $N \geq 1$.

In the case of EoS (14) and (15), the adiabatic index, Γ , is larger than $4/3$ and condition (7) is obeyed for large values of the Fermi impulse, p_F , and approaches $4/3$ when p_F decreases to zero. If the EoS is $E = 3P$, then $\Gamma = 4/3$. For the polytrope, $\Gamma = 1 + 1/N$, therefore condition (7) is obeyed for $N \leq 3$.

Concerning condition (8), we found that it can be obeyed (there is a minimum of the function $M = M(r_o)$) for the EoS of the cool, degenerated, Fermi-Dirac gas characterized with relations (14) and (15). We further found that it is also obeyed for polytrope (19) and (20), as well as the EoS which is the combination of the polytrope and EoS for radiation, $E = 3P$. On the contrary, no minimum of the function $M = M(r_o)$ was found for the EoS of the degenerated ion-electron gas, i.e. for the gas constituting the white-dwarf stars.

7. A confrontation of two concepts of RCO

In this section, we discuss the traditional fulfilled-sphere concept versus the new hollow-sphere concept of RCO.

7.1. On the requirement of the regularity of metrics

When a relativistic star or other object generating a strong gravity is modeled, it is demanded, among other things, that the metrics should be regular at the origin. The demand of regularity was specified by, e.g., Misner et al. (2017) (in their paragraph 23.5) who calculated the mass inside the radius r ,

$$M_r(r) = \int_0^r 4\pi r^2 E dr + M_r(0), \quad (57)$$

and argued that the constant of integration $M_r(0)$ must be zero. The first problem with Eq.(57) is the lower limit of the integration. It has always been assumed to be zero, but the question why it is zero has never been answered. This question is non-trivial in the GR. The zero lower limit means that the distribution of matter in the RCO is implicitly assumed to extend to its proper center. However, it means that the distribution is *assumed*, not proved.

According to the authors requiring the regularity of the metrics at the origin, the demand $M_r(0) = 0$, implying a space geometry that is smooth at the origin, is physically acceptable in contrast to a non-zero value, which means a geometry with a singularity at the origin and is physically unacceptable.

However, can the demanded equality $M_r(0) = 0$ be achieved within GR? This demand has never been proved to be possible. On the contrary, the equation of geodesic implies the relativistic term of the gravitational acceleration, which cannot be zero for an RCO of a non-zero mass and which implies that the outer layers of the RCO attract the layers below them outward from the RCO center. It is possible (although this has been proved neither) that there is always a finite RCO-centric distance, below which the net gravity of the outer layers

dominates over the downward oriented gravitational action of lower layers. Thus, there should necessarily occur, at the RCO consisting of a compressible fluid, an inner physical surface and the function $M(r)$ is zero at a finite object-centric distance. The demand $M_r(0) = 0$ can, paradoxically, be surely obeyed only after GR is ignored at a region around the RCO center.

The matter inside the RCO could be distributed down to its center, if we completed the demand $M_r(0) = 0$ with another demand that every RCO must consist either of an incompressible fluid or a solid material. In the case of solid material, the stress-energy tensor (7) is irrelevant and no else stress-energy tensor was considered. The demand of incomprehensibility would also be problematic, especially for the super-massive RCOs. Penrose (1969) pointed out that the mean density of an RCO decreases with its mass. An estimate of the mean density can be done in the following way.

Let us define the “compactness” of RCO, ζ , as the ratio of the gravitational Schwarzschild and outer-surface radii, i.e. $\zeta = R_g/R_{out}$. The mean density, $\langle\rho\rangle$, of the fulfilled-sphere RCO with the mass M equals $\langle\rho\rangle = 3M/(4\pi R_{out}^3)$. Let us consider two RCOs with masses M_1 and M_2 , which have the same compactness, i.e. there is valid $R_{g1}/R_{out1} = R_{g2}/R_{out2}$. From the latter,

$$R_{out2} = \frac{M_2 R_{out1}}{M_1}. \quad (58)$$

If one calculates the ratio of mean densities of both aforementioned RCOs, he or she obtains

$$\frac{\langle\rho\rangle_2}{\langle\rho\rangle_1} = \frac{3M_2}{4\pi R_{out2}^3} \left(\frac{3M_1}{4\pi R_{out1}^3} \right)^{-1} = \frac{M_2}{M_1} \left(\frac{R_{out1}}{R_{out2}} \right)^3. \quad (59)$$

When the outer radius of the second RCO, R_{out2} , is expressed by relation (58), the ratio of the mean densities equals

$$\frac{\langle\rho\rangle_2}{\langle\rho\rangle_1} = \frac{M_1^2}{M_2^2}. \quad (60)$$

It means, the mean density of RCO, being in the form of a fulfilled sphere, is reciprocally proportional to its mass squared. For example, if the mean density of a neutron star having the mass of order of $10^0 M_\odot$ is $\sim 10^{17} \text{ kg m}^{-3}$, then the mean density of a super-massive RCO with the mass of order of magnitude $10^9 M_\odot$ is 18 orders of magnitude smaller than the mean density of the neutron star, i.e. it equals about $10^{-1} \text{ kg m}^{-3}$. It is even smaller than the density of the Earth’s atmosphere at the Earth’s surface. This indicates that the regions of RCO with a relative small material density rather consist of a common gas than an incomprehensible matter or solid matter.

Misner et al. (2017) were right that there is a singularity at $r = 0$ if $M(0) \neq 0$. However, this singularity does not seem to be problematic as we argued in

Sect. 4.5. It is of the Big-Bang type and, therefore, an acceptable singularity and, until it exists, it cannot be visited, in principle, by any particle or object (observer). It can thus be regarded as a point of space-time not belonging to our universe.

7.2. One or two degrees of freedom?

When one demands the distribution of RCO matter down to its center, he or she arbitrarily cancels one degree of freedom. While the hollow-sphere RCO can acquire (i) a various zero-gravity distance, r_o , and (ii) a various thickness, i.e. difference $R_{out} - R_{in}$, the fulfilled-sphere RCO can have only various outer radius. From the point of view of GR, it is not clear what keeps the matter of the fulfilled-sphere RCO distributed down to its center. If one wants to create a model of the fulfilled-sphere RCO, he or she must ignore the second, relativistic, term of acceleration (29) when they determine the action of upper material layers onto the lower layers. It means that the relativistic acceleration is replaced in this case by its Newtonian counterpart, in fact. In the past, this replacement has escaped the experts' attention, since it has always been assumed implicitly. Or, the researchers kept in their minds the postulate of the Minkowski metrics inside the spherical shell.

When the stability of fulfilled-sphere neutron stars was proved via various perturbation analyses, it was likely just the ignorance of the relativistic term of acceleration causing a positive result. If the second degree of freedom is taken into account, then the fulfilled-sphere RCO (or RCO with a very small r_o) is highly unstable according to the binding-energy criterion.

7.3. Does a solution for the fulfilled-sphere RCO exist?

The question in the title of this sub-section could be answered if the analytical solutions of the EFE for the realistic EoS were known. Then, the problem of a fulfilled-sphere versus hollow-sphere concept of RCO could be solved. Unfortunately, an analytical solution of the EFEs is known only for one realistic EoS, the EoS of radiation $E = 3P$, i.e. a photon sphere.² If one considers, for example, the polytrope or the mixture of polytrope and radiation, one has to use numerical methods (Stephani et al., 2009, p. 250). In the following, we describe an indication of the answer at least in the case of the photon sphere.

For the EoS of $E = 3P$, the analytical solution was found by Hajj-Boutros (1989) in the form of the elliptic integral of the first kind. To reveal whether the solution for the RCO in the form of a fulfilled sphere exists, we however need only some simpler relations, which occurred as an intermediate result in Hajj-Boutros' derivation.

²We speak here about the realistic EoS in sense that this equation gives the relation between the pressure and energy density of a real entity (radiation).

In his work, the author used the isotropic coordinates with the auxiliary metric functions $\mu = \mu(r)$ and $\nu = \nu(r)$. The line element in these coordinates is defined as

$$ds^2 = -e^\mu(dr^2 + r^2 d\vartheta^2 + r^2 \sin^2 \vartheta d\varphi^2) + e^\nu c^2 dt^2 \quad (61)$$

and the analogs of EFEs (2), (3), and (5) with the components of the stress-energy tensor given by matrix (7) are

$$\kappa P = e^{-\mu} \left(\frac{\mu'^2}{4} + \frac{\mu'\nu'}{2} + \frac{\mu' + \nu'}{r} \right), \quad (62)$$

$$\kappa P = e^{-\mu} \left(\frac{\mu''}{2} + \frac{\nu''}{2} + \frac{\nu'^2}{4} + \frac{\mu' + \nu'}{2r} \right), \quad (63)$$

$$\kappa E = e^{-\mu} \left(\mu'' + \frac{\mu'^2}{4} + \frac{2\mu'}{r} \right). \quad (64)$$

Eq.(12) remains valid for the isotropic coordinates in the unchanged form.

[Hajj-Boutros \(1989\)](#) suggested to change the variable r :

$$\xi = \ln r. \quad (65)$$

In agreement with this author, we use a dot (double dot) to denote the derivative (second derivative) in respect to the new variable, ξ . One easily obtains $\mu' = e^{-\xi}\dot{\mu}$, $\nu' = e^{-\xi}\dot{\nu}$, $\mu'' = e^{-2\xi}(\ddot{\mu} - \dot{\mu})$, and $\nu'' = e^{-2\xi}(\ddot{\nu} - \dot{\nu})$. Subsequently, Eqs.(62)–(64) can be re-written, for $E = 3P$, as

$$S = \frac{1}{4}\dot{\mu}^2 + \frac{1}{2}\dot{\mu}\dot{\nu} + \dot{\mu} + \dot{\nu}, \quad (66)$$

$$S = \frac{1}{2}\ddot{\mu} + \frac{1}{2}\ddot{\nu} + \frac{1}{4}\dot{\nu}^2, \quad (67)$$

$$3S = \ddot{\mu} + \frac{1}{4}\dot{\mu}^2 + \dot{\mu}, \quad (68)$$

where we denoted $S = \kappa P e^\mu e^{2\xi}$.

Hajj-Boutros derived relations

$$\dot{\nu}^2 = A \sinh(\nu + \alpha) - 2, \quad (69)$$

$$\mu = -2\xi - \nu - 2 \ln(\dot{\nu}) + C_1, \quad (70)$$

where A , α , and C_1 are the integration constants. The last relation can be re-written as

$$\dot{\nu}^2 = \frac{C_\mu}{r^2} e^{-\mu-\nu}, \quad (71)$$

where $C_\mu = e^{C_1}$ is another constant. Comparing (69) and (71) and after some algebraic handling, we obtain

$$A \sinh(\nu + \alpha) - 2 = \frac{C_\mu e^{-\mu-\nu}}{r^2}. \quad (72)$$

Eq.(12) can be integrated (Tolman & Ehrenfest, 1930) and we obtain

$$P = P_o e^{-2\nu}, \quad (73)$$

where P_o is an integration constant corresponding with the maximum pressure. From the latter, $e^{-\nu} = \sqrt{\frac{P}{P_o}}$. This relation enables the replacement of the quantity ν with pressure, P , in Eq.(72), i.e.

$$\frac{A}{2} e^\alpha \sqrt{\frac{P_o}{P}} - \frac{A}{2} e^{-\alpha} \sqrt{\frac{P}{P_o}} - 2 = \frac{C_\mu e^{-\mu}}{r^2} \sqrt{\frac{P}{P_o}}. \quad (74)$$

Using notation $B = e^\alpha \sqrt{P_o}$ and $C_2 = e^\alpha C_\mu$, the last equation can be changed to the quadratic equation of the variable P ,

$$\hat{a}P^2 + \hat{b}P + \hat{c} = 0, \quad (75)$$

with coefficients

$$\hat{a} = (Ar^2 + 2C_2 e^{-\mu})^2, \quad (76)$$

$$\hat{b} = -2B^2 (A^2 r^2 + 8r^2 + 2AC_2 e^{-\mu}) r^2, \quad (77)$$

$$\hat{c} = A^2 B^4 r^4. \quad (78)$$

Now, we can investigate the behavior of the pressure and, at the same time, energy density (since $E = 3P$) in the center of RCO. The regularity of metrics in the center requires that the g_{rr} component of the metric tensor, which equals e^μ in the isotropic coordinates, must acquire a finite value. If e^μ is finite then $\hat{a} \rightarrow 4C_2^2 e^{-2\mu}$, $\hat{b} \rightarrow 0$, and $\hat{c} \rightarrow 0$ for $r \rightarrow 0$ and the roots of Eq.(75) are

$$P|_{1,2} = \frac{-\hat{b} \pm \sqrt{\hat{b}^2 - 4\hat{a}\hat{c}}}{2\hat{a}} \rightarrow 0. \quad (79)$$

Hence, our analysis results in the conclusion that a stable relativistic photon sphere cannot possess a form of the fulfilled sphere; the pressure and energy density in its center are falling to zero.

Of course, we still do not know the behavior of the pressure and energy density in the center of RCO consisting of a gas described with the realistic EoS, as the polytrope, or EoS of the cool, degenerated, Fermi gas, or other, more sophisticated EoS. However, the above-mentioned conclusion indicates that the fulfilled-sphere configuration of RCO is not obvious.

7.4. Remarks about the concept of black hole

At the hollow-sphere RCO, we cannot avoid the singularity in its center. However, we cannot either avoid a singularity at the fulfilled-sphere RCO, those with the mass above the Oppenheimer-Volkoff limit. For a very massive object, we have to accept their collapse and singularity at the event horizon. The experts attempted to demonstrate that the singularity at the distance $r = R_g$ (i.e. at the event horizon) is just a coordinate artifact. Several coordinate transformations with no singularity in any component of the metric tensor were found and this was used as the argument.

However, GR is based, except of other, on the principle that the line element is invariant under any transformation within this theory. Therefore, if the line element, ds , in one coordinate system contains a singular point, the line element ds' in every other (“dashed”) coordinate system must also contain the corresponding singular point. It means that the singularity cannot be removed, in principle.

One can demonstrate the fact that there is always valid that $ds^2 = ds'^2$ in the case of, e.g., the Kruskal-Szekeres coordinates which are well known to be used in the incorrect proving that $r = R_g$ is not a genuine singularity. In these coordinates, new variables X and T are defined as

$$X = \sqrt{\frac{r}{R_g} - 1} e^{r/(2R_g)} \cosh\left(\frac{ct}{2R_g}\right), \quad (80)$$

$$T = \sqrt{\frac{r}{R_g} - 1} e^{r/(2R_g)} \sinh\left(\frac{ct}{2R_g}\right), \quad (81)$$

in the region above the event horizon. (In the region below the event horizon, variables X and T are defined by the similar relations. Considering them, the same conclusion as we draw below can be derived.) The line element squared, ds'^2 , in the new coordinates can be given as

$$ds'^2 = \frac{4R_g^3}{r} e^{-r/R_g} (dX^2 - dT^2) + r^2 d\vartheta^2 + r^2 \sin^2 \vartheta d\varphi^2 \quad (82)$$

(the $+++-$ signature is used, here). Actually, there is no singular point at any distance $r > 0$ in forms $(4R_g^3/r)e^{-r/R_g}$, r^2 , or $r^2 \sin^2 \vartheta$.

When we, however, calculate the differential $dX^2 - dT^2$ squared, we obtain

$$\begin{aligned} dX^2 - dT^2 &= \left(\frac{1}{2R_g} e^{r/(2R_g)}\right)^2 \\ &\cdot \left[\left(\frac{r}{R_g}\right)^2 dr^2 - \left(\frac{r}{R_g} - 1\right) c^2 dt^2 \right]. \end{aligned} \quad (83)$$

We see that $dX^2 - dT^2 \rightarrow \infty$ and, then, $ds'^2 \rightarrow \infty$ for $r \rightarrow R_g$. The singularity does not disappear in the new (dashed) coordinate system. In addition, the differential of any quantity should acquire an infinitesimally small value. Otherwise, one basic assumption of the differential calculus is violated. It means that the Kruskal-Szekeres coordinates should never be used in the vicinity of R_g .

The collapse of very massive fulfilled-sphere RCOs below their event horizon was not accepted by some GR experts. It is well known that Einstein and Eddington were reluctant to the concept of a black hole. Concerning this object, Eddington wrote (Chandrasekhar, 1972): *“Chandrasekhar shows that a star of mass greater than a certain limit remains a perfect gas and can never cool down. The star has to go on radiating and radiating and contracting and contracting until, I suppose, it gets down to a few kilometers’ radius when gravity becomes strong enough to hold the radiation and the star can at least find peace. I felt driven to the conclusion that this was almost a reductio ad absurdum of the relativistic degeneracy formula. Various accidents may intervene to save the star, but I want more protection than that. I think that there should be a law of Nature to prevent the star from behaving in this absurd way.”* Our result indicates that Eddington could be right. There actually exists the “law of Nature” which can prevent the star from an infinite collapse. It is the relativistic gravity itself. Deeply inside the compact object, there appears such a position of the mass center of the dominant-gravity matter that the net gravitational attraction becomes oriented outward from the object’s center.

In Sect. 5.4 we stated that we do not know, at the moment, whether the energy needed for the gravitational collapse is finite or infinite. If this energy were finite, then black holes would be possible, although not necessary, a final stage of very massive objects without the internal energy source. If the energy were infinite, the black holes would be energetically forbidden and, thus, impossible as Eddington claimed.

The skepticism concerning the black-hole concept seems to be in a contradiction with the claims of some experts who said the collapse of a very massive object below its event horizon was proved in the papers by Oppenheimer & Volkoff (1939) and Oppenheimer & Snyder (1939). A detailed inspection of the first paper however reveals that Oppenheimer and Volkoff discovered that there is no solution of the EFEs for a stable neutron star with the mass exceeding the upper mass limit. In their era, there existed the models of stars and planets within the Newtonian gravity which was oriented toward the center throughout the whole body of object. It is therefore not very surprising that they assumed a collapse of an unstable object.

In their paper, Oppenheimer and Snyder considered the previous conclusion drawn by Oppenheimer and Volkoff that a massive compact object had necessarily to collapse and, based on this conclusion, they *described* the collapse when the gradient of pressure to resist the gravitational attraction is negligible. Their work cannot be a proof of the collapse since such a proof can only be done when one evaluates both the strength of the gravitational attraction

and oppositely acting gradient of pressure and demonstrates that the gravity is dominant (Neslušan, 2019). But the gradient of pressure was not evaluated by the authors.

It is worth noting that the non-existence of black holes would not be in a disagreement with observations. Murk (2022) studied the observability of the black holes and argued that “identifying the observed astrophysical black hole candidates as genuine black holes is not justified based on the currently available observational data”. Actually, it is necessary to realize that various phenomena, which are today ascribed to the black holes, occur due to a strongly curved space-time in the vicinity of compact objects. However, such the space-time can also be configured by a dark RCO, which is not collapsed below its event horizon.

8. Conclusions

In our paper, we demonstrated of how GR works, indeed, in the astrophysics of the RCOs. The particular conclusions follows.

(1) The formula to calculate a gravitational acceleration consists, basically, of two terms, Newtonian and relativistic. The relativistic term represents a repulsive gravity which weakens the attractive Newtonian term in the region of space above the event horizon.

(2) Due to the relativistic term in acceleration, there always occurs an outward oriented gravitational action in the central region of a spherically symmetric distribution of matter.

(3) In the RCOs with their mass smaller than the Oppenheimer-Volkoff mass limit, the volume of the region of the outward oriented gravity can be arbitrarily small. At the moment, we do not know if the volume of the region can be zero. This circumstance enabled to postulate the metrics without a singularity in the center of RCOs and, practically, create the models of RCOs in the form of (an approximate) fulfilled sphere, with the matter distributed down to the RCO center.

(4) The EFEs imply the RCOs, consisting of a compressible perfect fluid, in the form of a hollow sphere. Inside such an RCO, there exists an RCO-centric distance below which the metric quantity u , related to the g_{rr} component of the metric tensor, is negative. The corresponding energy is, however, positive. We named this energy as “hidden energy”. This kind of energy never occurs within the Newtonian physics. It was found that its value can be several orders of magnitude larger in the super-massive RCOs than the value of their energy derived from the detectable Newtonian mass, which determines the acceleration of the objects above the RCO’s outer surface.

(5) A model of a traditional, fulfilled-sphere RCO (or a quasi-fulfilled sphere RCO in fact) can be constructed only with a mass smaller than the Oppenheimer-Volkoff upper mass limit. Since no analytical solution of the EFEs exists to de-

scribe a real RCO, it is unknown whether there is or is not a mass limit in the case of hollow-sphere RCOs; if so, then this limit must be considerably larger than the Oppenheimer-Volkoff limit.

(6) When it is postulated that any realistic RCO must be in the form of a fulfilled sphere, then the essential part of the solutions of the EFEs is forbidden. Due to this prohibition, there occurs the Oppenheimer-Volkoff upper mass limit and scientists are forced to establish the concept of a black hole to describe a final stage of more massive objects. Thus, the concept of a black hole is not implied by GR, but it appeared, on the contrary, due to the prohibition of the large, essential, part of this theory.

(7) To construct a model of RCO in the form of a fulfilled sphere, one must cancel one degree of freedom; only the RCO outer radius is variable in this case. He or she must, usually implicitly, assume a fictitious force keeping the distribution of RCO matter down to its center. The hollow-sphere RCO consisting of a given set of constituting particles can have a various zero-gravity distance and thickness; thus, there are two degrees of freedom.

(8) The stable-equilibrium configuration of a hollow-sphere RCO consisting of a given set of constituting particles occurs for a zero-gravity distance, which is significantly larger than zero. If this distance decreases, the RCO's total energy increases. If the zero-gravity distance is smaller than a certain limit, the object is in an unstable-equilibrium configuration. If the zero-gravity distances approaches zero, i.e. the hollow-sphere RCO is going to become the fulfilled-sphere object, its energy is tremendous (possibly approaching infinity) and its stability is very problematic.

(9) There is no singularity in the center of the fulfilled-sphere RCO. However, this smoothness of metrics is only postulated, at the moment. No solution of the EFEs for a realistic EoS implying a non-singular central point has ever been found. The singularity in the hollow-sphere-RCO center, i.e. in the center of its internal vacuum void, is the Big-Bang type singularity; everything is attracted away from the center. Hence, this singularity does not represent any problem. (If the Big-Bang type singularity was not acceptable, the theory of Big Bang would be incorrect.) Furthermore, this singularity is an abstract singularity, which exists in our description of the metrics in the vacuum void. In principle, no material particle can ever enter the singularity until it exists. The singularity is removed by an object with an energy comparable with the energy of the RCO, when this object occurs in the void.

In conclusion, we should seriously consider the concept of the hollow-sphere RCO with the outward oriented gravitational action and negative metric function u in its most central region. Although this concept includes a Big-Bang type, abstract singularity in the center, it is completely consistent with GR. In contrast to the hollow-sphere concept of RCO, the traditional, fulfilled-sphere concept requires the ignorance of GR in the RCO's central region.

We demonstrated that no predicted property of the hollow-sphere RCO contradicts the observations. On the contrary, it seems that such the concept can help us to solve several astrophysical and cosmological problems. The existence of the hollow-sphere RCO is predicted within the original GR, which is currently not the main-stream theory in the astrophysics of the compact objects, because of the postulated limitation. A discussion about the removal of the limitation is strongly desirable. Likely, we do not need any new physics. We should only use the whole extent of authentic, genuine, Einstein's theory of general relativity.

Acknowledgements. This work was supported, in part, by VEGA - the Slovak Grant Agency for Science, grant No. 2/0009/22.

References

- Anastopoulos, C. & Savidou, N., Classification theorem and properties of singular solutions to the Tolman-Oppenheimer-Volkoff equation. 2021, *Classical and Quantum Gravity*, **38**, 075024, DOI: 10.1088/1361-6382/abdf26
- Birkhoff, G. D. & Langer, R. E. 1923, *Relativity and modern physics* (Harvard University Press)
- Buchdahl, H. A., General-Relativistic Fluid Spheres. III. a Static Gaseous Model. 1967, *Astrophysical Journal*, **147**, 310, DOI: 10.1086/149001
- Chandrasekhar, S., The highly collapsed configurations of a stellar mass (Second paper). 1935, *Monthly Notices of the Royal Astronomical Society*, **95**, 207, DOI: 10.1093/mnras/95.3.207
- Chandrasekhar, S., The increasing role of general relativity in astronomy. 1972, *The Observatory*, **92**, 160
- deLyra, J. L., Energetic Stability of the Solutions of the Einstein Field Equations for Spherically Symmetric Liquid Shells. 2021, *arXiv e-prints*, arXiv:2101.07214, DOI: 10.48550/arXiv.2101.07214
- deLyra, J. L., The black-hole limits of the spherically symmetric and static relativistic polytrope solutions. 2023, *General Relativity and Gravitation*, submitted
- deLyra, J. L. & Carneiro, C. E. I., Complete solution of the Einstein field equations for a spherical distribution of polytropic matter. 2023, *General Relativity and Gravitation*, **55**, 67, DOI: 10.1007/s10714-023-03115-6
- deLyra, J. L., de A. Orselli, R., & Carneiro, C. E. I., Exact solution of the Einstein field equations for a spherical shell of fluid matter. 2023, *General Relativity and Gravitation*, **55**, 68, DOI: 10.1007/s10714-023-03116-5
- Einstein, A., Die Feldgleichungen der Gravitation. 1915, *Sitzungsberichte der Königlich Preussischen Akademie der Wissenschaften*, **XLVIII**, 844
- Einstein, A., Die Grundlage der allgemeinen Relativitätstheorie. 1916, *Annalen der Physik*, **354**, 769, DOI: 10.1002/andp.19163540702

- Hajj-Boutros, J., Radiation Equilibrium in General Relativity: General Solution. 1989, *Modern Physics Letters A*, **4**, 427, DOI: 10.1142/S0217732389000514
- Hansen, C. J. & Kawaler, S. D. 1994, *Stellar Interiors. Physical Principles, Structure, and Evolution*. (Springer)
- Hernández, H., Suárez-Urango, D., & Núñez, L. A., Acceptability conditions and relativistic barotropic equations of state. 2021, *European Physical Journal C*, **81**, 241, DOI: 10.1140/epjc/s10052-021-09044-5
- Ivanov, B. V., Analytical study of anisotropic compact star models. 2017, *European Physical Journal C*, **77**, 738, DOI: 10.1140/epjc/s10052-017-5322-7
- Kotopoulos, D. & Anastopoulos, C., Thermodynamics of spherically symmetric thin-shell spacetimes. 2023, *Classical and Quantum Gravity*, **40**, 225005, DOI: 10.1088/1361-6382/acfec1
- Misner, C. W., Thorne, K. S., & Wheeler, J. A. 2017, *Gravitation* (Princeton University Press)
- Murk, S., Nomen non est omen: why it is too soon to identify ultra-compact objects as black holes. 2022, *arXiv e-prints*, arXiv:2210.03750, DOI: 10.48550/arXiv.2210.03750
- Neslušan, L., The Ni's Solution for Neutron Star and Outward Oriented Gravitational Attraction in Its Interior. 2015, *Journal of Modern Physics*, **6**, 2164, DOI: 10.4236/jmp.2015.615220
- Neslušan, L., A solution to unconstrained Einstein's equations for a relativistic radiation sphere. in , *New Frontiers in Black Hole Astrophysics*, ed. A. Gomboc, Vol. **324** (Cambridge University Press), 355
- Neslušan, L., Outline of the concept of stable relativistic radiation sphere. A model of quasar? 2017b, *Astrophysics and Space Science*, **362**, 48, DOI: 10.1007/s10509-017-3027-x
- Neslušan, L., The second rise of general relativity in astrophysics. 2019, *Modern Physics Letters A*, **34**, 1950244, DOI: 10.1142/S0217732319502444
- Neslušan, L., A demonstration of the difference between the normalized and non-limited solutions of the field equations in the modeling of relativistic compact objects. 2022, in *Cosmology on Small Scales 2022*, ed. M. Krížek & Y. V. Dumin (Institute of Mathematics, Czech Academy of Sciences), 85
- Neslušan, L., Component x of the gravitational acceleration in general relativity and concept of mass. 2023, *Contributions of the Astronomical Observatory Skalnaté Pleso*, **53**, 16, DOI: 10.31577/caosp.2023.53.2.16
- Ni, J., Solutions without a maximum mass limit of the general relativistic field equations for neutron stars. 2011, *Science China Physics, Mechanics, and Astronomy*, **54**, 1304, DOI: 10.1007/s11433-011-4350-9
- Oppenheimer, J. R. & Snyder, H., On Continued Gravitational Contraction. 1939, *Physical Review*, **56**, 455, DOI: 10.1103/PhysRev.56.455
- Oppenheimer, J. R. & Volkoff, G. M., On Massive Neutron Cores. 1939, *Physical Review*, **55**, 374, DOI: 10.1103/PhysRev.55.374

- Penrose, R., Gravitational Collapse: the Role of General Relativity. 1969, *Nuovo Cimento Rivista Serie*, **1**, 252
- Schwarzschild, K., Über das Gravitationsfeld einer Kugel aus inkompressibler Flüssigkeit nach der Einsteinschen Theorie. 1916, in *Sitzungsberichte der Königlich Preussischen Akademie der Wissenschaften zu Berlin*, 424
- Stephani, H., Kramer, D., MacCallum, M., Hoenselaers, C., & Herlt, E. 2009, *Exact Solutions of Einstein's Field Equations* (Cambridge University Press)
- Straumann, N. 2013, *General Relativity* (Springer)
- Tolman, R. C. 1934, *Relativity, Thermodynamics, and Cosmology* (Clarendon Press)
- Tolman, R. C., Static Solutions of Einstein's Field Equations for Spheres of Fluid. 1939, *Physical Review*, **55**, 364, DOI: 10.1103/PhysRev.55.364
- Tolman, R. C. & Ehrenfest, P., Temperature Equilibrium in a Static Gravitational Field. 1930, *Physical Review*, **36**, 1791, DOI: 10.1103/PhysRev.36.1791
- Tooper, R. F., Adiabatic Fluid Spheres in General Relativity. 1965, *Astrophysical Journal*, **142**, 1541, DOI: 10.1086/148435
- Turck-Chieze, S., Cahen, S., Casse, M., & Doom, C., Revisiting the Standard Solar Model. 1988, *Astrophysical Journal*, **335**, 415, DOI: 10.1086/166936
- Whittaker, J. M., An Interior Solution in General Relativity. 1968, *Proceedings of the Royal Society of London Series A*, **306**, 1, DOI: 10.1098/rspa.1968.0133

PRÁCE ASTRONOMICKÉHO OBSERVATÓRIA
NA SKALNATOM PLESE
LIV, číslo 3

Zostavovateľ:	RNDr. Richard Komžík, CSc.
Vedecký redaktor:	RNDr. Augustín Skopal, DrSc.
Vydal:	Astronomický ústav SAV, Tatranská Lomnica
IČO vydavateľa:	00 166 529
Periodicita:	3-krát ročne
ISSN (on-line verzia):	1336-0337
CODEN:	CAOPF8
Rok vydania:	2024
Počet strán:	96

Contributions of the Astronomical Observatory Skalnaté Pleso are processed using
L^AT_EX 2_ε CAOSP DocumentClass file 3.09 ver. 2021.